

State University of New York Report

**Numerical Simulation of High-Speed
Turbulent Reacting Flows**

by

**F.A. Jaber, P.J. Colucci, S. James, and P. Givi
Department of Mechanical and Aerospace Engineering
State University of New York at Buffalo
Buffalo, NY 14260-4400**

**Annual Report Submitted to
The NASA Langley Research Center**

Progress Report on Activities Supported Under Grant NAG 1-1122

for the Period

August 1, 1996 - July 31, 1997

Contents

1	Summary of Achievements	1
2	Introduction	2
3	Governing Equations	3
3.1	Modeling	5
4	The Filtered Mass Density Function (FMDF)	7
5	Lagrangian Stochastic Solution of the FMDF	11
6	Numerical Solution Procedure	12
7	Results	17
7.1	Flows Simulated	17
7.2	Reaction Mechanisms	20
7.3	Numerical Specifications	23
7.4	Consistency of FMDF	27
7.5	Validations via DNS	31
7.6	Validations via Laboratory Data	36
8	Concluding Remarks	41
9	Personnel	42

Numerical Simulation of High-Speed Turbulent Reacting Flows

F.A. Jaber, P.J. Colucci, S. James and P. Givi
Department of Mechanical and Aerospace Engineering
State University of New York at Buffalo
Buffalo, NY 14260-4400

Abstract

The purpose of this research is to continue our efforts in advancing the state of knowledge in large eddy simulation (LES) methods for computational analysis of high-speed reacting turbulent flows. We have just completed first year of Phase III of this research. This annual report provides a brief and up-to-date summary of our activities during the period: August 1, 1996 through July 31, 1997.

Technical Monitor

Dr. J. Philip Drummond (Hypersonic Propulsion Branch, NASA LaRC, Mail Stop 197, Tel: 757-864-2298) is the Technical Monitor of this

1 Summary of Achievements

We are now in Year 1 of the Phase III activities on this NASA LaRC sponsored project. The total time allotted for this phase is three years; this phase was followed at the conclusion of Phase II activities (also for three years). In total we have completed 7 years of LaRC supported research, and two years are remaining.

Our efforts in the past year have been particularly fruitful. We developed a new methodology termed the "filtered mass density function" (FMDf) and implemented it for LES of variable

density chemically reacting turbulent flows at low Mach numbers. The FMDF represents the single point joint probability density function of the subgrid scale (SGS) scalar quantities and is obtained by solution of its modeled transport equation. In this equation, the chemical reactions appear in closed form but the influences of scalar mixing and convection within the subgrid are modeled. The stochastic differential equations (SDEs) which yield statistically equivalent results to that of the FMDF transport equation are derived and are solved via a Lagrangian Monte Carlo scheme. The consistency, convergence, and accuracy of FMDF and the Monte Carlo solution of its equivalent SDEs are assessed via comparison with data generated by direct numerical simulation (DNS) and with experimental data. In nonreacting flows, it is shown that the filtered values of temperature, density and scalars compare very well with those obtained by “conventional” LES procedure in which the finite difference solution of the transport equations governing these filtered quantities is obtained. The advantage of the FMDF is demonstrated in reacting flows. In the absence of closures for the subgrid scalar, density and temperature correlations, the results based on the conventional LES methods are significantly different from those based on DNS. The FMDF results show a much closer agreement with DNS data. The FMDF results also compare favorably with laboratory data of reacting turbulent shear flows, and correctly portrays several important features observed experimentally.

A detailed description of the FMDF is provided in this report.

2 Introduction

As indicated in our last year report, (also prepared in the form of a paper by Colucci *et al.* (1997)), we have previously developed a methodology termed the “filtered density function” (FDF) for LES of chemically reacting flows. This methodology is based on the idea originally proposed by Pope (1991). The fundamental property of the FDF is to account for the effects of subgrid scale (SGS) scalar fluctuations in a probabilistic manner. Colucci *et al.* (1997) developed a transport equation for the FDF in which the effects of unresolved convection and subgrid were modeled similarly to those in conventional LES and Reynolds averaging (RA) procedures. This transport equation was solved numerically by a Lagrangian Monte Carlo

procedure and the results were compared with those obtained by direct numerical simulations (DNS) and by the conventional LES in different free shear flows. It was shown that in non-reacting flows, the first moment of the FDF as obtained by the Monte Carlo solution is the same as that obtained by the finite difference solution of the transport equation governing the mean scalar value (LES-FD). The advantage of the FDF was demonstrated in reacting flows in which its results were shown to deviate significantly from those based on LES-FD. Detailed comparison with DNS data indicated clear advantage of FDF over LES-FD.

The encouraging results generated by FDF warrants its extensions and applications to more complex flows. Further assessment of its predictive capability are also in order. The objective in this work is to extend the methodology for treatment of reactive flows with variable density flows so that exothermic chemical reactions can be simulated. For that, we introduce the “filtered mass density function” (FMDF) which essentially is the density weighted PDF of SGS scalar variables. With the definition of the FMDF, the mathematical framework for its implementation in LES of reacting flows is established. The results obtained by FMDF are scrutinized by detailed comparisons with DNS and laboratory data. The FMDF deals only with scalar quantities; the hydrodynamic field is obtained via the conventional LES procedure. Probability treatment of the SGS velocity fluctuations is postponed for future work. Also, the formulation is based on the assumption of low Mach number. Thus while exothermicity and variable density effects can be studied, high speed flows cannot be treated by the formulation presented here.

3 Governing Equations

The primary transport variables in a compressible flow undergoing chemical reaction are the density ρ , the velocity vector u_i along the x_i direction, the total specific enthalpy h , the pressure p , and the species mass fractions Y_α ($\alpha = 1, 2, \dots, N_s$). The conservation equations governing these variables are the continuity, momentum, enthalpy (energy) and species mass fraction equations, along with an equation of state relating thermodynamic variables. These equations are expressed as (Williams, 1985):

$$\frac{\partial \rho}{\partial t} + \frac{\partial \rho u_i}{\partial x_i} = 0 \quad (1)$$

$$\frac{\partial \rho u_j}{\partial t} + \frac{\partial \rho u_i u_j}{\partial x_i} = -\frac{\partial p}{\partial x_j} + \frac{\partial \tau_{ij}}{\partial x_i} \quad (2)$$

$$\frac{\partial \rho \phi_\alpha}{\partial t} + \frac{\partial \rho u_i \phi_\alpha}{\partial x_i} = -\frac{\partial J_i^\alpha}{\partial x_i} + \rho S_\alpha, \quad \alpha = 1, 2, \dots, \sigma = N_s + 1 \quad (3)$$

$$p = \rho R^0 T \sum_{\alpha=1}^{N_s} Y_\alpha / \mathcal{M}_\alpha = \rho \mathcal{R} T \quad (4)$$

where t represents time, R^0 is the universal gas constant and \mathcal{M}_α is the molecular weight of species α . Equation (4) effectively defines the mixture gas “constant” \mathcal{R} . Equation (3) represents the mass fraction and enthalpy equations in a common form with

$$\phi_\alpha \equiv Y_\alpha, \quad \alpha = 1, 2, \dots, N_s,$$

$$\phi_\sigma \equiv h = \sum_{\alpha=1}^{N_s} h_\alpha \phi_\alpha \quad (5)$$

in which:

$$h_\alpha = h_\alpha^0 + \int_{T_0}^T c_{p_\alpha}(T') dT' \quad (6)$$

where T denotes the temperature, T_0 is the reference temperature and h_α^0 and c_{p_α} denote the enthalpy of formation and constant pressure specific heat of species α respectively.

At low Mach numbers, by neglecting the viscous dissipation and thermal radiation, the source terms in the enthalpy equation becomes $S_\sigma \equiv S_h = \frac{1}{\rho} \frac{Dp}{Dt} \approx \frac{1}{\rho} \frac{\partial p}{\partial t}$. The chemical source terms ($S_\alpha = S_\alpha(\phi)$, $\phi = [Y_1, Y_2, \dots, Y_{N_s}, h]$) are functions of the composition variables (ϕ).

For a Newtonian fluid with zero bulk viscosity and Fickian diffusion, the viscous stress tensor τ_{ij} , mass and heat flux (J_i^α , $\alpha = 1, 2, \dots, \sigma$) are given by:

$$\tau_{ij} = \mu \left(\frac{\partial u_i}{\partial x_j} + \frac{\partial u_j}{\partial x_i} - \frac{2}{3} \frac{\partial u_k}{\partial x_k} \delta_{ij} \right) \quad (7)$$

$$J_i^\alpha = -\gamma \frac{\partial \phi_\alpha}{\partial x_i} \quad (8)$$

where μ is the dynamic viscosity and $\gamma = \rho\Gamma$ denotes the thermal and mass molecular diffusivity coefficients. In the present work, the Lewis number is assumed to be unity.

Large eddy simulation involves the use of the spatial filtering operation (Aldama, 1990):

$$\langle f(\mathbf{x}, t) \rangle_\ell = \int_{-\infty}^{+\infty} f(\mathbf{x}', t) \mathcal{G}(\mathbf{x}', \mathbf{x}) d\mathbf{x}' \quad (9)$$

where \mathcal{G} denotes the filter function, $\langle f(\mathbf{x}, t) \rangle_\ell$ represents the filtered value of the transport variable $f(\mathbf{x}, t)$, and $f' = f - \langle f \rangle_\ell$ denotes the fluctuations of f from the filtered value. For variable density flows it is more convenient to consider the Favre filtered quantity defined as:

$$\langle f(\mathbf{x}, t) \rangle_L = \frac{\langle \rho f \rangle_\ell}{\langle \rho \rangle_\ell}$$

and the fluctuation about this filtered value $f'' = f - \langle f \rangle_L$.

For a spatially and temporally invariant filter function, $\mathcal{G}(\mathbf{x}', \mathbf{x}) \equiv G(\mathbf{x}' - \mathbf{x})$, the application of the filtering operation to the transport equations yields:

$$\frac{\partial \langle \rho \rangle_\ell}{\partial t} + \frac{\partial \langle \rho \rangle_\ell \langle u_i \rangle_L}{\partial x_i} = 0 \quad (10)$$

$$\frac{\partial \langle \rho \rangle_\ell \langle u_j \rangle_L}{\partial t} + \frac{\partial \langle \rho \rangle_\ell \langle u_i \rangle_L \langle u_j \rangle_L}{\partial x_i} = -\frac{\partial \langle p \rangle_\ell}{\partial x_j} + \frac{\partial \langle \tau_{ij} \rangle_\ell}{\partial x_i} - \frac{\partial T_{ij}}{\partial x_i} \quad (11)$$

$$\frac{\partial \langle \rho \rangle_\ell \langle \phi_\alpha \rangle_L}{\partial t} + \frac{\partial \langle \rho \rangle_\ell \langle u_i \rangle_L \langle \phi_\alpha \rangle_L}{\partial x_i} = -\frac{\partial \langle J_i^\alpha \rangle_\ell}{\partial x_i} - \frac{\partial M_i^\alpha}{\partial x_i} + \langle \rho S_\alpha \rangle_\ell, \quad \alpha = 1, 2, \dots, \sigma \quad (12)$$

where $T_{ij} = \langle \rho \rangle_\ell (\langle u_i u_j \rangle_L - \langle u_i \rangle_L \langle u_j \rangle_L)$ and $M_i^\alpha = \langle \rho \rangle_\ell (\langle u_i \phi_\alpha \rangle_L - \langle u_i \rangle_L \langle \phi_\alpha \rangle_L)$ denote the subgrid stress and the subgrid mass flux, respectively, $\langle \rho S_\alpha \rangle_\ell = \langle \rho \rangle_\ell \langle S_\alpha \rangle_L$ ($\alpha = 1, 2, \dots, N_s$) are the filtered reaction rates and $\langle \rho S_h \rangle_\ell = \frac{\partial \langle p \rangle_\ell}{\partial t}$. In this work the contribution $\langle S_h \rangle_L$ is assumed to be negligible.

3.1 Modeling

In LES of non-reacting flows the closure problem is associated with T_{ij} and M_i^α (Erlebacher *et al.*, 1992; Salvetti and Banerjee, 1995). In reacting flows, an additional model is required for the filtered reaction rate $\langle S_\alpha \rangle_L$. Here, modeling of $\langle S_\alpha \rangle_L$ is the subject of the probability

formulation as described in the next section. For the former two, we make use of currently available and well-established closures. The subgrid stress is modeled via two different eddy viscosity closures. The first is the compressible form of the Smagorinsky model (Erlebacher *et al.*, 1992):

$$T_{ij} = -2C_{R1}\langle\rho\rangle_t\Delta_G^2\Pi_S^{1/2}\left(\langle\mathcal{S}_{ij}\rangle_L - \frac{1}{3}\langle\mathcal{S}_{kk}\rangle_L\delta_{ij}\right) + \frac{2}{3}C_{I1}\langle\rho\rangle_t\Delta_G^2\Pi_S\delta_{ij} \quad (13)$$

where $\langle\mathcal{S}_{ij}\rangle_L$ is the resolved scale strain rate tensor, $\Pi_S = \langle\mathcal{S}_{ij}\rangle_L\langle\mathcal{S}_{ij}\rangle_L$, Δ_G is the characteristic size of filter and C_{R1} , C_{I1} are empirical constants. The drawbacks of this closure are well-recognized (Zang and Piomelli, 1993; Kerr *et al.*, 1996). In an attempt to overcome some of these drawbacks, we also make use of a second closure which is the variable density form of the model that has been used in our previous work (Colucci *et al.*, 1997) and is given as:

$$T_{ij} = -2C_{R2}\langle\rho\rangle_t\Delta_GE^{1/2}\left(\langle\mathcal{S}_{ij}\rangle_L - \frac{1}{3}\langle\mathcal{S}_{kk}\rangle_L\delta_{ij}\right) + \frac{2}{3}C_{I2}\langle\rho\rangle_tE\delta_{ij} \quad (14)$$

where $E = |\langle u_i^*\rangle_L\langle u_i^*\rangle_L - \langle\langle u_i^*\rangle_{L'}\langle\langle u_i^*\rangle_{L'}\rangle|$, $u_i^* = u_i - \mathcal{U}_i$ and \mathcal{U}_i is a reference velocity in the x_i direction. The subscript ℓ' denotes the filter at the secondary level which has a characteristic size (denoted by $\Delta_{G'}$) larger than that of grid level filter. This model is essentially a modified version of that proposed by Bardina *et al.* (1983), which utilize equal sizes for the grid and secondary filters. We refer to this as the modified kinetic energy viscosity (MKEV) closure. Accordingly, the subgrid eddy viscosity, ν_t for these two closures are expressed as:

$$\nu_t = C_{R1}\Delta_G^2\sqrt{\langle\mathcal{S}_{ij}\rangle_L\langle\mathcal{S}_{ij}\rangle_L}, \quad (15)$$

and

$$\nu_t = C_{R2}\Delta_G\sqrt{|\langle u_i^*\rangle_L\langle u_i^*\rangle_L - \langle\langle u_i^*\rangle_{L'}\langle\langle u_i^*\rangle_{L'}\rangle|}, \quad (16)$$

respectively.

A similar diffusivity model is used for the closure of the subgrid mass flux (Eidson, 1985):

$$M_i^\alpha = -\gamma_t\frac{\partial\langle\phi_\alpha\rangle_L}{\partial x_i} \quad (17)$$

where $\gamma_t = \langle\rho\rangle_t\Gamma_t$, $\Gamma_t = \nu_t/Sc_t$, and Sc_t is the subgrid Schmidt number, assumed to be constant and equal to subgrid Prandtl number.

4 The Filtered Mass Density Function (FMDF)

Let $\phi(\mathbf{x}, t)$ denote the scalar array. We define the “filtered mass density function” (FMDF), denoted by F_L , as:

$$F_L(\psi; \mathbf{x}, t) \equiv \int_{-\infty}^{+\infty} \rho(\mathbf{x}', t) \zeta[\psi, \phi(\mathbf{x}', t)] G(\mathbf{x}' - \mathbf{x}) d\mathbf{x}' \quad (18)$$

$$\zeta[\psi, \phi(\mathbf{x}, t)] = \delta[\psi - \phi(\mathbf{x}, t)] \equiv \prod_{\alpha=1}^{\sigma} \delta[\psi_{\alpha} - \phi_{\alpha}(\mathbf{x}, t)] \quad (19)$$

where δ denotes the delta function and ψ denotes the composition domain of the scalar array. The semicolon indicates that $F_L(\psi; \mathbf{x}, t)$ is the FMDF with regards to the compositional variables ψ only. The term $\zeta[\phi, \psi(\mathbf{x}, t)]$ is the “fine-grained” density (O’Brien, 1980; Pope, 1985), and Eq. (18) implies that the FMDF is the *mass weighted spatially filtered* value of the fine-grained density. The integral property of the FMDF is such that

$$\int_{-\infty}^{+\infty} F_L(\psi; \mathbf{x}, t) d\psi = \int_{-\infty}^{+\infty} \rho(\mathbf{x}', t) G(\mathbf{x}' - \mathbf{x}) d\mathbf{x}' = \langle \rho(\mathbf{x}, t) \rangle_{\ell}. \quad (20)$$

The FMDF is related to the FDF ($f_L(\psi; \mathbf{x}, t)$) ((Colucci *et al.*, 1997)) through the density: $\hat{\rho}(\psi) f_L(\psi; \mathbf{x}, t) = F_L(\psi; \mathbf{x}, t)$. Additionally, it is useful to define the Favre-weighted FDF $\mathcal{F}_L(\psi; \mathbf{x}, t)$ through $\langle \rho \rangle_{\ell} \mathcal{F}_L(\psi; \mathbf{x}, t) = \hat{\rho}(\psi) f_L(\psi; \mathbf{x}, t) = F_L(\psi; \mathbf{x}, t)$.

For further developments, it is useful to define the mass weighted conditional filtered mean of the variable $Q(\mathbf{x}, t)$ as:

$$\langle Q(\mathbf{x}, t) | \psi \rangle_{\ell} \equiv \frac{\int_{-\infty}^{+\infty} \rho(\mathbf{x}', t) Q(\mathbf{x}', t) \zeta[\psi, \phi(\mathbf{x}', t)] G(\mathbf{x}' - \mathbf{x}) d\mathbf{x}'}{F_L(\psi; \mathbf{x}, t)} \quad (21)$$

Equation (21) implies the following properties:

$$(i) \quad \text{For } Q(\mathbf{x}, t) = c, \quad \langle Q(\mathbf{x}, t) | \psi \rangle_{\ell} = c \quad (22)$$

$$(ii) \quad \text{For } Q(\mathbf{x}, t) \equiv \hat{Q}(\phi(\mathbf{x}, t)), \quad \langle Q(\mathbf{x}, t) | \psi \rangle_{\ell} = \hat{Q}(\psi) \quad (23)$$

$$(iii) \quad \text{Integral property :} \quad \int_{-\infty}^{+\infty} \langle Q(\mathbf{x}, t) | \psi \rangle_{\ell} F_L(\psi; \mathbf{x}, t) d\psi = \langle \rho(\mathbf{x}, t) \rangle_{\ell} \langle Q(\mathbf{x}, t) \rangle_L \quad (24)$$

where c is a constant, and $\widehat{Q}(\phi(\mathbf{x}, t)) \equiv Q(\mathbf{x}, t)$ denotes the case where the variable Q can be completely described by the compositional variable $\phi(\mathbf{x}, t) \equiv [\phi_1, \phi_2, \dots, \phi_\sigma]$. From these properties, it follows that the filtered value of any function of the scalar variables (such as $\rho \equiv \widehat{\rho}[\phi(\mathbf{x}, t)]$ and $S_\alpha \equiv \widehat{S}_\alpha[\phi(\mathbf{x}, t)]$) is obtained by integration over the composition space.

To develop a transport equation for the FMDF, first the transport equation for fine-grained density is derived. By applying the method developed by Lundgren (1969) and others (Pope, 1976; O'Brien, 1980) to Eq. (3) it can be shown that the fine-grained density evolves according to the following equation:

$$\frac{\partial \widehat{\rho}(\psi) \zeta(\phi, \psi)}{\partial t} + \frac{\partial \widehat{\rho}(\phi) u_i(\mathbf{x}, t) \zeta(\phi, \psi)}{\partial x_i} = \frac{\partial \zeta(\phi, \psi)}{\partial \psi_\alpha} \frac{\partial J_i^\alpha}{\partial x_i} - \widehat{\rho}(\phi) \frac{\partial}{\partial \psi_\alpha} [\widehat{S}_\alpha(\psi) \zeta(\phi, \psi)]. \quad (25)$$

The transport equation for $F_L(\psi; \mathbf{x}, t)$ is obtained by multiplying Eq. (25) with the filter function $G(\mathbf{x}' - \mathbf{x})$ and integrating over \mathbf{x}' space. The final result after some algebraic manipulation is

$$\begin{aligned} \frac{\partial F_L(\psi; \mathbf{x}, t)}{\partial t} + \frac{\partial [\langle u_i(\mathbf{x}, t) | \psi \rangle_\ell F_L(\psi; \mathbf{x}, t)]}{\partial x_i} &= \frac{\partial}{\partial \psi_\alpha} \left[\left\langle \frac{1}{\widehat{\rho}(\phi)} \frac{\partial J_i^\alpha}{\partial x_i} | \psi \right\rangle_\ell F_L(\psi; \mathbf{x}, t) \right] \\ &\quad - \frac{\partial [\widehat{S}_\alpha(\psi) F_L(\psi; \mathbf{x}, t)]}{\partial \psi_\alpha}. \end{aligned} \quad (26)$$

The unclosed nature of convection and mixing is indicated by the conditional filtered value of the velocity and gradient of scalar flux. These unclosed terms can be further simplified. The convection term is decomposed into resolved and subgrid scale components as:

$$\langle u_i | \psi \rangle_\ell F_L = \langle u_i \rangle_L F_L + [\langle u_i | \psi \rangle_\ell - \langle u_i \rangle_L] F_L. \quad (27)$$

With the assumption of constant property Fickian diffusion, the conditional scalar flux gradient term may be decomposed into diffusive and dissipative parts:

$$\frac{\partial}{\partial \psi_\alpha} \left[\left\langle -\frac{1}{\widehat{\rho}} \frac{\partial}{\partial x_i} \left(\gamma \frac{\partial \phi_\alpha}{\partial x_i} \right) | \psi \right\rangle_\ell F_L \right] = \frac{\partial}{\partial x_i} \left(\gamma \frac{\partial (F_L / \widehat{\rho})}{\partial x_i} \right) - \frac{\partial^2}{\partial \psi_\alpha \partial \psi_\beta} \left[\left\langle \gamma \frac{\partial \phi_\alpha}{\partial x_i} \frac{\partial \phi_\beta}{\partial x_i} | \psi \right\rangle_\ell F_L / \widehat{\rho} \right]. \quad (28)$$

The first term on the right hand side of this equation represents the effect of molecular diffusion on the spatial transport of the FMDF. The second term represents the dissipative

nature of subgrid mixing. Upon substitution of Eqs. (27) and (28) in Eq. (26):

$$\begin{aligned} \frac{\partial F_L}{\partial t} + \frac{\partial \langle u_i \rangle_L F_L}{\partial x_i} &= \frac{\partial}{\partial x_i} \left(\gamma \frac{\partial (F_L / \hat{\rho})}{\partial x_i} \right) - \frac{\partial^2}{\partial \psi_\alpha \partial \psi_\beta} \left[\left\langle \gamma \frac{\partial \phi_\alpha}{\partial x_i} \frac{\partial \phi_\beta}{\partial x_i} | \psi \right\rangle_t F_L / \hat{\rho} \right] \\ &- \frac{\partial [\langle u_i | \psi \rangle_t - \langle u_i \rangle_L] F_L}{\partial x_i} - \frac{\partial [\hat{S}_\alpha(\psi) f_L]}{\partial \psi_\alpha}. \end{aligned} \quad (29)$$

This is an exact transport equation for the FMDF. The last term on the right hand side of this equation is due to chemical reaction (and also reference pressure for $\alpha = \sigma$) and is in a closed form. The first term on the right hand side represents the effects of molecular diffusion of FDF in physical space and is closed. The second term on the left hand side represents convection of the FDF in physical space and is also closed provided $\langle u_i \rangle_L$ is known. The unclosed terms are associated with the second and third terms on the right hand side representing the influences of molecular mixing and the unresolved subgrid scale convection, respectively.

The unclosed terms in Eq. (29) are modeled in a fashion consistent with conventional LES. The subgrid convective flux is modeled via:

$$[\langle u_i | \psi \rangle_t - \langle u_i \rangle_L] F_L = -\gamma_t \frac{\partial (F_L / \langle \rho \rangle_t)}{\partial x_i} \quad (30)$$

The advantage of the decomposition (Eq. (27)) and the subsequent model (Eq. (30)) is that they yield results similar to that in conventional LES. The first two Favre moments corresponding to Eqs. (27) and (30) are:

$$\langle u_i \phi_\alpha \rangle_L = \langle u_i \rangle_L \langle \phi_\alpha \rangle_L + [\langle u_i \phi_\alpha \rangle_L - \langle u_i \rangle_L \langle \phi_\alpha \rangle_L], \quad (31)$$

$$\langle \rho \rangle_t [\langle u_i \phi_\alpha \rangle_L - \langle u_i \rangle_L \langle \phi_\alpha \rangle_L] = -\gamma_t \frac{\partial \langle \phi_\alpha \rangle_L}{\partial x_i} \quad (32)$$

The term within brackets in Eq. (31) is the generalized scalar flux in the form considered in conventional LES (Germano, 1992; Salvetti and Banerjee, 1995). Consequently, Eq. (32) becomes identical to Eq. (17).

The closure for the conditional subgrid diffusion is based on the linear mean square estimation (LMSE) model (O'Brien, 1980; Dopazo and O'Brien, 1976), which is also known as the IEM

(interaction by exchange with the mean) closure (Borghi, 1988):

$$\frac{\partial^2}{\partial \psi_\alpha \partial \psi_\beta} \left[\left\langle \gamma \frac{\partial \phi_\alpha}{\partial x_i} \frac{\partial \phi_\beta}{\partial x_i} | \psi \right\rangle_\ell F_L / \bar{\rho} \right] = - \frac{\partial}{\partial \psi_\alpha} [\Omega_m (\psi_\alpha - \langle \phi_\alpha \rangle_L) F_L], \quad (33)$$

where Ω_m is the “frequency of mixing within the subgrid” which is not known *a priori*. This frequency can be related to the subgrid diffusion coefficient and the filter length: $\Omega_m = C_\Omega (\gamma + \gamma_\ell) / (\langle \rho \rangle_\ell \Delta_G^2)$. The second moment of Eq. (33) provides an expression for the subgrid scalar dissipation of species α :

$$\epsilon_{s\alpha} = 2 \left\langle \gamma \frac{\partial \phi_{(\alpha)}}{\partial x_i} \frac{\partial \phi_{(\alpha)}}{\partial x_i} \right\rangle_\ell = 2 \Omega_m \langle \rho \rangle_\ell (\langle \phi_\alpha^2 \rangle_L - \langle \phi_\alpha \rangle_L^2) \quad (34)$$

where the subscripts in parenthesis are excluded from the summation convention.

To establish consistency between the FMDF and conventional moment closure approaches we make use of the assumption:

$$\frac{\partial}{\partial x_i} \left(\gamma \frac{\partial (F_L / \bar{\rho})}{\partial x_i} \right) \approx \frac{\partial}{\partial x_i} \left(\gamma \frac{\partial (F_L / \langle \rho \rangle_\ell)}{\partial x_i} \right). \quad (35)$$

Note that this assumption is not necessary to evaluate the FMDF and is only adopted to establish consistency.

In the general case that the molecular diffusivity is a function of the scalar variables, the decomposition of the conditional scalar flux gradient takes on the form:

$$\frac{\partial}{\partial \psi_\alpha} \left[\left\langle -\frac{1}{\bar{\rho}} \frac{\partial}{\partial x_i} \left(\gamma \frac{\partial \phi_\alpha}{\partial x_i} \right) | \psi \right\rangle_\ell F_L \right] = \frac{\partial}{\partial x_i} \left\langle \gamma \frac{\partial \zeta}{\partial x_i} \right\rangle_\ell - \frac{\partial^2}{\partial \psi_\alpha \partial \psi_\beta} \left[\left\langle \gamma \frac{\partial \phi_\alpha}{\partial x_i} \frac{\partial \phi_\beta}{\partial x_i} | \psi \right\rangle_\ell F_L / \bar{\rho} \right]. \quad (36)$$

Note that the diffusive term is in a form that accounts for the correlations between the scalars and the molecular diffusivity. This term may be approximated by:

$$\frac{\partial}{\partial x_i} \left\langle \rho \Gamma \frac{\partial \zeta}{\partial x_i} \right\rangle_\ell \approx \frac{\partial}{\partial x_i} \left[\langle \rho \rangle_\ell \langle \Gamma \rangle_L \frac{\partial (F_L / \langle \rho \rangle_\ell)}{\partial x_i} \right] = \frac{\partial}{\partial x_i} \left[\langle \rho \rangle_\ell \langle \Gamma \rangle_L \frac{\partial \mathcal{F}_L}{\partial x_i} \right] \quad (37)$$

where $\langle \Gamma \rangle_L = \Gamma(\langle \phi \rangle_L)$. This neglects these correlations and allows one to work directly with

Favre filtered quantities. This is made clear through examination of the first moment:

$$\left\langle \rho \Gamma \frac{\partial \phi_\alpha}{\partial x_i} \right\rangle_\ell \approx \frac{\partial}{\partial x_i} \left[\langle \rho \rangle_\ell \langle \Gamma \rangle_L \frac{\partial \langle \phi_\alpha \rangle_L}{\partial x_i} \right].$$

For the remainder of this work, the molecular diffusivity is assumed constant.

With the closures given by Eqs. (30) and (33) and also the approximation made in Eq. (35), the modeled FMDF transport equation takes on the form:

$$\frac{\partial F_L}{\partial t} + \frac{\partial [\langle u_i \rangle_L F_L]}{\partial x_i} = \frac{\partial}{\partial x_i} \left[(\gamma + \gamma_t) \frac{\partial (F_L / \langle \rho \rangle_\ell)}{\partial x_i} \right] + \frac{\partial}{\partial \psi_\alpha} [\Omega_m (\psi_\alpha - \langle \phi_\alpha \rangle_L) F_L] - \frac{\partial [\hat{S}_\alpha F_L]}{\partial \psi_\alpha}. \quad (38)$$

This equation may be integrated to obtain transport equations for the SGS moments. The equation for the first subgrid Favre moment, $\langle \phi_\alpha \rangle_L$, and the generalized subgrid variance, $\sigma_\alpha^2 = \langle \phi_\alpha^2 \rangle_L - \langle \phi_\alpha \rangle_L^2$ are:

$$\frac{\partial (\langle \rho \rangle_\ell \langle \phi_\alpha \rangle_L)}{\partial t} + \frac{\partial (\langle \rho \rangle_\ell \langle u_i \rangle_L \langle \phi_\alpha \rangle_L)}{\partial x_i} = \frac{\partial}{\partial x_i} (\gamma + \gamma_t) \frac{\partial \langle \phi_\alpha \rangle_L}{\partial x_i} + \langle \rho \rangle_\ell \langle S_\alpha \rangle_L \quad (39)$$

$$\begin{aligned} \frac{\partial (\langle \rho \rangle_\ell \sigma_\alpha^2)}{\partial t} + \frac{\partial (\langle \rho \rangle_\ell \langle u_i \rangle_L \sigma_\alpha^2)}{\partial x_i} &= \frac{\partial}{\partial x_i} \left[(\gamma + \gamma_t) \frac{\partial \sigma_\alpha^2}{\partial x_i} \right] + 2(\gamma + \gamma_t) \left[\frac{\partial \langle \phi_\alpha \rangle_L}{\partial x_i} \frac{\partial \langle \phi_\alpha \rangle_L}{\partial x_i} \right] \\ &\quad - 2\Omega_m \langle \rho \rangle_\ell \sigma_\alpha^2 + 2\langle \rho \rangle_\ell (\langle \phi_\alpha S_\alpha \rangle_L - \langle \phi_\alpha \rangle_L \langle S_\alpha \rangle_L). \end{aligned} \quad (40)$$

These equations are identical to those which can be derived by filtering Eq. (3) directly, and adopting Eqs. (32) and (34) for the subgrid flux and dissipation. In such direct moment closure formulation, however, the terms involving $\langle S_\alpha \rangle_L$ remain unclosed.

5 Lagrangian Stochastic Solution of the FMDF

The Lagrangian Monte Carlo procedure (Pope, 1985) is employed for the solution of the FMDF transport equation (Eq. (38)). In this procedure, each of the Monte Carlo elements (particles) obeys certain equations which govern its transport. These particles undergo motion in physical space by convection due to the filtered mean flow velocity and diffusion due to molecular and subgrid diffusivities. For each particle, the compositional values of the

scalars are changed due to mixing and reaction.

The spatial transport of the FMDF is represented by the general diffusion process in a stochastic manner using the following stochastic differential equation (SDE): (Pope, 1985; Risken, 1989; Gardiner, 1990)

$$dX_i(t) = D_i(\mathbf{X}(t), t)dt + E(\mathbf{X}(t), t)dW_i(t) \quad (41)$$

where X_i is the Lagrangian position of a stochastic particle, D_i and E are known as the “drift” and “diffusion” coefficients, respectively, and W_i denotes the Wiener-Levy process (Karlin and Taylor, 1981). The drift and diffusion coefficients are obtained by comparing the Fokker-Plank equation corresponding to Eq. (41) with the spatial derivative terms in the FMDF transport equation (Eq. (38)),

$$E \equiv \sqrt{2(\gamma + \gamma_t)/\langle \rho \rangle_t}, \quad D_i \equiv \langle u_i \rangle_L + \frac{1}{\langle \rho \rangle_t} \frac{\partial(\gamma + \gamma_t)}{\partial x_i}. \quad (42)$$

The subgrid mixing and reaction terms are implemented by altering the compositional makeup of the particles according to the following equation,

$$\frac{\partial \phi_\alpha^+}{\partial t} = -\Omega_m(\phi_\alpha^+ - \langle \phi_\alpha \rangle_L) + \hat{S}_\alpha(\phi^+) \quad (43)$$

where $\phi_\alpha^+ = \phi_\alpha(X_i(t), t)$ denotes the scalar value of the particle with the Lagrangian position vector X_i . The solutions of Eqs. (41) and (43) yield the same statistics as those obtained directly from the solution of FMDF transport equation according to the principle of *equivalent systems* (Pope, 1985; Pope, 1994).

6 Numerical Solution Procedure

The numerical solution of the large eddy equations is based on a hybrid procedure in which the hydrodynamic Favre-filtered equations (Eqs. (10) and (11)) are integrated by a finite difference (F.D.) method and the filtered scalar field is obtained by the Monte Carlo (M.C.) solution of the FMDF transport equation. The F.D. and M.C. solvers are coupled through

the resolved thermodynamic variables. In the presentation below, the results obtained via this procedure are identified by the abbreviation FMDF-1.

For comparison, the “conventional” LES procedure is also considered. In this procedure, the modeled transport equations for the filtered scalar and the generalized subgrid scalar variance are simulated with the F.D. scheme. The hydrodynamic solver and the models for the subgrid stress and mass flux are identical to those in FMDF-1, but the effects of SGS fluctuations in the filtered reaction rate are ignored. That is, Eqs. (39)-(40) are solved via F.D. with the assumption $\langle S_\alpha(\phi) \rangle_L = S_\alpha(\langle \phi \rangle_L)$. The results based on this procedure are referred to as LES-FD.

The LES of the hydrodynamic variables, which also determines the subgrid viscosity and scalar diffusion coefficients, is conducted with the “compact parameter” F.D. scheme of Carpenter (1990). This is a variant of the MacCormack (1969) scheme in which fourth order compact differences are used to approximate the spatial derivatives, and a second order symmetric predictor-corrector sequence is employed for time discretization. The computational scheme is based on a hyperbolic solver which considers a fully compressible flow. Here, the simulations are conducted at a low Mach number ($M \approx 0.3$) to minimize compressibility effects. All the F.D. operations are conducted on fixed and equally sized grid points. Thus, the filtered values of the hydrodynamic variables are determined on these grid points. The transfer of information from these points to the location of the Monte Carlo particles is conducted via interpolation. Both fourth-order and second-order (bilinear) interpolations schemes were considered, but no significant differences in SGS statistics were observed. The results presented in the next section are based on simulations with fourth- and second-order interpolations in two-dimensional (2D) and 3D, respectively.

The FMDF is represented by an ensemble of Monte Carlo particles, each with a set of scalars $\phi_\alpha^{(n)}(\mathbf{X}^{(n)}(t), t)$ and Lagrangian position vector $\mathbf{X}^{(n)}$. A splitting operation is employed in which the transport in the physical and the compositional domains are treated separately. The simplest means of simulating Eq. (41) is via the Euler-Maruyamma approximation (Kloeden and Platen, 1995):

$$X_i^n(t_{k+1}) = X_i^n(t_k) + D_i^n(t_k)\Delta t + E^n(t_k)(\Delta t)^{1/2}\xi_i^n(t_k) \quad (44)$$

where $D_i^n(t_k) = D_i(\mathbf{X}^n(t_k))$ and $E^n(t_k) = E(\mathbf{X}^n(t_k))$. This formulation preserves the Markovian character of the diffusion process (Billingsly, 1979; Helfand, 1979; Gillespie, 1992) and facilitates affordable computations. Higher order numerical schemes for solving Eq. (41) are available (Kloeden and Platen, 1995), but one must be very cautious in using them for LES. Since the diffusion term in Eq. (41) depends on the stochastic process $\mathbf{X}(t)$, the numerical scheme must preserve the Itô-Gikhman (Itô, 1951; Gikhman and Skorokhod, 1972) nature of the process. Equation (44) exhibits this property. The coefficients D_i and E require the input of the filtered mean velocity and the diffusivity (molecular and subgrid eddy). These are provided by F.D. solution of Eqs. (10)-(11).

The compositional values are subject to change due to subgrid mixing and chemical reaction. Equation (43) may be integrated numerically to simulate these effects simultaneously. Alternatively, this equation is treated in a split manner. This provides an analytical expression for the subgrid mixing. Within a time step, Δt , the compositional change for the n^{th} particle due to mixing is:

$$(\phi_\alpha^n)^{\text{mix}} = \langle \phi_\alpha^n \rangle_L + (\phi_\alpha^n - \langle \phi_\alpha^n \rangle_L) \exp[-\Omega_m \Delta t]. \quad (45)$$

Subsequently, the influence of chemical reaction is determined by evaluating the fine grain reaction rates S_α^n and modifying the composition of the elements:

$$\phi_\alpha^n(t + \Delta t) = (\phi_\alpha^n)^{\text{mix}} + S_\alpha^n \Delta t. \quad (46)$$

The implementation of Eq. (45) requires the Favre-filtered mean scalar values. These and other higher moments of the FMDF at a given point are estimated by consideration of particles within a volume centered at the point of interest. Effectively, this finite volume constitutes an “ensemble domain” characterized by the length scale Δ_E (not to be confused with Δ_G) in which the FMDF is discretely represented. This is necessary as, with probability one, no particles will coincide with the point (Pope, 1994). Here, a box of size Δ_E is used to construct the statistics at the finite difference nodes. These are then interpolated to the particle positions. Since the mixing model only requires the input of the filtered scalar value, and not its derivative, this volume averaging procedure is sufficient. From a numerical standpoint, determination of the size of the ensemble domain is an important issue (Colucci *et al.*, 1997). Ideally, it is desired to obtain the statistics from the Monte Carlo solution

when the size of sample domain is infinitely small (*i.e.* $\Delta_E \rightarrow 0$) and the number of particles within this domain is infinitely large. With a finite number of particles, if Δ_E is small there may not be enough particles to properly construct the statistics. A larger ensemble domain decreases the statistical error, but increases the dispersion errors which manifests itself in “artificially diffused” statistical results. This compromise between the statistical accuracy and dispersive accuracy as pertaining to Lagrangian Monte Carlo schemes implies that the optimum magnitude of Δ_E cannot, in general, be specified *a priori* (Pope, 1985; Colucci *et al.*, 1997). This does not diminish the capability of the procedure, but exemplifies the importance of the parameters which govern the statistics.

In an attempt to reduce computational overhead, a procedure involving the use of non-uniform weights is implemented. This approach allows a small number of particles to be imposed in regions where the behavior exhibits a low degree of variability. Conversely, in regions where the phenomena exhibits highly variable character, a large number of particles is desired to accurately represent the FMDF. This procedure is akin to grid compression in finite difference or finite volume approaches: whereas grid compression is a utility in increasing the *spatial* resolution in areas of interest, the application of variable weights allows for an increase in the resolution of the FMDF in selected regions. This is exemplified in the case of a reactive mixing layer. In the freestream regions where the composition is essentially described by a delta function, a low number of particles (in fact a single particle) is adequate to quantify the FMDF. In contrast, in the vicinity of the reaction zone it is desirable to impose a high number of particles as the composition takes on a wide range of values and the subgrid PDF in this region is more broad banded. In a slight generalization of that developed by Pope (1985), the particles evolve with a discrete Lagrangian FMDF $F_N^*(\psi, \mathbf{x}; t)$:

$$F_N^*(\psi, \mathbf{x}; t) = \Delta m \sum_{n \in \Delta_E} w^n \delta(\psi - \phi^n) \delta(\mathbf{x} - \mathbf{x}^n) \quad (47)$$

where Δm is the mass of a particle with unit weight and w^n is the weight of the n^{th} particle. Note that the semicolon is placed *after* the position vector \mathbf{x} since position constitutes a random variable for this *Lagrangian* FMDF. With integration of this expression over the

composition domain it is possible to demonstrate:

$$\langle \rho \rangle_{\ell} \propto \sum_{n \in \Delta_E} w^n \quad (48)$$

and the Favre filtered value of a transport quantity $\hat{Q}(\phi)$ is constructed by the weighted average

$$\langle Q \rangle_L = \frac{\sum_{n \in \Delta_E} w^n \hat{Q}(\phi^n)}{\sum_{n \in \Delta_E} w^n}. \quad (49)$$

Equation (48) implies that the filtered fluid density must be directly proportional to the sum of the weights in the ensemble domain. In the event of uniform weights, these expressions reduce to familiar forms $\langle \rho \rangle_L \propto N_E$ and $\langle Q \rangle_L = \frac{1}{N_E} \sum \hat{Q}(\phi^k)$ (Pope, 1985) where N_E is the number of particles in the ensemble domain. Hence, with uniform weights, the particle number density decreases significantly in regions of high temperature. This is particularly important because high temperature regions are typically associated with the reaction zones where proper estimation of the FMDF is critical. The application of variable weights allows the particle number density to be increased in the high temperature reaction zones without having to increase the number density outside this zone. At the initial time, the number density per grid cell of dimension $\Delta \times \Delta$, (denoted NPG) is invoked. For a given value of initial filtered density, the particle weights can then be assigned. Similarly, at an inflow boundary, the weights of the particles can be assigned based upon a specified particle number density and mass flux. The particle weight remains fixed during its life within the computational domain.

The chemical source terms in scalar equations are complex nonlinear functions of the thermodynamic and compositional variables. To evaluate these source terms in the M.C. solver, the fine grain values of the temperature (T^n) for all particles are calculated from the composition variable $\phi^n \equiv [Y_1^n, Y_2^n, \dots, Y_{N_s}^n, h^n]$ and the fine grain values of density (ρ^n) are determined from evaluation of the equation of state at a reference pressure $p_0 (= \rho^n \mathcal{R}^n T^n)$. The filtered pressure, $\langle p \rangle_{\ell}$ is obtained by the filtered equation of state, $\langle p \rangle_{\ell} = \langle \rho \rangle_{\ell} \langle \mathcal{R} T \rangle_L$. In this equation $\langle \rho \rangle_{\ell}$ is obtained from the F.D. solver and the correlation $\langle \mathcal{R} T \rangle_L$ is obtained by ensemble averaging of $\mathcal{R}^n T^n$ in the M.C. solver. In this procedure, the coupling between the hydrodynamic and the scalar fields is taken into account and allows the investigation of the effects of variable density.

The pressure ($\langle p \rangle_t$) field as determined by the above procedure exhibits some spatial oscillations. It is known that in PDF methods mean quantities calculated from particles are accompanied by statistical noise due to the finite sample size (Pope, 1985). Since spatial derivatives of $\langle p \rangle_t$ are required in the F.D. hydrodynamic solver, the oscillations can result in numerical difficulties. This is exacerbated by the nature of the fully compressible hydrodynamic code utilized in this work which allows these oscillations to propagate throughout the computational domain as spurious acoustic waves. Our results below show that while noise in the pressure field is noticeable, that of the compositional variables is not very significant. The amplitudes of the oscillations can be decreased by smoothing of the $\langle \mathcal{R}T \rangle_L$ field. An alternate procedure is to evaluate the correlation $\langle \mathcal{R}T \rangle_L$ by F.D. solution of its transport equation. The general form of this equation is complicated, involving two point correlations of scalars and temperature. At present this approach is investigated only for the case in which \mathcal{R} is constant. With this restriction, only the solution of the Favre filtered temperature equation is required. The reaction source term in this equation is evaluated from the M.C. solution. It is shown below that the statistics as determined by this procedure exhibit almost no spatial oscillations thus no smoothing is required. The results obtained from this procedure are identified by the label FMDF-2.

7 Results

7.1 Flows Simulated

The FMDF is employed for the simulations of the following flow configurations:

1. A two-dimensional (2D) temporally developing mixing layers.
2. A 3D temporally developing mixing layer.
3. A 2D spatially developing planar jet.
4. A 2D spatially developing mixing layer.

The two-dimensional simulations are conducted to allow extensive computations for assessing the consistency and accuracy of the FMDF and the convergence of the Monte Carlo

results. Both non-reacting and reacting flows are considered. Both the FMDF and LES-FD approaches are applied to the cases itemized in (1)-(3). Some of these cases are also treated by DNS, the results of which are used to assess the performance of the FMDF and LES-FD. Further appraisal is made by comparison with laboratory data for the flow under item (4).

The temporal mixing layer consists of two co-flowing streams traveling in opposite directions with the same speed (Riley *et al.*, 1986). The reactants \mathcal{A} and \mathcal{B} are introduced into the top and the bottom streams, respectively. The length in the streamwise direction is large enough to allow for the rollup of two large vortices and one (subsequent) pairing of these vortices. In 3D simulations, the length of the domain in spanwise direction is 60% of that in streamwise direction (Moser and Rogers, 1991). The layer is forced via both 2D and 3D forcing functions (Moser and Rogers, 1991; Miller *et al.*, 1994). The initial values of the reactants \mathcal{A} and \mathcal{B} at each spanwise location in 3D simulations are identical to those in the 2D simulations. In the figures presented below, x , y , z correspond to the streamwise, cross-stream and spanwise directions, respectively.

In the planar jet, the reactant \mathcal{A} is injected with a high velocity from a jet of width D into a co-flowing stream with a lower velocity carrying reactant \mathcal{B} (Steinberger *et al.*, 1993). The size of the domain in the jet flow is $0 \leq x \leq 14D$, $-3.5D \leq y \leq 3.5D$. The ratio of the co-flowing stream velocity to that of the jet at the inlet is kept fixed at 0.5. A double-hyperbolic tangent profile is utilized to assign the velocity distribution at the inlet plane. The formation of the large scale coherent structures are expedited by imposing low amplitude perturbations at the inlet. The frequency of these perturbations correspond to the most unstable mode and subharmonics of this mode as determined by linear stability analysis of spatially evolving disturbances (Michalke, 1965; Colucci, 1993). The characteristic boundary condition procedure developed by Poinso and Lele (1992) was used at the inlet. In this approach, the velocity and temperature variables are held fixed while the density is solved via its transport equation. The characteristic procedure facilitates evaluation of incoming waves which are necessary for the solution to the continuity equation. Zero derivative boundary conditions were used at the freestreams and the pressure boundary condition of Rudy and Strikwerda (1980) was used at the outflow.

To demonstrate the effectiveness of the FMDF approach under more realistic conditions, simulations of the laboratory experiments conducted by Mungal and Dimotakis (1984) were

performed. In these experiments, the turbulent combustion process was studied utilizing a planar shear layer to sustain a diffusion flame with one freestream containing diatomic hydrogen and the other containing diatomic fluorine. In both streams, the reactant gas was diluted in nitrogen. The intention of such simulations is to verify the ability of the FMDF approach to handle more complex chemical kinetic mechanisms and increased values of the physical parameters such as the Reynolds number. While the nature of turbulence is inherently three-dimensional, the present simulations are restricted to two spatial dimensions. This assumption is not too severe since the larger, resolved scales of the flow exhibit less three-dimensionality than the unresolved scales (Brown and Roshko, 1974).

In the hydrogen-fluoride mixing layer simulations, treatment of the hydrodynamic flow variables at all of the computational boundaries is similar to that of the spatially evolving planar jet as described earlier. In order to mimic a naturally developing shear layer, a modified variant of the forcing procedure suggested by Sandham and Reynolds (1989) was utilized. The cross-stream velocity component at the inlet is forced at the most unstable mode as well as 4 harmonics (both sub- and super-) of this mode. A spatial linear stability analysis was performed to determine the most unstable mode of the hyperbolic velocity profile imposed at the inlet. Sandham and Reynolds (1989) used a random phase shift to ‘jitter’ the layer. The form of this phase shift was applied by generating a uniform random number $-\varphi_{max} \leq \Delta\varphi \leq \varphi_{max}$ at each timestep and incrementing the phase by this amount. The effect of such a procedure is to prevent periodic behavior in the pairings of the large scale structures and allows the layer attain a higher degree of similarity downstream. The present approach considers a similar random phase shift, however, instead of utilizing a uniform distribution for the phase shift at each time increment, a discrete approximation of the Weiner process was applied:

$$\varphi(t^{n+1}) = \varphi(t^n) + \sqrt{2\sigma_\varphi^2 \Delta t} \eta_n, \quad (50)$$

where η_n is a Gaussian random variable with zero mean and unit variance. The quantity σ_φ^2 is the variance of the random process per unit time and controls the ‘drift’ of the process over time (the variance per *timestep* is $\sigma_\varphi^2 \Delta t$).

7.2 Reaction Mechanisms

For the flow configurations (1)-(3), the reaction scheme is of the type $\mathcal{A} + \mathcal{B} \rightarrow \mathcal{P}$ with an Arrhenius expression for the reaction rate:

$$S_{\mathcal{A}} = S_{\mathcal{B}} = -A_f(\rho A)(\rho B) \exp(-E_a/RT), \quad (51)$$

where A_f is the pre-exponential factor, E_a is the activation energy, and A , B denote the mass fractions of species \mathcal{A} , \mathcal{B} , respectively. This reaction rate may be expressed in non-dimensional form as:

$$S_{\mathcal{A}}^* = S_{\mathcal{B}}^* = -Da(\rho^* A)(\rho^* B) \exp(-Ze/T^*). \quad (52)$$

The asterisk denotes the non-dimensionalized variable normalized by its reference value. This effectively defines the Zeldovich and Damköhler numbers, Ze and Da , respectively:

$$Ze = E_a/RT_r, \quad (53)$$

$$Da = \frac{A_f \rho_r f_r}{U_r/L_r}, \quad (54)$$

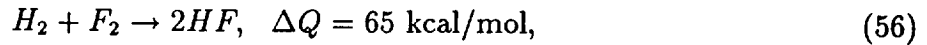
where ρ_r , T_r , U_r and L_r are reference density, temperature, velocity and length scale, respectively. Combustion exothermicity is parameterized by the non-dimensional heat release parameter Ce , defined as:

$$Ce = \frac{-\Delta h_P^0}{c_p T_r} \quad (55)$$

where Δh_P^0 is the heat of formation for the product \mathcal{P} . We note here that Ze and Ce are defined based on T_r , the same quantity used to non-dimensionalized the temperature field such that $T_r^* = 1$. Other authors have chosen an alternate convention (such as the adiabatic flame temperature) which results in a different numerical value of Ce and Ze for the same flow. Both constant rate ($Ze = 0$) and temperature dependent ($Ze \neq 0$) reactions are considered. The species $\mathcal{A}, \mathcal{B}, \mathcal{P}$ are assumed thermodynamically identical and the fluid is assumed to be calorically perfect.

The reaction mechanism associated with the experiment is more complicated and requires relaxation of some of the restrictions noted in the previous paragraph. The hydrogen-fluoride

reaction could be represented by the reaction (Mungal and Dimotakis, 1984)

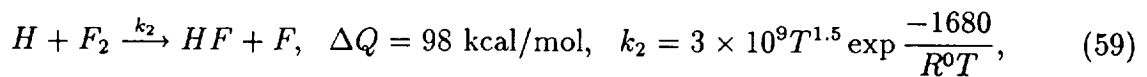
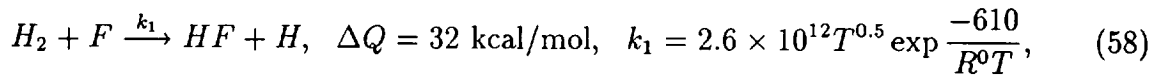


where ΔQ is the heat of reaction. The heat released in a mixture containing 1% mole fraction of F_2 and 1% mole fraction of H_2 diluted in nitrogen results in an adiabatic temperature rise of 93K above ambient (Mungal and Dimotakis, 1984). This reaction belongs to the more general family of hydrogen-halogen reactions:



in which Ha represents either F, Cl (chlorine), Br (bromine) or I (iodine). This group of flames has been extensively studied in the past (Chelliah, 1989) and has previously been used to test numerical methods for laminar flows undergoing combustion (Spalding and Stephenson, 1971).

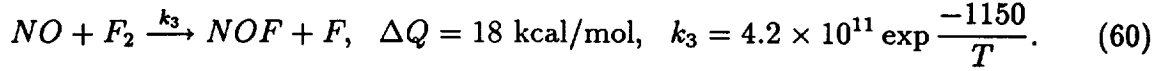
The global representation Eq. (56) is composed of a pair of second-order chain reactions (Mungal and Dimotakis, 1984):



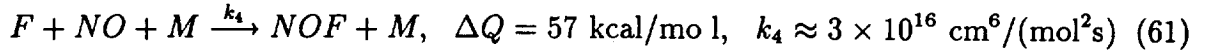
where the reaction rate constants k_1 and k_2 are given in units of $\text{cm}^3/(\text{mol s})$, T in K , and the universal gas constant R^0 in $\text{cal}/(\text{mol K})$. At low concentrations of the H atom, the reverse of the first of these two reactions is negligibly slow (Williams, 1985). Additionally, the rate data suggests that the reverse of the second reaction is also negligible as compared to the forward reaction (Chelliah, 1989).

The explosion limits for the hydrogen-fluorine reaction indicate that a mixture of these two gases at typical ambient conditions is stable (Chen *et al.*, 1975; Gmelin, 1980). Therefore, in order to initiate the reaction, a source of F atoms must be provided (Mungal and Dimotakis, 1984). Experimentally, this was accomplished by uniformly mixing a small amount of nitric

oxide with the hydrogen-nitrogen mixture. The nitric oxide mixes and reacts with the fluorine stream to produce free fluorine atoms:



The reverse of this reaction may be neglected (Rapp and Johnston, 1960). An additional reaction serves to limit the nitric oxide concentration (Baulch *et al.*, 1981; Cool *et al.*, 1970):



While it is necessary to add nitric oxide to initiate reaction, the addition of excessive amounts would deplete the availability of the free F atoms. Mungal and Dimotakis (1984) experimentally concluded that keeping the product of nitric oxide and diatomic fluorine molar concentrations to 0.03% resulted in rapid combustion. It was also noted by the authors that an increase of 50% in the nitric oxide concentration resulted in no appreciable changes in the temperature measurements. This suggests that for the conditions encountered in the experiment, the hydrogen-fluoride reaction can be well approximated by the limit of infinite rate chemistry.

Both finite and infinite rate FMDF calculations were undertaken. For the finite rate calculations, the 8 species, 4 reaction model based on Eqs. (58)-(61) was utilized. Due to the very fast rate of the hydrogen-fluoride reaction, compositional change due to reaction was implemented in 10 chemical timesteps for every hydrodynamic timestep. The computational cost associated with the high dimensionality as well as the large number of chemical timesteps motivated the investigation of infinite rate calculations. The application of infinite rate chemistry is a powerful tool in the analysis of LES flows in those cases in which it is justified. For a general nonlinear reaction mechanism, solution of a filtered conserved scalar alone is not sufficient to determine the *filtered* reactive scalars since the knowledge of the subgrid PDF of the conserved scalar is required to determine these quantities. The demonstrated utility of the FMDF approach coupled with infinite rate chemistry is an added objective of the present work.

7.3 Numerical Specifications

The results of numerical simulations are presented in three different sections. In section 7.4, the simulation results of the temporally developing mixing layer are used to demonstrate the consistency of the solution procedure for FMDF and the convergence of the Monte Carlo procedure for the solution of FMDF. In section 7.5, the simulation results of the 3D temporally developing layer and those of the 2D planar jets are used to appraise the performance of the FMDF in predicting DNS data. In section 7.6, the simulation results of the spatially evolving shear layer is used to assess FMDF via comparison with experimental data. All results in sections 7.4 and 7.5 are presented in non-dimensional form with normalization to reference quantities. In all temporal flows, the reference quantities are taken to be the freestream values, while in the spatially evolving flows, normalization is performed with regard to the high speed stream. The results in section 7.6 are presented in terms of dimensional quantities. In the presentation of the non-dimensional results the asterisks are dropped for brevity.

The magnitude of the flow parameters considered in DNS are dictated by the resolution which can be afforded. The primary parameters are the flow Reynolds number (Re), the Damköhler number (Da), the molecular Schmidt number (Sc) and the molecular Prandtl number (Pr). In all simulations $Sc = Pr = 1$. All finite difference simulations (in both DNS and LES) are conducted on equally-spaced, square ($\Delta x = \Delta y = \Delta$) grids. The highest resolution in DNS of the 2D temporal mixing layer consists of 433×577 grid points which allows reliable calculations at $Re = 11,200$ (based on the velocity difference and initial vorticity thickness), $Ce = 5$, $Ze = 8$, and $Da = 11.92$. The DNS of the 3D temporal shear layer is conducted with a resolution of $217 \times 289 \times 133$ with $Re = 2,240$, $Da = 1$ and $Ce = Ze = 0$. The DNS of the planar jet is performed on a 1201×601 grid and allows accurate simulations with $Re = 10,000$ (based on the centerline velocity at the inlet and the jet width), $Ce = 2.5$, $Ze = 8$ and $Da = 119.2$.

The FMDF and LES-FD are conducted on lower resolution than those used in DNS. The LES of the temporal mixing layer is conducted on a 55×73 grid for 2D simulations while resolutions of $37 \times 49 \times 23$ and $55 \times 73 \times 34$ are utilized in 3D. The LES of the spatial jet and hydrogen-fluoride mixing layer are conducted on a 201×101 grid. In addition to those cases which are assessed via comparison with DNS, several other temporal mixing layer cases

are considered to demonstrate the consistency between FMDF and LES-FD approaches as well as convergence of the Monte-Carlo methodology. These simulations are conducted using the same grid resolution and Reynolds number as outlined above. A top-hat filter function (Aldama, 1990) of the form:

$$G(\mathbf{x}' - \mathbf{x}) = \prod_{i=1}^2 \hat{G}(x'_i - x_i)$$

$$\hat{G}(x'_i - x_i) = \begin{cases} \frac{1}{\Delta_G} & |x'_i - x_i| \leq \frac{\Delta_G}{2} \\ 0 & |x'_i - x_i| > \frac{\Delta_G}{2} \end{cases} \quad (62)$$

is used with $\Delta_G = 2\Delta$. No attempt is made to investigate the sensitivity of the results to the filter function (Vreman *et al.*, 1994) or the filter size (Erlebacher *et al.*, 1992).

In both FMDF and LES-FD simulations, the subgrid stresses are modeled via the MKEV closure (Eq. (14)) unless specified otherwise. In the implementation of the MKEV, the magnitude of the reference velocity \mathcal{U}_i is set to zero in the cross-stream and spanwise directions and to the average of the high and low speed streams in the streamwise direction. Additionally, the ratio of the filter size at the secondary level to that at the grid level is $\Delta_{G'}/\Delta_G = 3$. The subgrid mass flux is modeled via Eq. (17). In all cases except that of the hydrogen-fluoride mixing layer, $Pr_t = Sc_t = 0.7$. No attempt is made here to determine the magnitudes of the constants appearing in these models in a dynamic manner (Germano, 1992). In all simulations $C_{I1} = C_{I2} = 0.006$. The magnitudes of C_{R1} and C_{R2} are given below. The subgrid mixing model requires the input of the constant C_Ω in the mixing frequency which also determines the SGS variances. A value of $C_\Omega = 4$ is used in most simulations. Application of these values for Sc_t , Pr_t and C_Ω in the hydrogen-fluoride configuration resulted in a notably low temperature rise compared to the results observed in the experiment. To increase the subgrid diffusion and mixing, a slightly lower value of $Sc_t = Pr_t = 0.5$ and increased value of $C_\Omega = 6$ were invoked. This set of constants yield a more favorable temperature rise. At this point, it is unclear whether these modifications indicate a lack of robustness in the estimation of the mixing frequency or if the low temperature rise is due to the lack of three dimensionality and small scales in the two-dimensional simulation. Additionally, it is noted that the mean temperature rise was found be sensitive to the forcing at the inlet.

In the FMDF of temporal mixing layer, the particles are initially distributed throughout the computational region. In the FMDF of the jet, the particles are supplied only in the region $-1.75D \leq y \leq 1.75D$. For the temporal shear layer, the initial value of NPG (defined earlier) is varied to assess its affect on statistical convergence. The size of the “ensemble domain” is also varied to assess its influence. The following sizes are considered: $\Delta_E = 2\Delta$, Δ . The number of samples used to construct the FMDF is thus controlled by selection of NPG and Δ_E . In some of the planar jet simulations and all of the hydrogen-fluoride mixing layer simulations, variable weights (as outlined earlier) are employed to decrease the overall computational expense. All other simulations utilize uniform weights. In the temporal mixing layer, due to flow periodicity in the streamwise and spanwise directions, if the particle leaves the domain at the right or the left boundary, new particles are introduced at the other boundary with the exact same compositional values. In the spatially evolving jet and mixing layer, new particles are introduced at the inlet at a rate corresponding to the desired (imposed) local particle number density and fluid velocity. With prescription of the filtered fluid density, the particle weight is adjusted to yield the proper mass flux across the boundary. Finally, the compositional makeup (reactant mass fractions and enthalpy) is imposed with a hyperbolic tangent dependence on the cross-stream coordinate.

In application of the FMDF approach to the experimental configuration, the length scale used in the non-dimensionalization is taken to be 45.7 cm, corresponding to the distance from the virtual origin to the position downstream at which the experimental measurements were taken. The computational domain encompassed a rectangular region 1.2 by 0.6 nondimensional units so as to decrease the effect of the outflow boundary condition at the (non-dimensional) position $x = 1.0$ coinciding with the location of the measurement apparatus in the experiment. Initial discretization of the FMDF was accomplished with 5 particles per grid cell in the freestreams, peaking to a value of 30 at the level of the splitter plate ($y = 0$), corresponding to a initial number density from 20 to 120 sample points per ensemble for an ensemble domain size of $\Delta_E = 2\Delta$. The composition (reactant mass fractions and enthalpy) of incoming particles was set according to composition of the fluid at the point of entry with a hyperbolic tangent profile used to assign the inlet composition variables. The velocity scale was taken to be that of the fast stream (22 m/s), with a velocity ratio of 0.4. The Reynolds number based on the downstream measurement location was taken to be 4.0×10^5 , consistent with the experimental value.

Due to the low Mach number of the experiment, very small timesteps are required to satisfy the CFL condition required by the compressible hydrodynamic solver. Additionally, such compressible solvers become sensitive to numerical instabilities at low Mach numbers. In order to alleviate these problems, the Mach number in the simulation was artificially increased by a factor of 5 while holding the Reynolds and Damköhler numbers fixed. This was accomplished by increasing the velocity reference scale by a factor of 5 and decreasing the reference length scale by a factor of 5. In order for the nondimensional reaction rate to be the same, the reaction rate constants k_1 through k_4 were increased by a factor of 5^2 . The result is an increase of the Mach number from 0.07 to 0.35 while maintaining the same Reynolds and Damköhler numbers. Since the experimental Mach number as well as the simulated Mach number are low enough such that compressibility effects on the flowfield are negligible, this procedure is justified. Any wave related phenomena is of course not properly simulated, however they have little effect on the hydrodynamics and are not of any interest in the present work. Dilatational effects due to heat release are not affected by this approximation and are properly accounted for. Furthermore, the filtered pressure was obtained by measuring the subgrid Favre correlation $\langle \mathcal{RT} \rangle_L$ from the M.C. solver and multiplying by the filtered density provided by the F.D. solution to the continuity equation. A minimal degree of smoothing of $\langle \mathcal{RT} \rangle_L$ consisting of a local box filter 3×3 grid points with equal weights was used to minimize the magnitude of pressure oscillations throughout the flowfield. Only the FMDF-1 formulation was utilized in the experimental comparison.

The simulated results are analyzed both “instantaneously” and “statistically.” In the former, the instantaneous contours (snap-shots) and the scatter plots of the scalar values are considered. In the latter, the “Reynolds-averaged” statistics constructed from the instantaneous data are calculated. In 2D temporal mixing layer, the flow is homogeneous in the x -direction; thus the statistics are constructed by the ensemble from all the grid points in the streamwise direction. These statistics are y dependent. In 3D shear layer the flow is homogeneous in x and z directions therefore statistical are evaluated by averaging in both these directions. In some cases, the x -averaged statistics are presented at several different z locations to illustrate the three dimensional effects. In the spatially developing mixing layer and jet flows the averaging procedure is conducted via sampling in time. These statistics are $y - t$ dependent. All Reynolds averaged results are denoted by an overbar.

7.4 Consistency of FMDF

The objective in the results presented in this subsection is to demonstrate the consistency of the FMDF formulation. For this purpose, the LES results via FMDF and LES-FD are compared against each other in 2D and 3D temporal mixing layers under different conditions. Since the accuracy of the finite difference procedure is well-established, this comparative analysis provides a means of assessing the performance of the Monte Carlo solution of the FMDF.

In all simulations MKEV model is used to calculate the eddy viscosity with $C_{R2} = 0.02$. Unless otherwise mentioned, in 2D simulations $NPG = 50$ and in 3D simulations $NPG = 20$ at locations that $\langle \rho \rangle_\ell = 1$. Also, in all 2D simulations $\Delta_E = \Delta$ and in all 3D simulations $\Delta_E = 2\Delta$ unless specified otherwise.

2D Simulations

Simulations of 2D layers are conducted in which the flow is initiated with a nonuniform distribution of density and temperature. The initial filtered density is distributed as a “spike” in the middle of the layer (Fig. 1(a)). The reaction rate in this simulation is zero. The flow that starts with this condition evolves quite differently in comparison to one which starts with a uniform density distribution (Colucci, 1993). With uniform weights assigned to the Monte-Carlo particles, the particle number density must remain proportional to the fluid density. This is observed in Fig. 1(a) where it is demonstrated that the filtered density calculated from the Monte-Carlo particles ($\langle \rho \rangle_\ell = (\langle 1/\rho \rangle_L)^{-1} = 1/(\frac{1}{N_E} \sum_{n \in \Delta_E} \frac{1}{\rho^n})$, where N_E is the total number of particles involved in ensemble averaging) matches exactly with that of finite difference values calculated at the Eulerian grid points. Figure 1(b) shows that at the final time of the simulation (when the flow has experienced the pairing of two neighboring vortices) the Reynolds averaged filtered density calculated from finite difference and Monte-Carlo approaches are very close. While there are some oscillations in the particle number density due to finite number of particles and the stochastic nature of the Monte Carlo procedure, this quantity is still highly correlated with the fluid density.

Figure 2 shows the temporal evolution of the vorticity thickness (δ_v) for the cases in which the values of the filtered density are either initially uniform or distributed as a spike. When the

flow starts with uniform density, the effect of thermodynamic quantities on the hydrodynamics is negligible and δ_ρ as obtained by FMDF-1 and FMDF-2 are identical. Comparatively, with an initial density spike, the growth of the layer is damped. Nevertheless, the results obtained by FMDF-1 are very close to those obtained by FMDF-2. The slight difference between the results predicted by these two methods are attributed to the differences in the numerical procedures. The results obtained from high resolution DNS indicate that the growth of layer is reasonably well predicted by the LES schemes.

In Fig. 3, the contour plots of the resolved vorticity and temperature at the final time ($t = 44$) as obtained by FMDF-1 and FMDF-2 are shown. Figure 3 provides a visual demonstration of the consistency of the FMDF as the results via the hybrid F.D. - M.C. scheme (FMDF-1) are in agreement with those obtained by F.D. (FMDF-2). There are some oscillations in the results obtained by FMDF-1. Comparatively, these oscillations are nearly eliminated in FMDF-2. An interesting observation in Fig. 3 is that there are significant positive vorticity values in the flow field. These positive values are created by the baroclinic term and are also observed in DNS.

To determine the extent of noise accompanying the statistical quantities, the Reynolds averaged values of the resolved pressure, temperature, energy and conserved scalar are shown in Fig. 4. This figure indicates that the results based on FMDF-1 are very close to those obtained via FMDF-2. The most significant difference between these results is in filtered pressure which exhibits appreciable oscillations in FMDF-1 (Fig. 4(a)). To reduce the pressure fluctuations, a local least square filter function is applied to smooth the $\langle T \rangle_L$ values as obtained from the Monte Carlo particles. This operation reduces the oscillations in $\langle p \rangle_t$ noticeably as shown in Fig. 4(a) and does not have a significant influence on the other statistical quantities. Figures 4(b)-4(d) show that the filtered values of the resolved scale energy, temperature and conserved scalar as obtained by FMDF-1 are very close to those predicted by FMDF-2. Several other filter functions has also been employed to smooth $\langle T \rangle_L$. The effect of these filter functions on the flow field is demonstrated in Fig. 5, where the difference between calculated values of $\langle p \rangle_t$ via FMDF-2 and FMDF-1 with smoothing are shown. In all cases, the difference in $\langle p \rangle_t$ is very small (less than 2%). The most significant difference between the pressure fields occurs when no smoothing operation is applied to $\langle T \rangle_L$ in FMDF-1. The results in Fig. 5 also show that the difference between the pressure fields is

significantly decreased as the number of employed particles is increased.

To demonstrate the consistency between the FMDF and moment closure (LES-FD) approaches, comparison between the moments of a conserved scalar calculated from the Monte-Carlo particles and those generated by LES-FD is made. This is observed in Fig. 6 where contour plots of the Favre-filtered value of scalar \mathcal{A} are presented. In the results presented in Fig. 6 and also in those in Figs. 7 and 8, the Favre filtered temperature in FMDF is calculated from Monte Carlo particles (FMDF-1) and no smoothing operation is performed. Figure 6 clearly indicates the results obtained by FMDF are strikingly similar to those obtained by LES-FD. Similarly, Fig. 7 is a plot of the Reynolds averaged first and second subgrid Favre moments. Figure 7(a) shows the comparison of FMDF and LES-FD results for $\overline{\langle A \rangle}_L$ for different values of Δ_E and NPG . The agreement in the first moment is quite good even for large values of Δ_E . This is particularly important as the Favre-filtered scalar is required in the mixing model. The difference between the FMDF and LES-FD results is more apparent in Fig. 7(b) where the cross-stream variation of $\overline{\sigma_A^2}$ for different Δ_E and NPG are considered. It is observed that FMDF overpredicts the values of the second moment. However, the difference between FMDF and LES-FD diminishes as Δ_E decreases. This is consistent with the results obtained in constant density flows (Colucci *et al.*, 1997).

The consistency between FMDF and LES-FD as established above is only valid in nonreacting flows. In reacting flows, the reaction term in FMDF transport equation is closed but the corresponding terms in the moment equations require modeling. This lack of consistency is demonstrated in Fig. 8 where simulations of a uniform density reacting temporal mixing layer with $Da = 2$ and $Ce = Ze = 0$ are considered. In these simulations, the LES resolution is lowered to 37×49 and $Re = 2,800$. The product thickness (δ_p) from FMDF and Favre-filtered DNS are nearly identical. Comparatively, in the absence of a reaction closure, the product formation in LES-FD is significantly higher. Also shown in Fig. 8 are the results calculated from the filtered density function (FDF) (Colucci *et al.*, 1997). The results obtained from FMDF and FDF are quite close, indicating the consistency of FMDF with FDF formulation in the limit of zero density variations.

3D Simulations

To further demonstrate the consistency between the FMDF and LES-FD methodologies,

large eddy simulations of 3D temporal shear layers are conducted. In these simulations the initial density and temperature profiles are distributed as a “spike”, similar to that in the previous 2D simulations.

The results of 3D simulations with 2D forcing are similar to those obtained via 2D simulations. To demonstrate this similarity, in Fig. 9 the cross-stream variation of the filtered density averaged over the x direction at several different z locations as obtained by FMDF-2 is shown. The values are calculated from the Monte- Carlo particles (M.C.) and finite difference procedure (F.D.). Figure 9 demonstrates that the filtered density profiles at different spanwise locations are similar to each other and to the results shown in Fig. 1(b) for 2D simulations. All other statistics were observed to exhibit similar two-dimensional behavior. Consistent with the 2D simulations, Fig. 9 further indicates that there is an excellent agreement between the filtered density calculated from M.C. and F.D. The agreement obtained by the different methods is better illustrated in Fig. 10, where scatter plots of $\langle T \rangle_L$ and $\langle A \rangle_L$ as calculated by M.C. and F.D. are shown. It is observed that the local values of $\langle T \rangle_L$ and $\langle A \rangle_L$ calculated from Monte Carlo particles are highly correlated with those calculated by the finite difference method. The correlation coefficients among the data presented in Figs. 10(a) and 10(b) are 0.998 and 0.993, respectively.

The statistics calculated from simulations with 3D forcing exhibit significant variations along the spanwise direction. This is observed in Fig. 11, where the cross-stream variation of the x -averaged streamwise vorticity and pressure at several z locations obtained by FMDF-1 and FMDF-2 are shown. The results in Fig. 11(a) indicate that the filtered vorticity calculated by FMDF-1 is very close to that calculated by FMDF-2. The filtered pressure obtained from FMDF-1 also exhibits similar trends to that obtained from FMDF-2, however, the noise in the pressure field as calculated by FMDF-1 is appreciable. Despite the obvious effect of this noise on the pressure field, the filtered scalar and temperature values as calculated by M.C. are consistent with those calculated by F.D. This is illustrated Fig. 12 in which scatter plots of $\langle T \rangle_L$ and $\langle A \rangle_L$ are shown. The results in Fig. 12(a) indicate that the local values of $\langle T \rangle_L$ calculated from Monte Carlo particles are very close to those calculated by finite difference method. Furthermore, there is a high correlation between the local values of $\langle A \rangle_L$ calculated from the Monte-Carlo particles and finite difference (Fig. 12(b)). The correlation coefficients among the data presented in Figs. 12(a) and 12(b) are 0.999 and 0.999, respectively.

7.5 Validations via DNS

The objective of this section is to assess the overall performance of FMDF methodology, to appraise the validity of the submodels employed in the FMDF transport equation, and to demonstrate the capabilities of FMDF for LES of complex exothermic chemically reacting turbulent flows. For this objective, the FMDF results are compared against DNS of the same flow configuration with the same magnitudes of the physical parameters (Re , Da etc...). For meaningful comparison, the DNS data is filtered and down-sampled onto coarse grids corresponding to the resolution used in FMDF. At this point it should be emphasized that FMDF is not intended to be an alternative to DNS, rather the comparison is made to assess the performance of the FMDF approach. The value in the FMDF approach lies in its applicability to more “practical” systems which are incapable to be treated by DNS. To illustrate the capability of the FMDF, the results are also compared with LES-FD in which the effects of SGS fluctuations on the filtered reaction rate are ignored. The results of two- and three-dimensional simulations are discussed in different subsections. First the results for the 2D temporal shear layer and 2D planar jet are presented. This is followed by the 3D temporal shear layer results. Unless otherwise specified, all FMDF calculations presented in this section utilize the FMDF-2 formulation.

2D Simulations

To quantify the performance of the FMDF methodology in the case of heat release, simulations of a temporal mixing layer undergoing exothermic chemical reaction are conducted. In Fig. 13(a), the FMDF predictions of the product thickness are compared with DNS results. The cross-stream variation of the product mass fraction averaged over streamwise direction at $t = 44$ are shown in Fig. 13(b). The FMDF results are calculated with both $\Delta_E = \Delta$ and $\Delta_E = 2\Delta$. The results obtained by LES-FD are also presented to demonstrate the importance of the SGS scalar fluctuations. Figure 13(a) indicates that the values of the product thickness predicted by FMDF are reasonably close to those of DNS. The size of the ensemble domain used to calculate the Favre-filtered statistics from particles does not have significant influence on the magnitude of the product thickness. Additionally, the results in Fig. 13(a) illustrate that the neglect of SGS correlations results in significant overpredictions of the product mass fraction. This behavior is observed at all times and is consistent

with that in Reynolds averaging (Libby and Williams, 1980). The results shown in Fig. 13(b) further illustrate these trends. While the cross-stream product distribution obtained in DNS and FMDF with either $\Delta_E = \Delta$ or $\Delta_E = 2\Delta$ are in good agreement, that predicted by LES-FD is significantly higher. It is expected that the deviation between DNS and LES-FD results would increase as the magnitude of the Damköhler number and/or Reynolds number increases (Colucci *et al.*, 1997). In the majority of “practical” reacting systems, the magnitudes of the Damköhler and Reynolds numbers are considerably large. Therefore it is expected that the effects of the SGS correlations would be highly pronounced in such applications.

In combustng flows, the reaction rate is typically a strong function of temperature. Therefore accurate prediction of the scalar field relies on the proper assessment of the temperature. In Fig. 14 the cross-stream variation of the filtered temperature (averaged over the x direction) for DNS, FMDF and LES-FD at $t = 44$ are shown. This figure shows that for this flow with significant variations in temperature due to heat release, the averaged filtered temperature is reasonably well predicted by FMDF. In contrast, LES-FD yields a significant overprediction in the product formation, indicating the importance of the SGS scalar and temperature fluctuations. Furthermore, it is demonstrated in Fig. 14 that the filtered temperature as obtained from M.C. particles is nearly identical with that obtained by the F.D. solution.

Accurate prediction of the filtered temperature field is also critical in evaluation of the velocity field. In the cases considered here the heat release associated with the reaction has a significant influence on the hydrodynamics. This is observed in Fig. 15 where it is shown that the vorticity thickness (δ_v) calculated by DNS is significantly decreased due to heat release. Figure 15 also shows that the vorticity thickness obtained from FMDF exhibits similar trends to those of DNS. Nevertheless, in both heat releasing and non-heat releasing cases, FMDF underpredicts the DNS values due to inaccuracy of the models for SGS stresses. The inaccuracy of the SGS stress models has a noticeable effect on the development of the flow in the transitional period of its evolution and is the primary reason for the slight differences between the DNS and FMDF results in Figs. 13 and 14.

The effectiveness of the FMDF to predict the slightly more complex jet flow is summarized in Figs. 16-21. As described above, in the treatment of exothermic flows, 3 different methodologies for dealing with the filtered pressure are employed. In each procedure, the filtered

density obtained from the finite difference solution of the filtered equations is used in the equation of state. In the first approach, the Favre-filtered temperature obtained by ensemble averaging over the Monte-Carlo particles is used to evaluate the filtered pressure (FMDF-1). Due to the statistical noise of the finite samples utilized to calculate mean quantities, the resulting pressure field suffers from oscillations. This is demonstrated by a snapshot of the flowfield in Figs. 16(a) and 17(a) in which contours of the pressure and temperature for exothermic reacting simulations are displayed. This behavior is amplified by the fact that the resulting pressure field is differentiated in the momentum equations and the finite difference solver is acoustic in nature. In an attempt to reduce this oscillatory behavior, a local box filter is applied to smooth the temperature. Figure 16(b) demonstrates that the pressure fluctuations in the resulting flowfield are reduced significantly. Furthermore, additional diffusion due to the smoothing nature of the box filter is apparent, especially in the temperature contours (Fig. 17(b)). The third approach considers the evaluation of the Favre filtered temperature by considering its transport equation (FMDF-2). The subgrid correlations appearing as the source term in this equation are obtained from the FMDF solver. The resulting pressure field, depicted in Fig. 16(c), is nearly free of pressure oscillations. The temperature values evaluated via this procedure are also free of noise (Fig. 17(c)). It is to be noted that in the present simulations, the gas constant of the mixture is assumed constant and any mass fraction-temperature correlations in the filtered equation of state are identically zero. The numerical treatment of these correlations due to variable mixture gas constant is the focus of our current investigation.

It has been shown in Fig. 1 that in the nonreacting density-stratified mixing layer, the Reynolds averaged values of the particle number density correlate with the filtered fluid density. Similarly, Fig. 18 shows that in reacting planar jet simulations the instantaneous particle number density and the filtered fluid density as calculated by FMDF are reasonably correlated. The results considered in Figs. 1 and 18 correspond to cases in which the particles have uniform weights. Of particular interest in Fig. 18 is that the particle number density is lowest in the high temperature reaction zones. To assess the effectiveness and accuracy of the variable weight procedure, simulations of a reacting planar jet identical to that in Figs. 16-18 but with variable particle weights are conducted. Particles are introduced at the inlet based on a specified number density which is lowest in the freestreams and peaks at the reaction zones. The resulting particle number density, sum of particle weights, and

filtered fluid density calculated by FMDF are shown in Fig. 19. It is observed in Fig. 19(a) that downstream there is a higher proportion of particles in the reaction zones relative to the case with uniform weights. The sum of the particle weights as shown in Fig. 19(b) is reasonably correlated with the filtered fluid density (Fig. 19(c)). A comparison between Figs. 18(b) and 19(c) indicate that despite the significant difference in the total number of particles and particle weighing procedures, the filtered density fields are nearly identical in the two simulations. The computational time in the case with variable weights is lower than that in the case with equal particle weighting by nearly a factor of two.

The similarity of the results obtained with uniform and variable particle weighting procedures is further demonstrated in Fig. 20(a) where the variation of the integrated product thickness with the downstream coordinate is shown. Also shown in this figure is the product thickness as obtained from DNS and LES-FD. It is observed that LES-FD substantially overpredicts the amount of product in comparison to the filtered DNS data. The FMDF results are much closer to those of DNS. Further comparison between DNS, FMDF and LES-FD results is made Fig. 20(b) where the time-averaged profile of the product variation in y direction at $x/D = 14$ is shown. Similar to the conclusions drawn from Fig. 20(a), it is observed that the amount of product predicted via LES-FD is significantly higher than that of DNS while the FMDF results are close to DNS values.

The ability of the FMDF to capture the effects of chemical reaction lies in its ability to resolve the scalar and temperature correlations without modeling. These correlations constitute an important contribution to the filtered reaction rate. To demonstrate this, in Fig. 21, contour plots of the SGS “unmixedness”, defined as $\langle S(\phi) \rangle_I - S(\langle \phi \rangle_L)$, from both DNS and FMDF are shown. A comparison between the results shown in this figure clearly indicate that the SGS unmixedness calculated by FMDF is in very good agreement with that of DNS. Comparatively, this term is effectively ignored in LES-FD. The contribution of the SGS unmixedness to the total filtered reaction rate is expected to increase as the flow Reynolds and Damköhler numbers increases. Therefore, it is expected that the difference between DNS and LES-FD results increase as Reynolds and/or Damköhler numbers increase.

3D Simulations

The major conclusions drawn from the 2D results are confirmed in 3D simulations. To

build upon the results obtained from the two-dimensional simulations, DNS and LES of three-dimensional temporal shear layer flow are conducted. The temporal evolution of the product thickness as predicted by FMDF is compared with DNS and LES-FD results in Fig. 22 for both low and high LES resolutions. Figure 22(a) illustrates the importance of the SGS unmixedness in 3D flows, as the product thickness obtained from LES-FD is appreciably higher than that predicted by DNS. Consistent with the results of the 2D simulations, the product thickness predicted by FMDF with MKEV model are close to those of DNS. Also shown in Fig. 22(a) are the FMDF results obtained using the Smagorinsky model as the SGS stress closure. The accuracy of the Smagorinsky model for this transitional flow is less than that of the MKEV model as the product thickness values obtained by FMDF with Smagorinsky closure compare less favorably to the DNS results than those obtained by FMDF with the MKEV model. The results shown in Fig. 22(b) for higher LES resolutions resemble those shown in Fig. 22(a) for lower LES resolution. Again LES-FD significantly overpredicts the DNS results while the results obtained from FMDF using the MKEV model yields a more favorable comparison. Expectedly, the difference among DNS, LES-FD and FMDF results decrease as the resolution in LES increases.

To further demonstrate the capabilities of FMDF, in Fig. 23 the cross-stream variations of the filtered product mass fractions for DNS, LES-FD and FMDF at $t = 44$ are shown. The product values reported in Fig. 23(a) are obtained by averaging the instantaneous results over x and z directions. To illustrate the three-dimensionality of the flow, the product mass fractions averaged over x direction at two different z locations are presented in Fig. 23(b). Consistent with the results shown in Fig. 22, it is observed that the product mass fractions are significantly overpredicted by LES-FD, again indicating the importance of the SGS scalar correlations. The product mass fraction predicted by FMDF as shown in Fig. 23(a) are in agreement with that of DNS. The FMDF reasonably predicts the product mass fractions for several spanwise locations demonstrating the enormous potential of the FMDF for LES of three-dimensional complex turbulent reacting flows.

A common feature of the results shown in Fig. 23 is that the dispersion of the product values along the cross-stream direction is slightly underpredicted by FMDF. The reason for this behavior is that the SGS stress and scalar flux models are not entirely accurate and result in underprediction of the growth of the layer. This is illustrated in Fig. 24, where it

is shown that for different filter sizes (different LES resolution) the temporal evolution of the vorticity thickness (δ_v) as predicted by FMDF with the MKEV model are lower than that predicted by DNS. Expectedly, as the resolution of FMDF is increased, the results better compare with DNS. The vorticity thickness predicted by FMDF using the Smagorinsky model are also considered in Fig. 24. It is shown that the vorticity thickness predicted by FMDF with the MKEV model predicts the DNS data much better than that via FMDF with the Smagorinsky closure. It is well established that the Smagorinsky closure generates excessive damping on the resolved scales in transitional regions (Zang and Piomelli, 1993) which, consequently, yields wrong prediction of the growth rate of the shear layer. The improved prediction of the eddy viscosity also results in more accurate prediction of the product formation by FMDF as illustrated in Fig. 22. This is primarily due to the role of the eddy viscosity in the determination of the subgrid mixing frequency.

Computational Requirements

To evaluate the computational cost of FMDF, the computational times associated with the simulations of 2D reacting planar jet and 3D reacting mixing layer are shown in tables 1 and 2, respectively. The overhead of the FMDF simulation is somewhat extensive as compared to LES-FD; nevertheless the running time for FMDF simulation is significantly less than that of DNS. While this overhead is tolerated in present simulations, there are several means of reducing it for future applications. For example the Lagrangian procedure would benefit from the utilization of parallel architecture, since a significant portion of the time is devoted to computations in large loops dimensioned by the total number of Monte Carlo particles. This has been discussed for use in PDF methods (Leonard and Dai, 1994) and its utilization in FMDF methods is encouraged. Again it is emphasized that FMDF is not intended to be an alternative to DNS. The value in the FMDF approach lies in its applicability to more “practical” systems which are incapable to be treated by DNS.

7.6 Validations via Laboratory Data

In the experiments of Mungal and Dimotakis (1984), several runs involving different equivalence ratios were undertaken to elucidate the effect of this parameter on the product for-

Table 1: The computational times for 2D planar jet simulations.

Simulation	Grid resolution	Normalized CPU time†	Figure
DNS	1201 × 601	242.5	20, 21
FMDF	201 × 101	7.62	19-21
LES-FD	201 × 101	1	20

† Unit correspond to 760 seconds on a Cray-C90.

Table 2: The computational times for 3D shear layer simulations.

Simulation	Grid resolution	Normalized CPU time†	Figure
DNS	217 × 289 × 133	182.71	22(b)
FMDF	55 × 73 × 34	7.64	22(b)
LES-FD	55 × 73 × 34	1	22(b)

† Unit correspond to 655 seconds on a Cray-C90.

mation. The authors define the equivalence ratio of the low speed freestream reactant concentration c_{02} to the high speed freestream value c_{01} divided by the low speed to high speed stoichiometric ratio:

$$\phi = \frac{c_{02}/c_{01}}{(c_{02}/c_{01})_s} = c_{02}/c_{01}, \quad (63)$$

noting that the stoichiometric ratio is unity for the hydrogen-fluorine reaction. In all of the runs, the fluorine mole fraction was kept at 1% while the hydrogen mole fraction was varied at 1%, 2%, 4% and 8%. With the fluorine on the high speed side, this allows for equivalence ratios of 1, 2, 4 and 8. ‘Flip’ experiments were conducted in which runs with inverse values of the equivalence ratio were conducted ($1, \frac{1}{2}, \frac{1}{4}$ and $\frac{1}{8}$). These were carried out by moving the 1% fluorine mixture to the low speed stream and the hydrogen mixture to the fast speed stream.

Figure 25 displays contour plots of (a) the instantaneous temperature field and (b) the time averaged temperature field for a stoichiometric ratio of unity (1% fluorine on the high speed side and 1% hydrogen on the low speed side). In this simulation, the 8 species, 4 reaction finite rate chemical mechanism was utilized. Clearly evident in this figure is the presence of large scale coherent structures. Note that the peak temperature in the instantaneous field approaches, but is somewhat lower than the adiabatic flame temperature. Since the

chemistry is sufficiently fast, finite rate effects do not offer an explanation; rather the cause is explained by the nature of the filtering process. In contrast to the instantaneous temperature field, the peak values of the time averaged field are considerably lower than that of the adiabatic flame temperature, an intuitive fact noted previously by the authors as well as by others (Wallace, 1981). It is noted that a large number of individual particles (i.e. 'realizations') do indeed approach the adiabatic flame temperature, a result reflected in Fig. 26 which is a scatter plot of the particle temperature against the mixture fraction Z where

$$Z = \frac{c_{H_2} + c_{F_{2\infty}} - c_{F_2}}{c_{H_{2\infty}} + c_{F_{2\infty}}}. \quad (64)$$

The presence of large scale structures in shear layers has been widely recognized (Brown and Roshko, 1974; Papamoschou and Roshko, 1986). Evidence of such structures in the present experiment is presented in the form of Schlieren photographs as well as temperature histories at several cross stream positions. Figure 27 is a corresponding time history of temperature at various cross stream locations calculated by the simulation. Each vertical increment represents temperatures ranging from ambient to the adiabatic flame temperature. Qualitatively, these time traces are strikingly similar to those generated in the experiment. One notable difference is that in the vicinity of the middle regions of the layer, there are points in time that the simulation exhibits near ambient temperature (cool fluid). While there is some evidence in the experiment, it is considerably more prevalent in the simulation. This is partially believed to be a consequence of the two dimensional nature of the simulation. Comparatively, the true three dimensional behavior exhibits smaller scales which tend to more effectively homogenize the fluid locally and prevent the presence of purely ambient fluid in this region. For this reason it is expected that the minimum values of the time averaged temperature in the vicinity $y = 0$ are slightly lower than those from the experiment. It is expected that a fully three dimensional FMDF simulation would alleviate this shortcoming. Another significant cause of this discrepancy noted by the authors is that the cold wire probes suffer from appreciable thermal lag and conduction error which tend to cause a 'smoothing' effect.

In an effort to assess the capability of the simulation to quantitatively predict the experimental results, Fig. 28 shows plots of the time averaged temperature as a function of the

cross stream coordinate at the downstream measuring station. In this figure, the cross stream coordinate is normalized with the 1% temperature thickness, δ_1 , defined as the distance between the points at which the cross stream mean temperature rise is 1% of the maximum mean temperature rise. The comparison between the experimentally measured values and those generated by the simulation procedure is favorable. Also in this figure is a plot of the mean temperature generated by the FMDF approach with the infinite rate reaction model. As expected, the infinite rate approach agrees quite well with the finite rate reaction mechanism. A considerable savings in computational time as well as memory is gained in the infinite rate approach, owing to the fact that only one passive scalar needs to be transported. Additionally, while 10 chemical time steps per hydrodynamic time step were required in the finite rate approach, the conserved scalar is not altered by the effects of reaction, eliminating the necessity for such expensive time splitting. As a result, while the finite rate code took 12,700 cpu seconds on a Cray C-90, the infinite rate code used only 1,990 cpu seconds on the same machine. With confidence in the infinite rate model, the remainder of the hydrogen-fluoride simulations were conducted using this approach.

To demonstrate the 'flip' effect noted in the experiment, Fig. 29 shows the cross-stream temperature variation for $\phi = 8$ and $\phi = \frac{1}{8}$. Two primary observations are consistent with the findings of the experiment: (1) the peak value of the mean temperature differs although the adiabatic flame temperature is the same and (2) the peak value 'shifts' toward the lean reactant stream. Clearly, since the only difference between the two runs is the interchange of the low and high speed reactants, the mechanism for this observation lies in the fluid mechanics. An explanation is offered by Mungal and Dimotakis (1984) in the context of the Broadwell-Breidenthal theory (Broadwell and Breidenthal, 1982). This theory based upon the fact that the entrainment ratio differs from unity due to the non symmetric nature of the velocity profile (the entrainment ratio is defined as the ratio of the volume of high speed fluid to the volume of low speed fluid mixed within the layer). An additional explanation is presented based upon the PDF's of Konrad (Konrad, 1977; Broadwell and Breidenthal, 1982). In this approach, the flipping effect is attributed to the fact that the Konrad PDF's have peaks near $\mathcal{E}/(1 + \mathcal{E})$, where \mathcal{E} is the entrainment ratio. Regardless of the theoretical explanation, the important feature is that the FMDF simulation is capable of capturing the phenomena observed in the experiment.

Absolute temperature profiles for all equivalence ratios are presented in Fig. 30(a). These results exhibit characteristics similar to those presented in the experimental investigation. Most notable is the tendency of the flame to favor the lean reactant side as discussed above. Additionally, with the exception of the two cases for $\phi = 1$, the peak temperature is higher for equivalence ratios greater than one compared to the reciprocal equivalence ratio, a generalization of the result discussed in the previous paragraph. Normalized mean temperature profiles are presented in Fig. 30(b). Consistent with the experiment, the peak normalized temperature reaches a maximum between the values of 1 and 2 for the equivalence ratio. These trends are more clearly portrayed in Fig. 31(a), which Mungal and Dimotakis (1984) refer to as 'inferred' temperature profiles. These plots are modified to reflect the temperature if the high speed reactant was fixed at 1 % molar concentration while the low speed stream was varied from $\frac{1}{8}\%$ through 8% to obtain the desired equivalence ratios. This figure clearly supports the conclusion drawn by the authors of the experiment that there exists an asymptotic limit to product formation as the high speed reactant is burned to completion. Similar behavior is exhibited in Fig. 31(b) in which inferred temperature profiles are shown for the situation in which the low stream reactant is fixed at 1% and the high speed reactant is varied to obtain the same equivalence ratios.

Further assessment of the FMDF approach is made in Fig. 32(a) which shows the variation of the normalized product thickness with the equivalence ratio. In lieu of direct species measurements, product formation in the experimental investigation was inferred from the temperature measurements. While the simulation allows direct measurement of the species mass fractions, the product thickness as defined by Mungal and Dimotakis (1984) was used for consistency:

$$\delta_{p1} = \int_{-\infty}^{+\infty} \frac{C_p \langle T(y) \rangle}{c_{10} \Delta Q} dy,$$

$$\delta_{p2} = \int_{-\infty}^{+\infty} \frac{C_p \langle T(y) \rangle}{c_{20} \Delta Q} dy.$$

The distinction between these two definitions of product thickness lies in the free stream concentration used for normalization purposes (Mungal and Dimotakis, 1984). In the definition of δ_{p1} , the high speed mole fraction c_{01} is used, while the low speed mole fraction c_{02} is used in the normalization of δ_{p2} . Figure 32(a) indicates the simulation captures the proper magnitude of product formation through all ranges of the equivalence ratio. At low

values of ϕ , the amount of product formed varies nearly linearly as the low speed reactant is consumed in reaction with excessive amounts of the high speed reactant. At high values of the equivalence ratio, the product thickness approaches an asymptotic value as reaction progress is inhibited by a lack of the high speed reactant relative to the amount of reactant in the low speed stream. This figure corresponds to the area under the curves in Fig. 31(a). Similarly, Fig. 32(b) shows the variation of the normalized product thickness δ_{p2} with the inverse equivalence ratio. The corresponding temperature profiles are those of Fig. 31(b).

8 Concluding Remarks

The utility of the filtered mass density function (FMDF) and its application to LES of variable density chemically reacting flows is explored and demonstrated. The advantage of FMDF lies in its ability to resolve the correlations of the reactive scalars, density and temperature at the subgrid scale (SGS) level without resorting to closure models. The present formulation is developed for treatment of scalar variables only, thus modeling is required for correlations involving the velocity field (such as the Favre SGS stress and mass flux). This may be overcome by considering the joint velocity-scalar FMDF. In the present form the scalar FMDF methodology is capable of treating complex exothermic reacting flows and is powerful in a sense that it can be added to the existent CFD codes.

The evolution equation for the FMDF is derived. Unclosed terms in this equation are identified and models are used to represent their effects. The FMDF transport equation is solved numerically via a Lagrangian Monte Carlo scheme in which the solutions of the equivalent stochastic differential equations (SDEs) are obtained. These solutions preserve the Itô-Gikhman nature of the SDEs. The consistency of the FMDF approach, the convergence of its Monte Carlo solution and the performance of the closures employed in the FMDF transport equation are assessed by comparison with results obtained by direct numerical simulation (DNS) and by conventional LES procedures in which the first two SGS scalar moments are obtained by a finite difference method (LES-FD). These comparative assessments are conducted by implementations of all three schemes (FMDF, DNS and LES-FD) in temporally developing mixing layer and spatially developing planar jet under both non-reacting and

reacting conditions. In non-reacting flows, the Monte Carlo solution of the FMDF yields results similar to those via LES-FD. The advantage of the FMDF is demonstrated by its use in reacting flows. In the absence of a closure for the subgrid scalar fluctuations, the LES-FD results are significantly different from those based on filtered DNS. The FMDF predictions yield much closer agreement to the DNS. The FMDF methodology is also tested by comparative assessment against the experimental data of Mungal and Dimotakis (1984) for a hydrogen-fluorine reacting mixing layer. It is shown that the FMDF method is able to accurately predict the temperature field. The “flip effect” and other physical phenomenon associated with experimental results are also correctly predicted by FMDF.

The results presented in this work demonstrate that FMDF provides a powerful tool for large eddy simulation of turbulent reacting flows. While the FMDF method is computationally more expensive than conventional LES method, it provides extensive flexibility for treating complex reacting flows over that of conventional LES methods without resorting to ad-hoc assumptions. Additionally, the FMDF approach can be applied to practical combustion systems where DNS is not feasible. Based on these observations, it is anticipated that LES of turbulent reacting flows with realistic chemical kinetics to be routinely conducted for practical applications in the near future.

9 Personnel

Dr. Peyman Givi is the PI of this project. Drs. Dale B. Taulbee and Cyrus K. Madnia are th Co-PIs. One Graduate Research Assistant (RA), Mr. Paul Colucci, is being supported by this Grant.

References

- Aldama, A. A. (1990). Filtering techniques for turbulent flow simulations. volume 49 of *Lecture Notes in Engineering*. Springer-Verlag, New York, NY.
- Bardina, J., Ferziger, J. H., and Reynolds, W. C. (1983). Improved turbulence models based on large eddy simulations of homogeneous, incompressible, turbulent flows. Department of Mechanical Engineering Report TF-19, Stanford University, Stanford, CA.
- Baulch, D. L., Duxbury, J., Grant, S. J., and Montague, D. C. (1981). Evaluated kinetic rate data for high temperature reactions. *J. Phys. Chem. Ref. Data* **4**.
- Billingsly, P. (1979). *Probability and Measure*. John Wiley and Sons, Inc., New York.
- Borghì, R. (1988). Turbulent combustion modeling. *Prog. Energy Combust. Sci.* **14**, 245–292.
- Broadwell, J. E. and Breidenthal, R. E. (1982). A simple model of mixing and chemical reaction in a turbulent shear layer. *J. Fluid Mech.* **125**, 397.
- Brown, G. L. and Roshko, A. (1974). On density effects and large structure in turbulent mixing layers. *J. Fluid Mech.* **64**, 775–816.
- Carpenter, M. H. (1990). A high-order compact numerical algorithm for supersonic flows. In Morton, K. W., editor, *Twelfth International Conference on Numerical Methods in Fluid Dynamics*, volume 371 of *Lecture Notes in Physics*, pages 254–258. Springer-Verlag, New York, NY.
- Chelliah, H. K. (1989), *Asymptotic Analyses of the Structures and Characteristics of Flames*. Ph.D. Thesis, Department of Mechanical and Aerospace Engineering, Princeton University, Princeton, NJ.
- Chen, H., Daugherty, J. D., and Fyfe, W. (1975). Flame propagation and repetitively pulsed Hydrogen Fluoride (HF) chain-reaction laser. *IEEE J. Quantum Electronics* **8**, 648–653.
- Colucci, P. J., Jaberì, F. A., Givi, P., and Pope, S. B. (1997). Filtered density function for large eddy simulation of turbulent reacting flows. *Phys. Fluids*. submitted.
- Colucci, P. J. (1993), Linear stability analysis of density stratified parallel shear flows. M.S. Thesis, Department of Mechanical and Aerospace Engineering, State University of New York at Buffalo, Buffalo, NY.
- Cool, T. A., Stephens, R. R., and Shirley, J. A. (1970). HCl, HF, and DF partially inverted CW chemical lasers. *J. Appl. Phys.* **41**, 4038–4050.
- Dopazo, C. and O'Brien, E. E. (1976). Statistical treatment of non-isothermal chemical reactions in turbulence. *Combust. Sci. and Tech.* **13**, 99–112.

- Eidson, T. M. (1985). Numerical simulation of the turbulent rayleigh-benard problem using subgrid modelling. *J. Fluid Mech.* **158**, 245–268.
- Erlebacher, G., Hussaini, M. Y., Speziale, C. G., and Zang, T. A. (1992). Toward the large eddy simulation of compressible turbulent flows. *J. Fluid Mech.* **238**, 155–185.
- Gardiner, C. W. (1990). *Handbook of Stochastic Methods*. Springer-Verlag, New York, NY.
- Germano, M. (1992). Turbulence: The filtering approach. *J. Fluid Mech.* **238**, 325–336.
- Gikhman, I. I. and Skorokhod, A. V. (1972). *Stochastic Differential Equations*. Springer-Verlag, New York, NY.
- Gillespie, D. T. (1992). *Markov Processes, An Introduction for Physical Scientists*. Academic Press, New York, NY.
- Gmelin. (1980). *Handbook of Inorganic Chemistry: Fluorine Suppl., Vol. 2: The Element*. Springer-Verlag, New York, NY.
- Helfand, E. (1979). Numerical integration of stochastic differential equations. *Bell System Technical Journal* **58**, 2289 – 2299.
- Itô, K. (1951). On stochastic differential equations. *Memoirs. Amer. Math. Soc.* **4**.
- Karlin, S. and Taylor, H. M. (1981). *A Second Course in Stochastic Processes*. Academic Press, New York, NY.
- Kerr, R. M., Domaradzki, J. A., and Barbier, G. (1996). Small-scale properties of nonlinear interactions and subgrid-scale energy transfer in isotropic turbulence. *Phys. Fluids* **8**, 197–208.
- Kloeden, P. E. and Platen, E. (1995). *Numerical Solution of Stochastic Differential Equations*, volume 23 of *Applications of Mathematics, Stochastic Modelling and Applied Probability*. Springer-Verlag, New York, NY.
- Konrad, J. H. (1977), *An Experimental Investigation of Mixing in Two-Dimensional Turbulent Shear Flows with Application to Diffusion-Limited Chemical Reactions*. PhD thesis, California Institute of Technology, Pasadena, CA.
- Leonard, A. D. and Dai, F. (1994). Applications of a coupled monte carlo PDF/finite volume CFD method for turbulent combustion. AIAA Paper 94-2904.
- Libby, P. A. and Williams, F. A., editors. (1980). *Turbulent Reacting Flows*, volume 44 of *Topics in Applied Physics*. Springer-Verlag, Heidelberg.
- Lundgren, T. S. (1969). Model equation for nonhomogeneous turbulence. *Phys. Fluids* **12**, 485–497.

- MacCormack, R. W. (1969). The effect of viscosity in hypervelocity impact catering. AIAA Paper 69-354.
- Michalke, A. (1965). On spatially growing disturbances in an inviscid shear layer. *J. Fluid Mech.* **23**, 521-544.
- Miller, R. S., Madnia, C. K., and Givi, P. (1994). Structure of a turbulent reacting mixing layer. *Combust. Sci. and Tech.* **99**, 1-36.
- Moser, R. D. and Rogers, M. M. (1991). Mixing transition and the cascade of small scales in a plane mixing layer. *Phys. Fluids A* **3**, 1128-1134.
- Mungal, M. G. and Dimotakis, P. E. (1984). Mixing and combustion with low heat release in a turbulent mixing layer. *J. Fluid Mech.* **148**, 349-382.
- O'Brien, E. E. (1980). The probability density function (PDF) approach to reacting turbulent flows. In Libby and Williams (1980), chapter 5, pages 185-218.
- Papamoschou, D. and Roshko, A. (1986). Observations of supersonic free shear layers. AIAA Paper 86-0162.
- Poinsot, T. J. and Lele, S. K. (1992). Boundary conditions for direct simulations of compressible viscous flows. *J. Comp. Phys.* **101**, 104-129.
- Pope, S. B. (1976). The probability approach to modeling of turbulent reacting flows. *Combust. Flame* **27**, 299-312.
- Pope, S. B. (1985). PDF methods for turbulent reactive flows. *Prog. Energy Combust. Sci.* **11**, 119-192.
- Pope, S. B. (1991). Mapping closures for turbulent mixing and reaction. *Theoret. Comput. Fluid Dynamics* **2**, 255-270.
- Pope, S. B. (1994). Lagrangian pdf methods for turbulent flows. *Ann. Rev. Fluid Mech.* **26**, 23-63.
- Rapp, D. and Johnston, H. S. (1960). Nitric Oxide-Fluorine dilute diffusion flame. *J. Chem. Phys.* **33**, 695-699.
- Riley, J. J., Metcalfe, R. W., and Orszag, S. A. (1986). Direct numerical simulations of chemically reacting mixing layers. *Phys. Fluids* **29**, 406-422.
- Risken, H. (1989). *The Fokker-Planck Equation, Methods of Solution and Applications*. Springer-Verlag, New York, NY.
- Rudy, D. H. and Strikwerda, J. C. (1980). Boundary conditions for subsonic compressible navier-stokes calculations. *J. Comp. Phys.* **36**, 327-338.
- Salvetti, M. V. and Banerjee, S. (1995). A priori tests of a new dynamic subgrid-scale model for finite-difference large-eddy simulations. *Phys. Fluids* **7**, 2831-2847.

- Sandham, N. D. and Reynolds, W. C. (1989). Some inlet-plane effects on the numerically simulated spatially-developing mixing layer. In *Turbulent Shear Flows 6*, pages 441–454. Springer-Verlag, New York, NY.
- Spalding, D. B. and Stephenson, P. L. (1971). Laminar flame propagation in Hydrogen+Bromine mixtures. *Proc. R. Soc. Lond.* **324**, 315.
- Steinberger, C. J., Vidoni, T. J., and Givi, P. (1993). The compositional structure and the effects of exothermicity in a nonpremixed planar jet flame. *Combust. Flame* **94**, 217–232.
- Vreman, B., Geurts, B., and Kuerten, H. (1994). Realizability conditions for the turbulent stress tensor in large-eddy simulation. *J. Fluid Mech.* **278**, 351–362.
- Wallace, A. K. (1981), *Experimental Investigation on the Effects of Chemical Heat Release on Shear Layer Growth and Entrainment*. PhD thesis, University of Adelaide, Australia.
- Williams, F. A. (1985). *Combustion Theory*. The Benjamin/Cummings Publishing Company, Menlo Park, CA, 2nd edition.
- Zang, T. A. and Piomelli, U. (1993). Large eddy simulation of transitional flow. In Galperin, B. and Orszag, S. A., editors, *Large Eddy Simulations of Complex Engineering and Geophysical Flows*, chapter 11, pages 209–227. Cambridge University Press, Cambridge, UK.

Figure captions

Figure 1. Cross-stream variation of the filtered density in temporally evolving mixing layer obtained by FMDF-1 at (a) $t = 0$, (b) $t = 44$.

Figure 2. Vorticity thickness vs. time in the temporally evolving mixing layer.

Figure 3. Contours of the filtered vorticity and temperature in the temporal mixing layer obtained by FMDF-1 (right hand side) and FMDF-2 (left hand side) at $t = 44$. The plots at the top represent the vorticity field and the bottom plots show the temperature field.

Figure 4. Cross-stream variation of the mean filtered (a) pressure, (b) kinetic energy, (c) temperature, and (d) scalar at $t = 44$.

Figure 5. Cross-stream variation of the percentage of the difference in pressure as obtained by FMDF-2 and FMDF-1 with different smoothing in temporally evolving shear layer at $t = 44$. (I) Long-dashed line: no smoothing, $NPG = 50$ and $\Delta_E = \Delta$; (I) Dotted-dashed line: smoothed with Gaussian filter, $NPG = 50$ and $\Delta_E = \Delta$; (I) solid line: smoothed with box filter, $NPG = 50$ and $\Delta_E = \Delta$; (I) dashed line: smoothed with local least square filter, $NPG = 50$ and $\Delta_E = \Delta$; (I) Long-dashed thick line: smoothed with Gaussian filter, $NPG = 200$ and $\Delta_E = \Delta$; (I) Dotted thick line: smoothed with Gaussian filter, $NPG = 50$ and $\Delta_E = 2\Delta$.

Figure 6. Contours of the filtered values of the conserved scalar as obtained by (a) LES-FD, (b) FMDF at $t = 44$.

Figure 7. Cross-stream variation of (a) filtered scalar, (b) generalized scalar variance in temporal shear layer at $t = 44$.

Figure 8. Product thickness variation with time in the temporally evolving mixing layer.

Figure 9. Cross-stream variation of the mean filtered density in 3D temporal shear layer at several spanwise locations.

Figure 10. Scatter plots of filtered values of (a) the temperature, (b) the conserved scalar as obtained by M.C. and F.D. with FMDF-2 method in 3D temporal shear layer with 2D forcing.

Figure 11. Cross-stream variation of the mean filtered (a) vorticity, and (b) pressure in 3D temporal shear layer at several spanwise locations.

Figure 12. Scatter plots of filtered quantities as obtained by M.C. and F.D. in the 3D temporal shear layer with 3D forcing: (a) temperature obtained by FMDF-2, (b) conserved scalar obtained by FMDF-1.

Figure 13. (a) Product thickness variation with time, (b) Cross-stream variation of the product mass fraction, in the temporally evolving mixing layer.

Figure 14. Cross-stream variation of the filtered temperature in temporally evolving mixing layer at $t = 44$.

Figure 15. Vorticity thickness vs. time in the temporally evolving mixing layer.

Figure 16. Contours of the filtered pressure in planar jet for different cases, (a) calculated by FMDF-1 with no smoothing of the filtered temperature, (b) calculated by FMDF-1 with smoothed filtered temperature with box filter, (c) calculated by FMDF-2 with no smoothing of the filtered temperature.

Figure 17. Contours of the filtered temperature in planar jet for different cases, (a) calculated by FMDF-1 with no smoothing of the filtered temperature, (b) calculated by FMDF-1 with smoothed filtered temperature with box filter, (c) calculated by FMDF-2 with no smoothing of the filtered temperature.

Figure 18. Contours of (a) particle number density and (b) fluid filtered density in planar jet for the case with uniform weights.

Figure 19. Contours of (a) particle number density, (b) particle weighting and (c) fluid filtered density in planar jet for the case with variable weights.

Figure 20. Temporal evolution of the product thickness, (b) Cross-stream variation of the product distribution at $x/D = 14$, in the spatially evolving reactive planar.

Figure 21. Contours of the instantaneous subgrid scale unmixedness for the spatially evolving planar jet, (a) DNS and (b) FMDF.

Figure 22. Product thickness variation with time in the 3D temporally evolving mixing layer. (a) low LES resolution, (b) high LES resolution.

Figure 23. Cross-stream variation of the mean product mass fraction. (a) the mean values are obtained by averaging over streamwise and spanwise directions, (b) the mean values are obtained by averaging over streamwise direction and are plotted at two different spanwise locations.

Figure 24. Temporal evolution of the vorticity thickness. The upper curves correspond to the cases with high LES resolution and the lower curves correspond to the cases with low LES resolution.

Figure 25. Contour plots of (a) instantaneous Favre filtered temperature and (b) time averaged temperature fields for $\phi = 1$.

Figure 26. Scatter plot of particle temperature versus mixture fraction for $\phi = 1$.

Figure 27. Time history of instantaneous Favre filtered temperature at several cross stream locations.

Figure 28. Cross stream variation of the normalized mean temperature for $\phi = 1$.

Figure 29. Cross stream variation of the normalized mean temperature for $\phi = 8$ and $\phi = \frac{1}{8}$.

Figure 30. Cross stream variation of (a) absolute mean temperature and (b) normalized mean temperature for all equivalence ratios.

Figure 31. Cross stream variation of the 'inferred' mean temperature profiles for (a) 1% high speed mole fraction and (b) 1% low speed mole fraction for all equivalence ratios.

Figure 32. Normalized product thickness variation with equivalence ratio: (a) δ_{p1} versus equivalence ratio and (b) δ_{p2} versus inverse equivalence ratio.

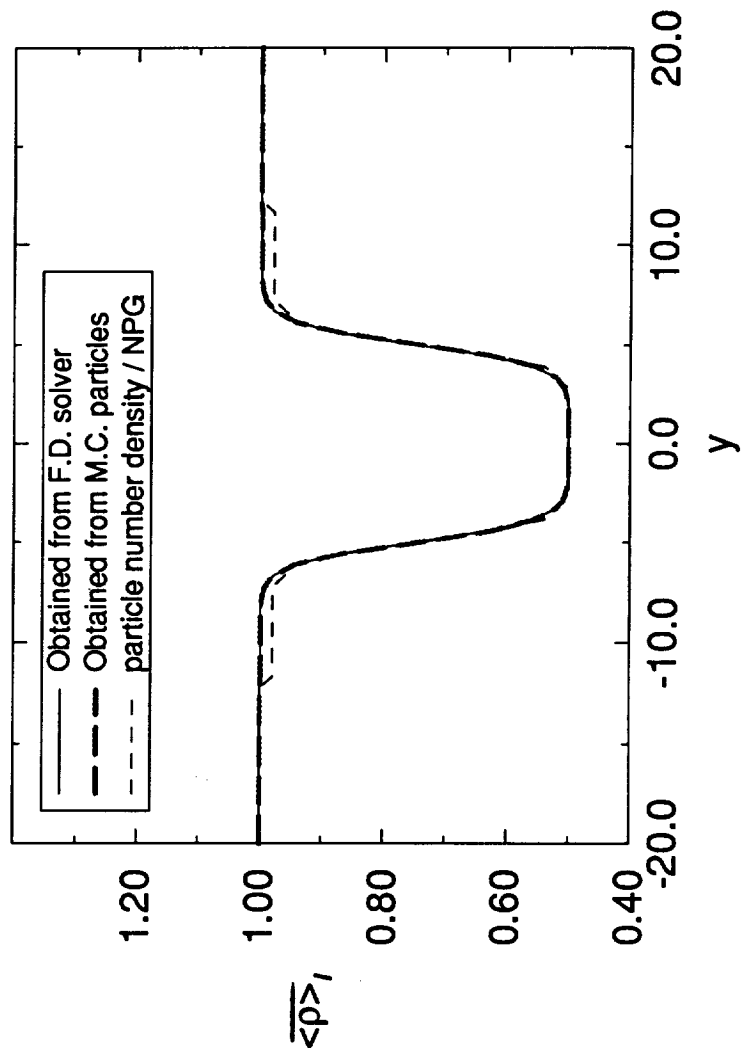


Figure 1(α)

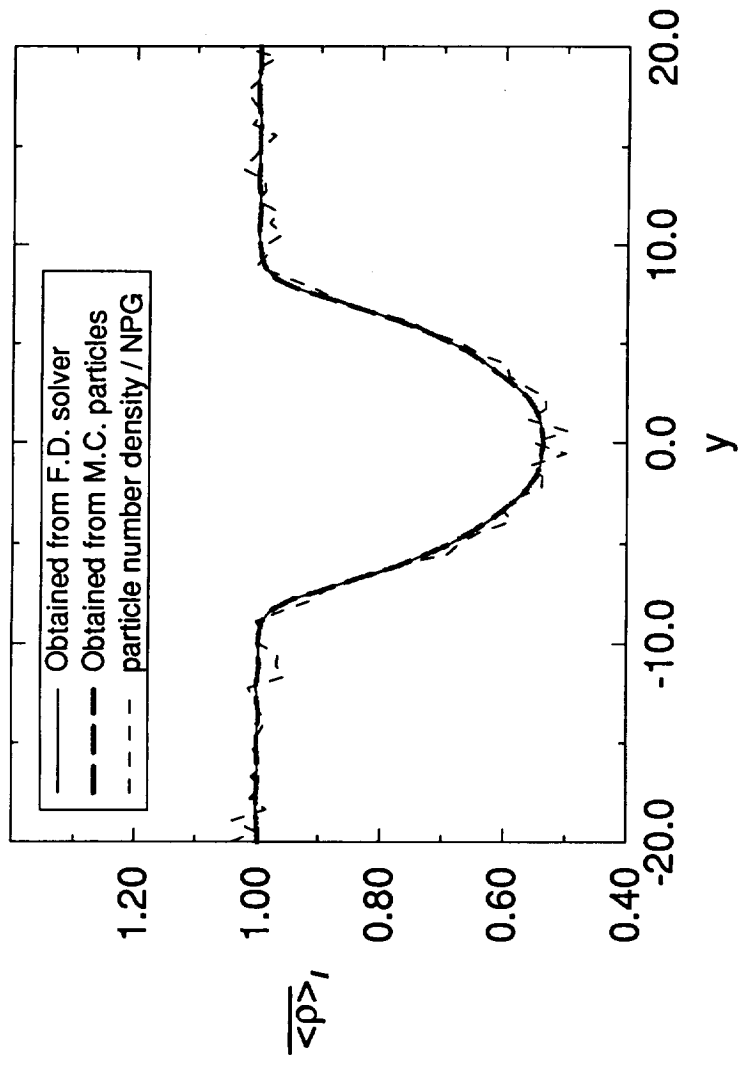


Figure 1(b)

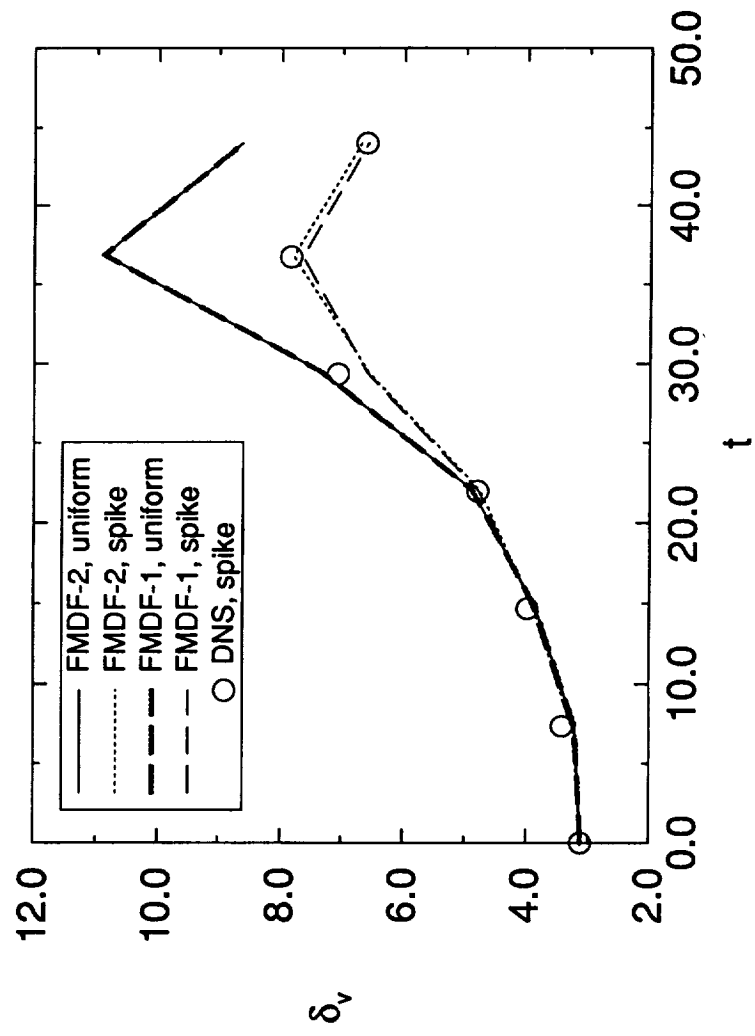
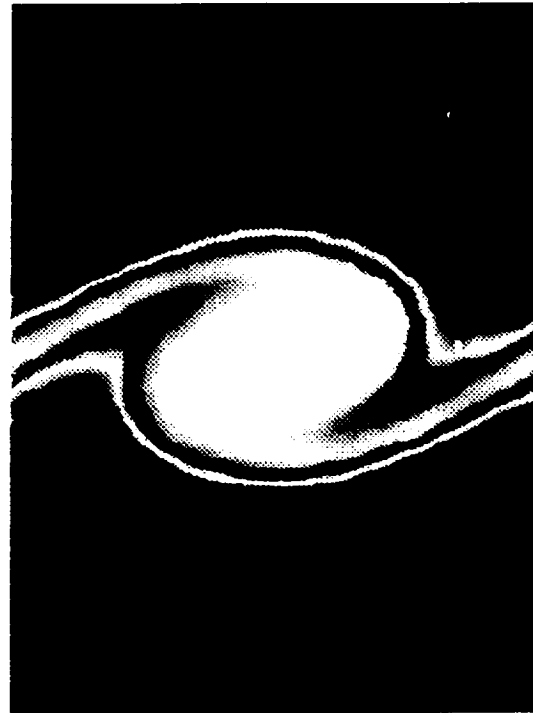
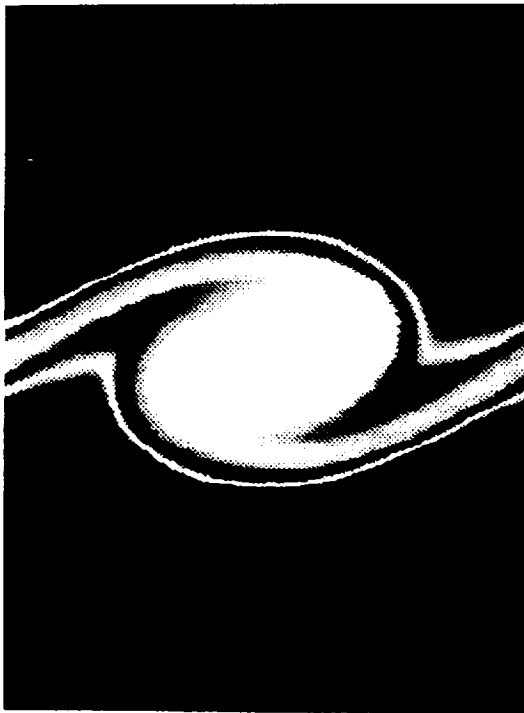


Figure 2



vorticity

-0.80 -0.33 0.14



temperature

1.00 1.50 2.00

Figure 3

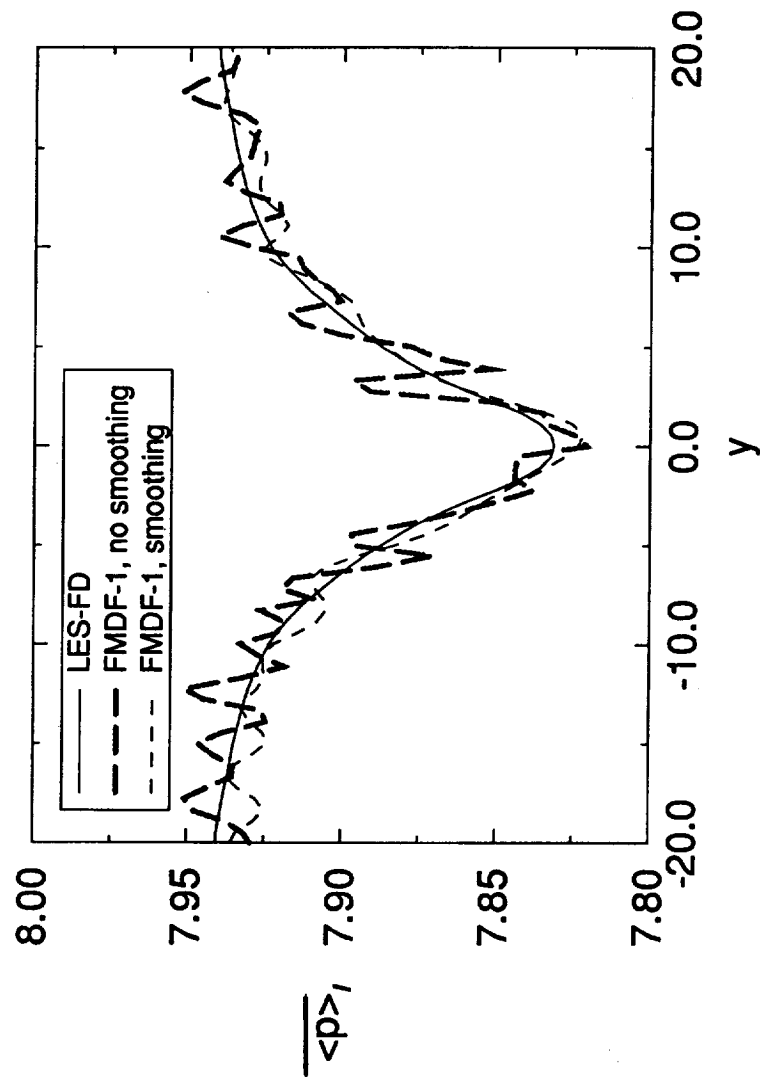


Figure 4(a)

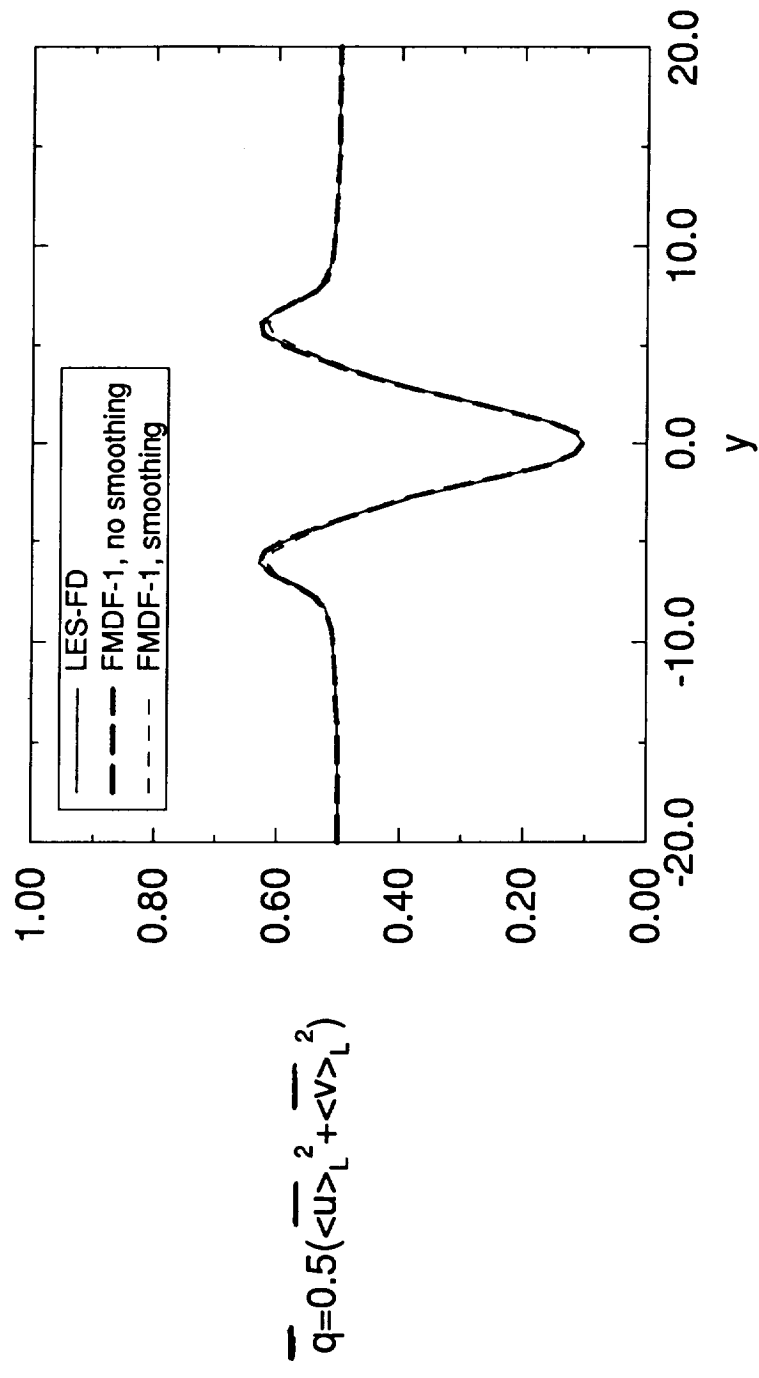


Figure 4(b)

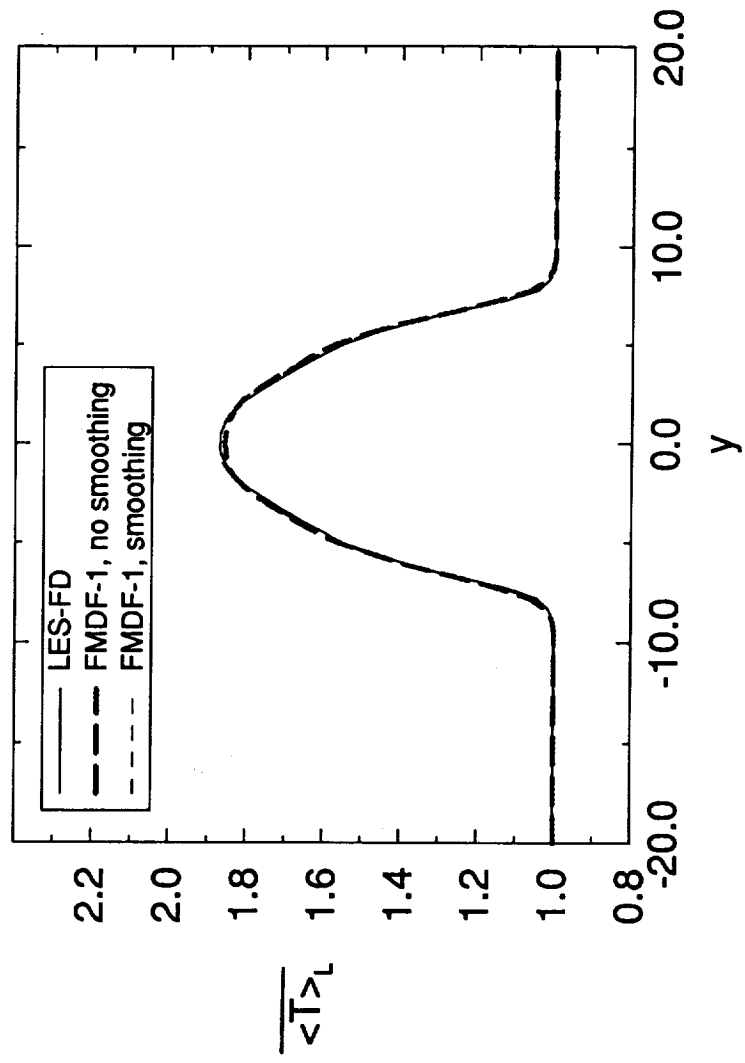


Figure 4(c)

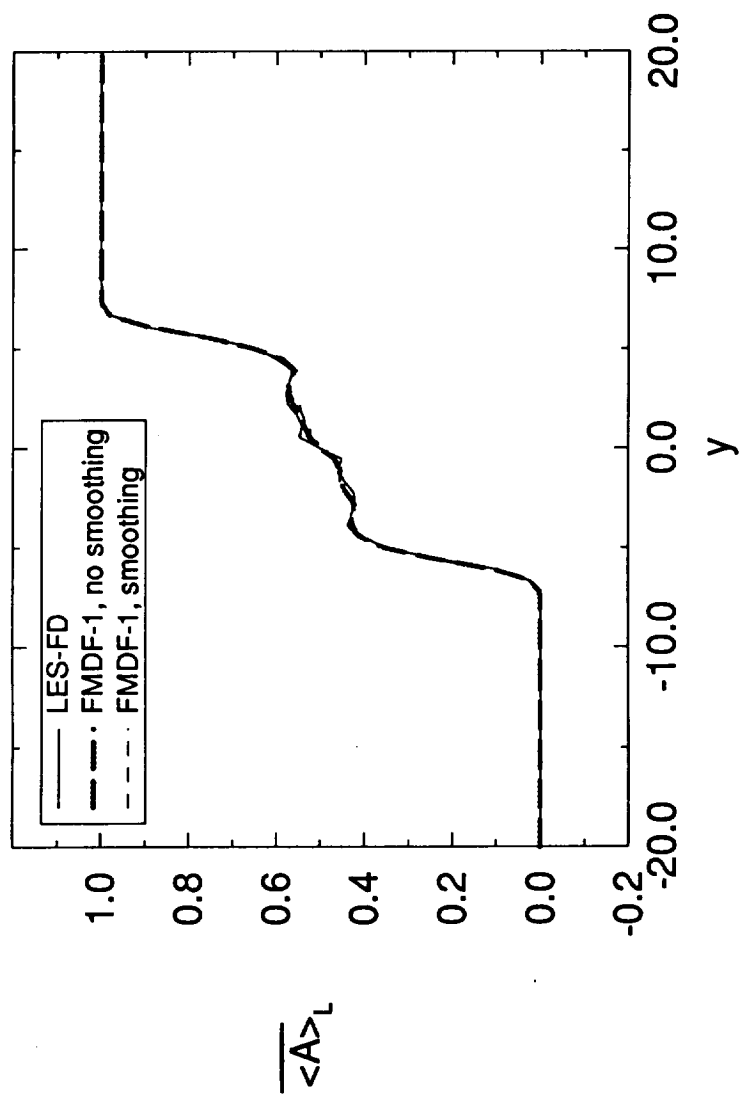


Figure 4(d)

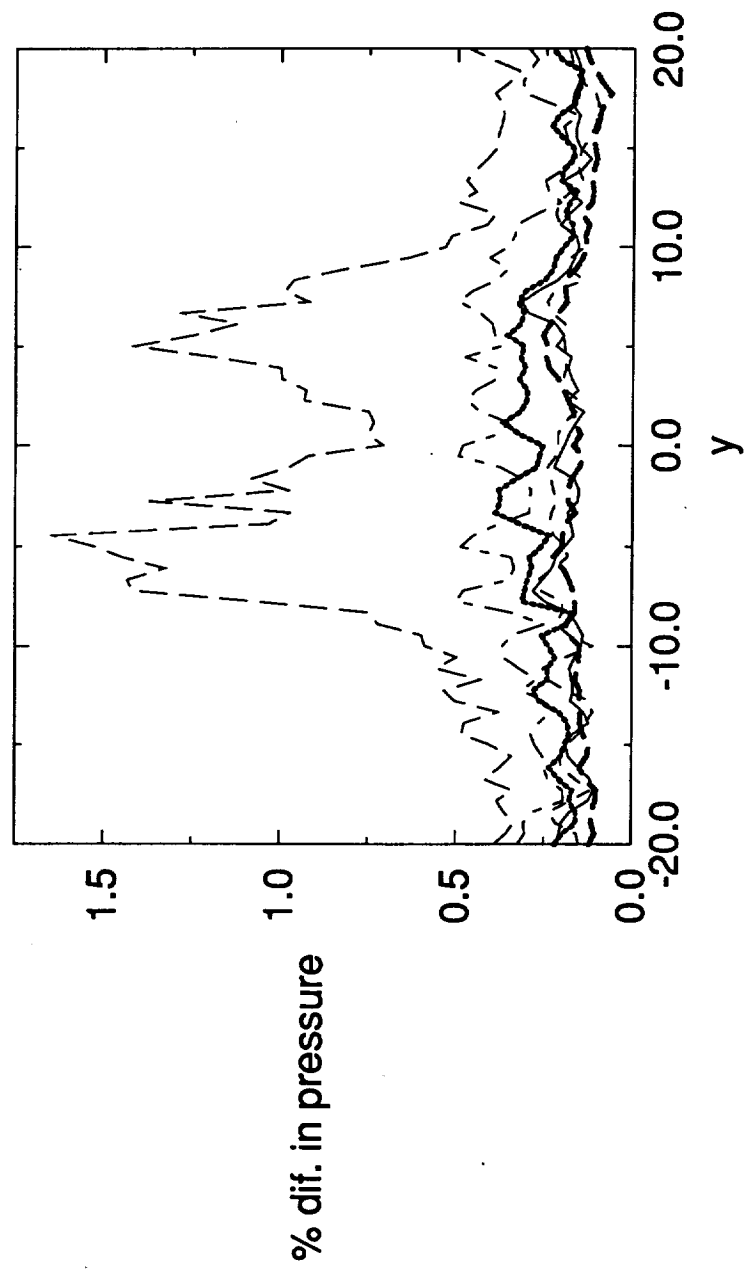


Figure 5



LES-FD



0.0

0.5

1.0



FMDF

Fig 6

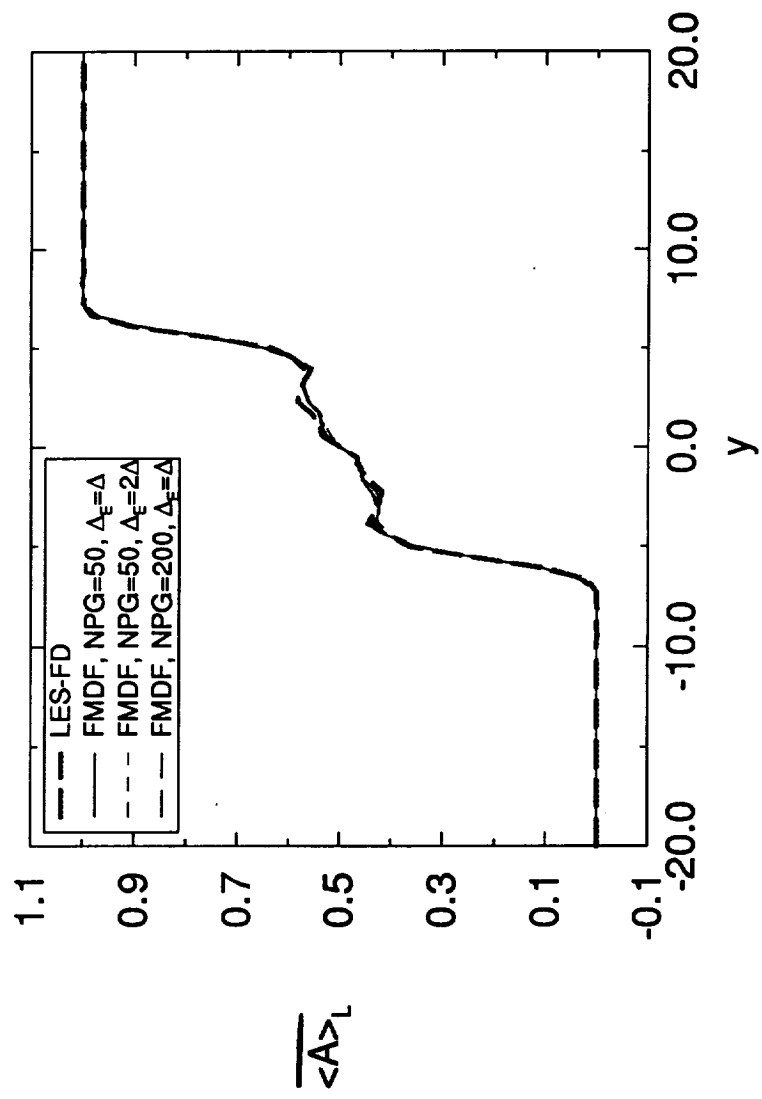


Figure 7(a)

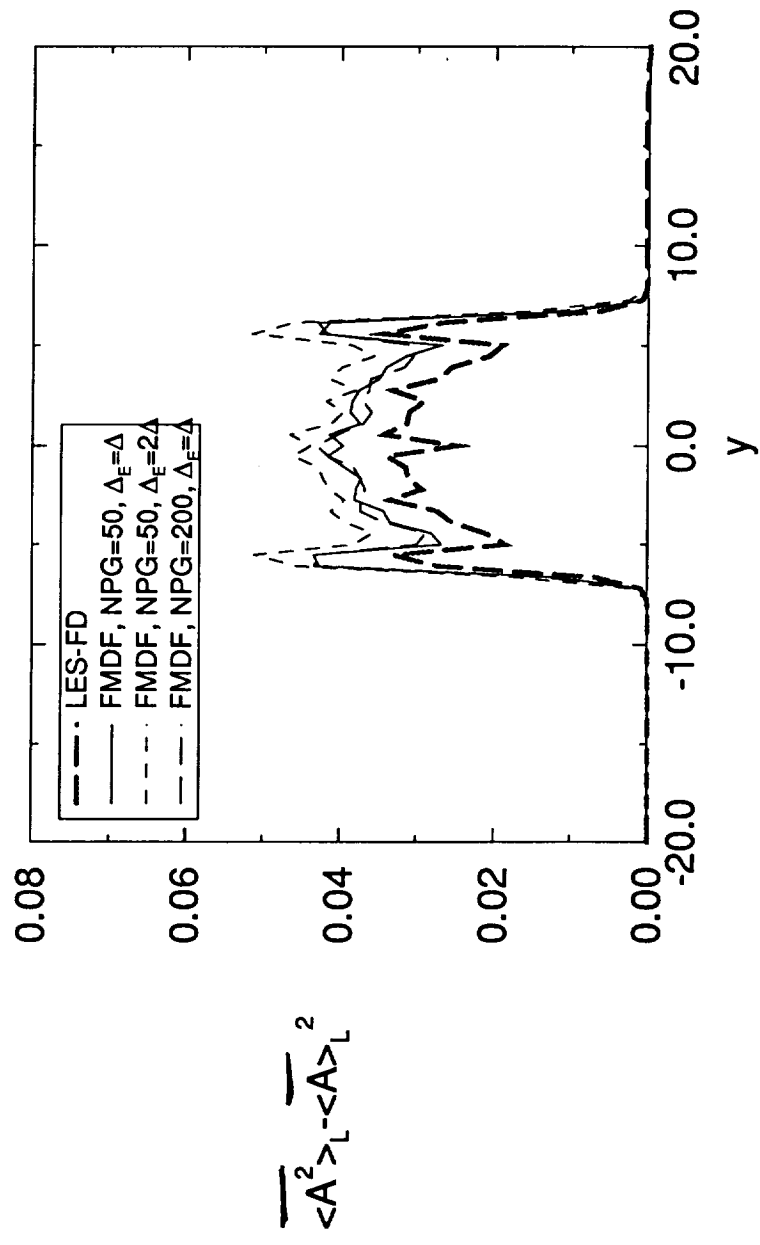


Figure 7(b)

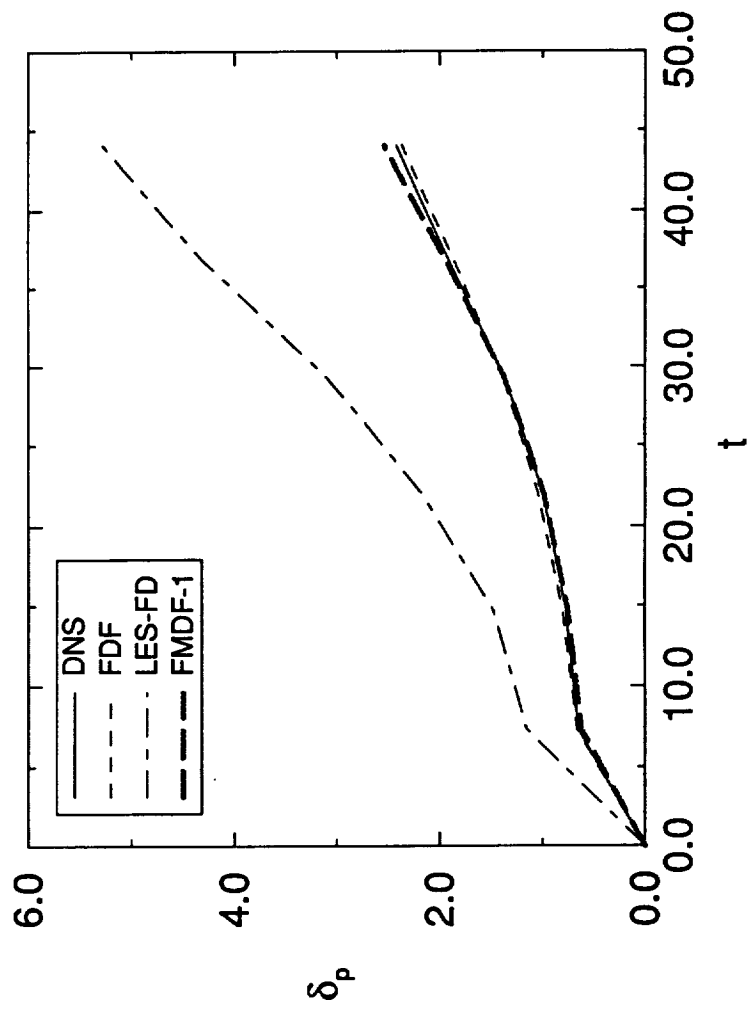


Figure 8

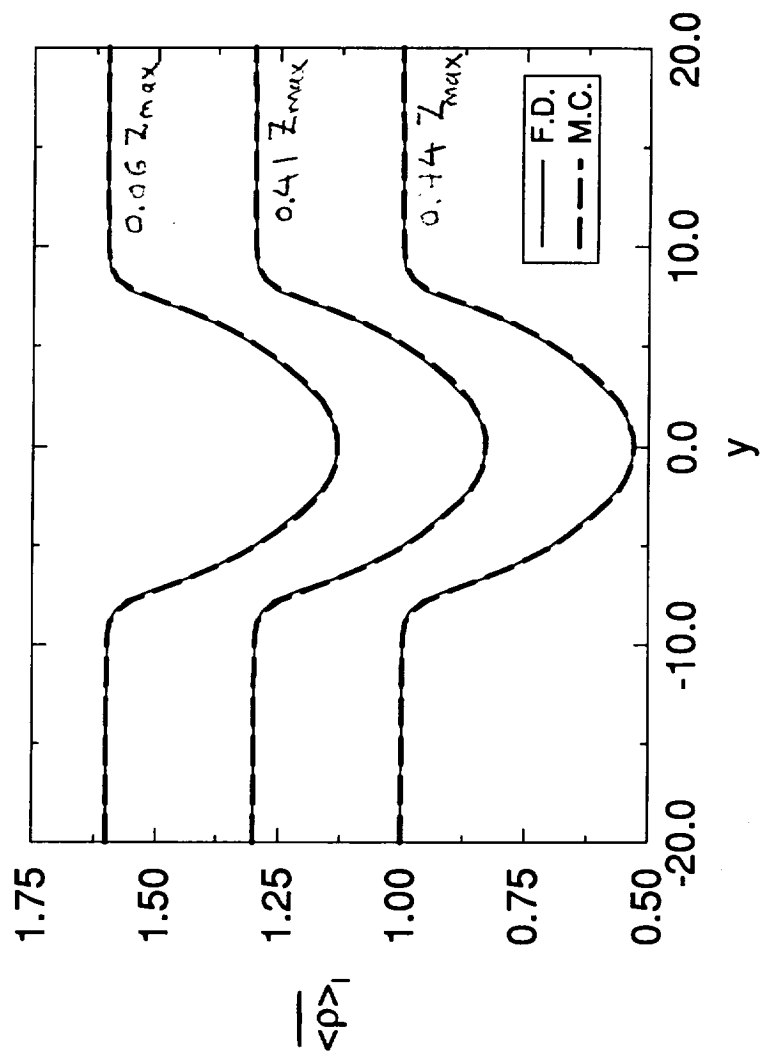


Figure 9

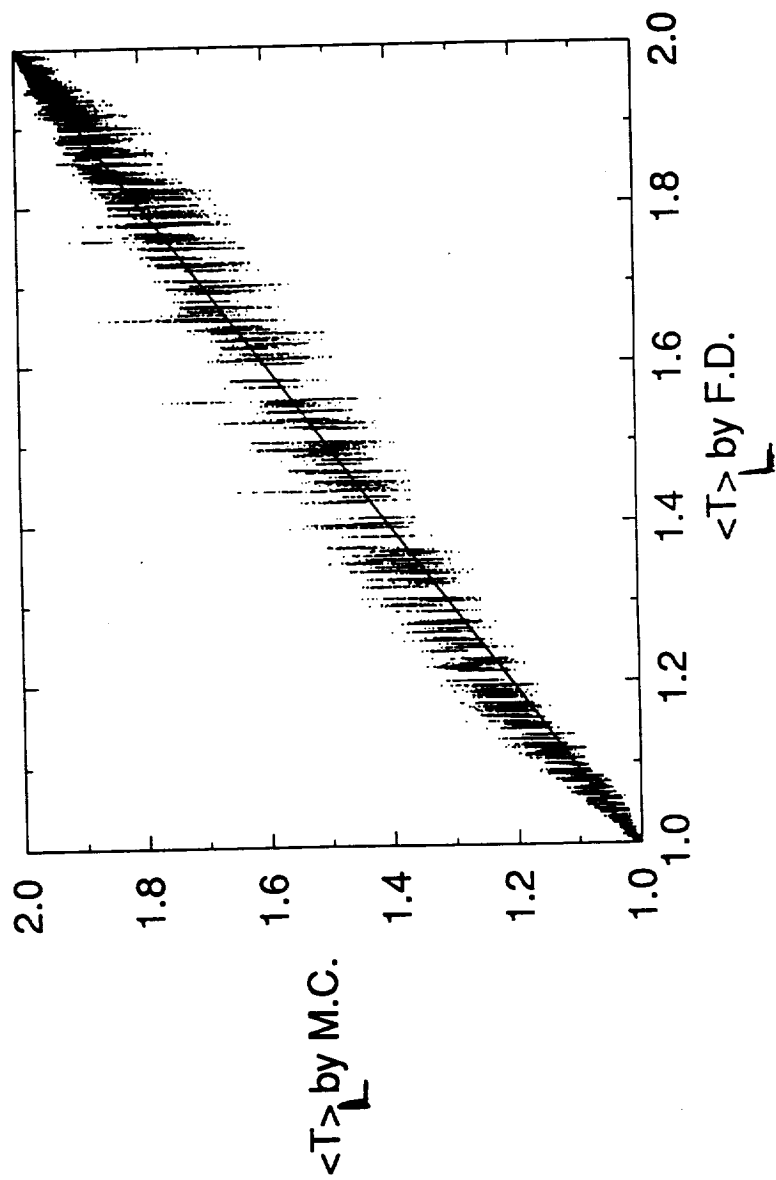


Figure 10(a)

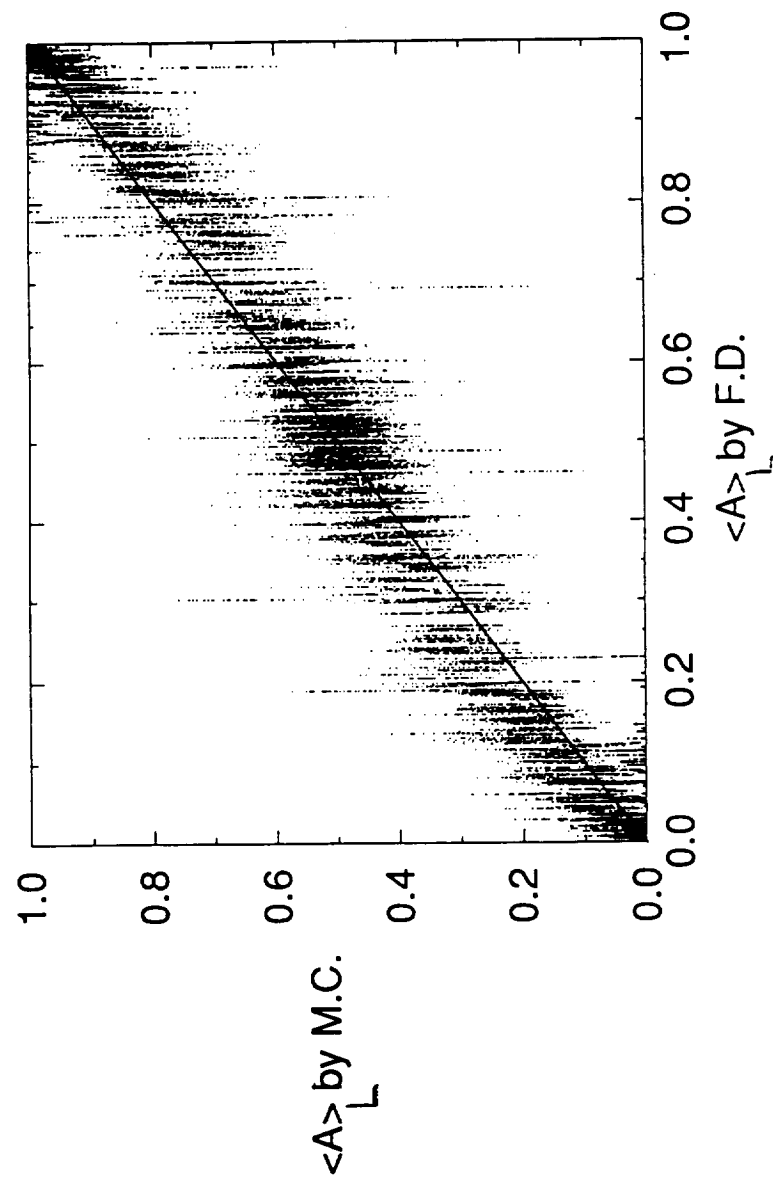


Figure 10(b)

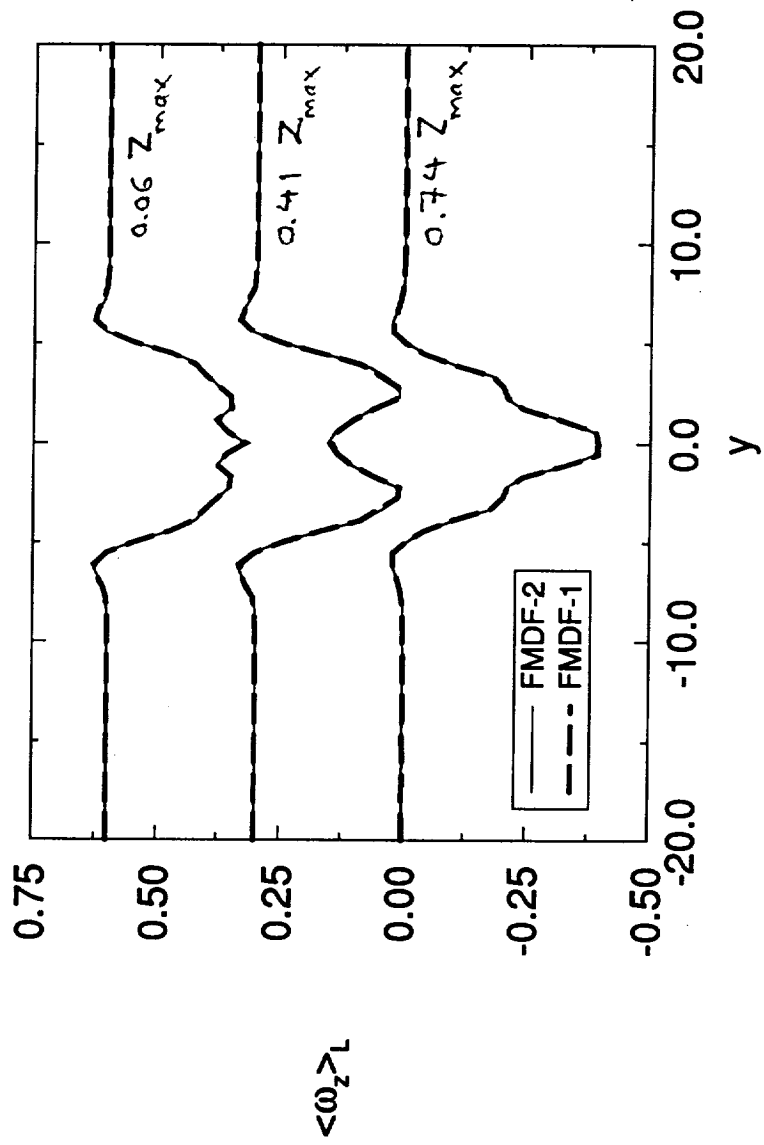


Figure 11(a)

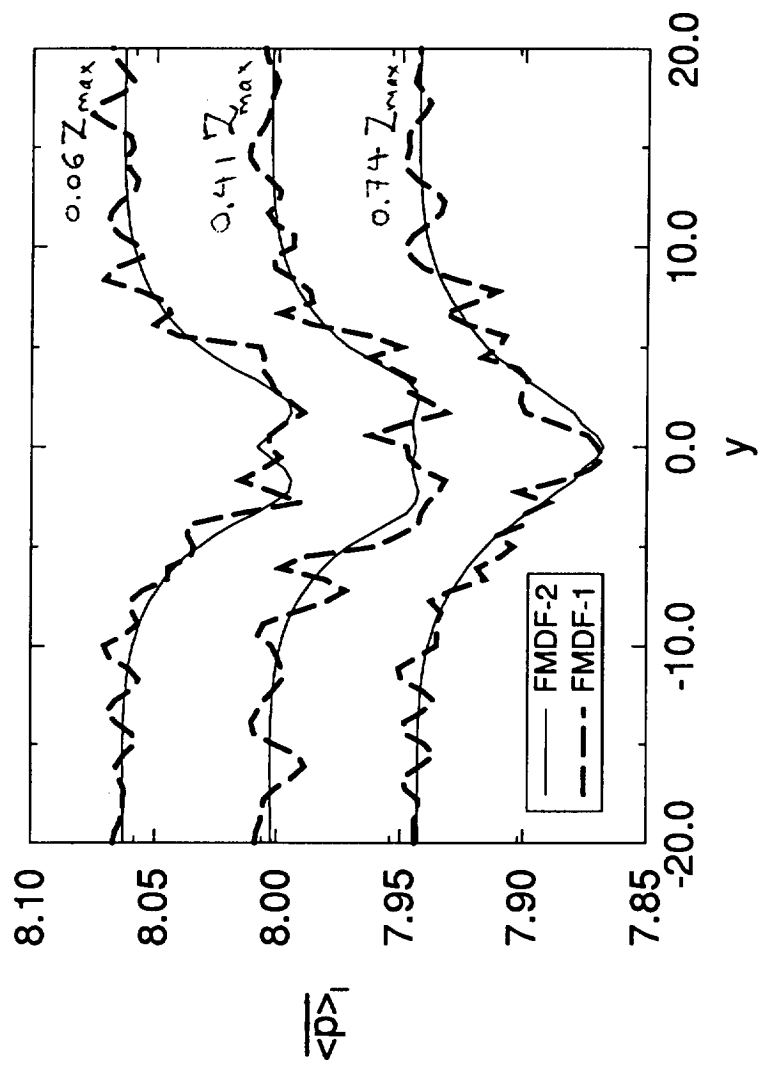


Figure 11(b)

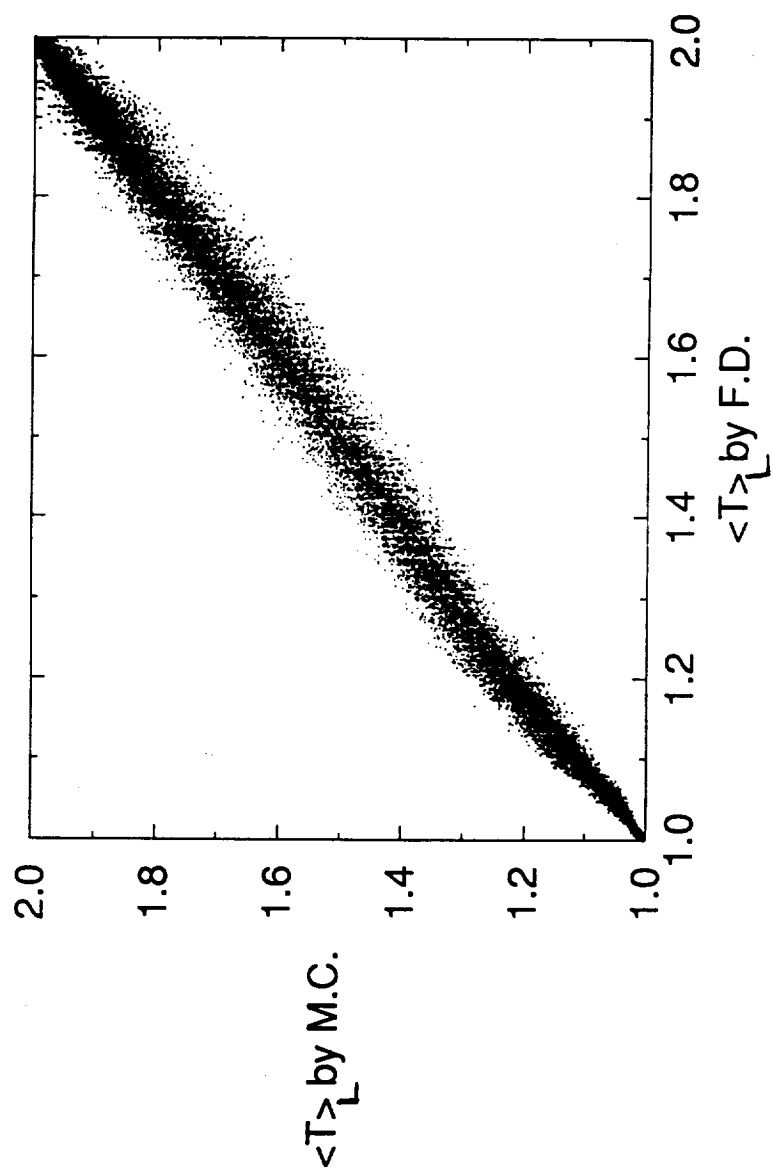


Figure 12(a)

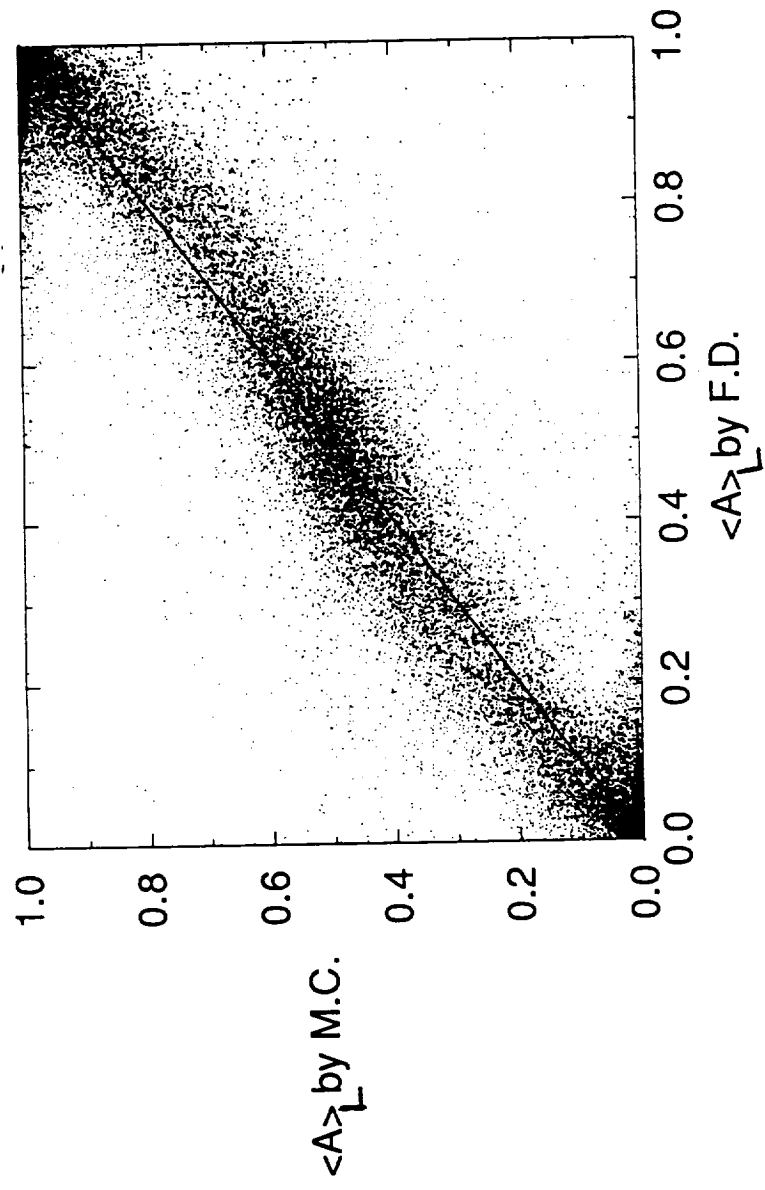


Figure 12(b)

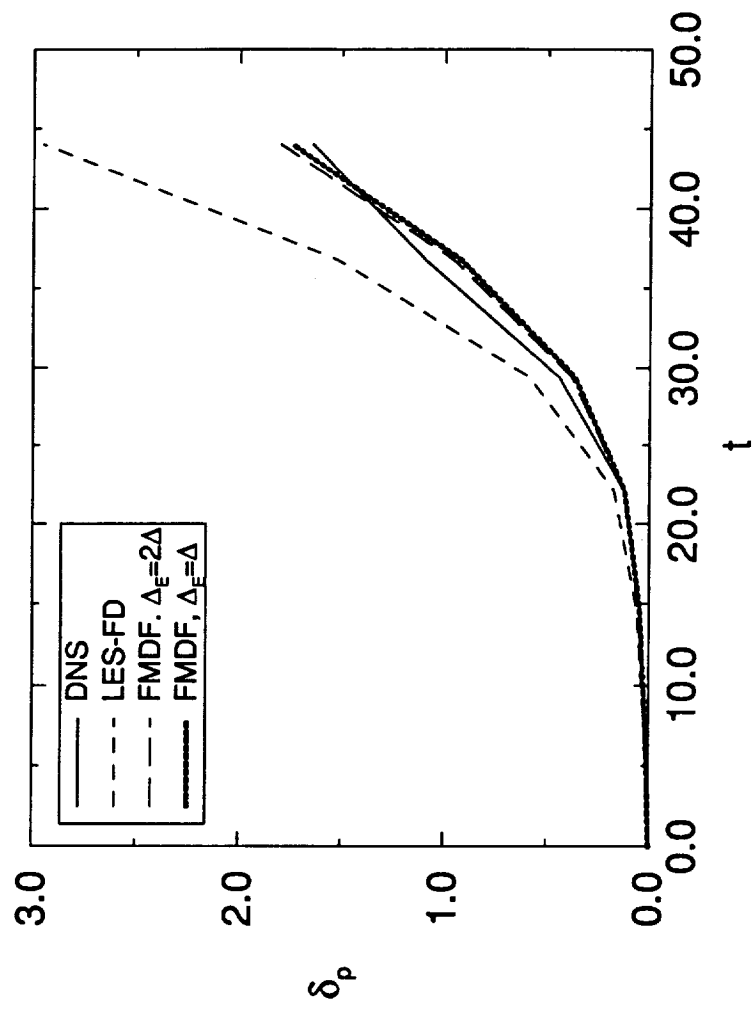


Figure 13(a)

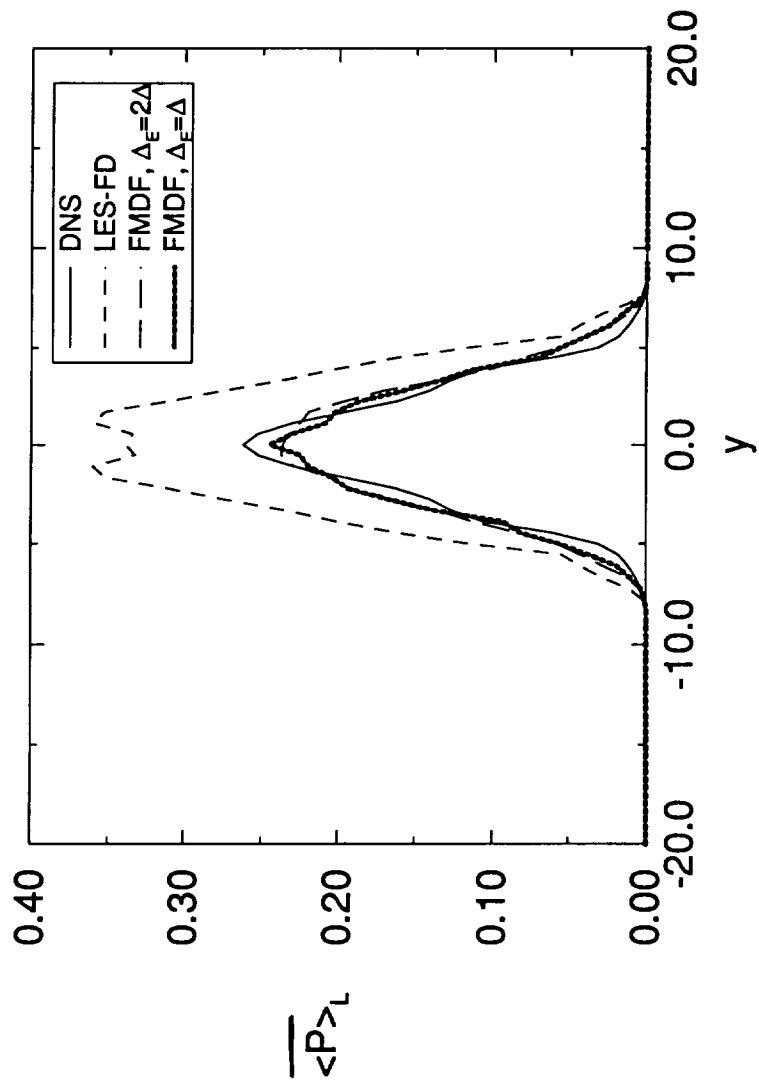


Figure 13 (b)

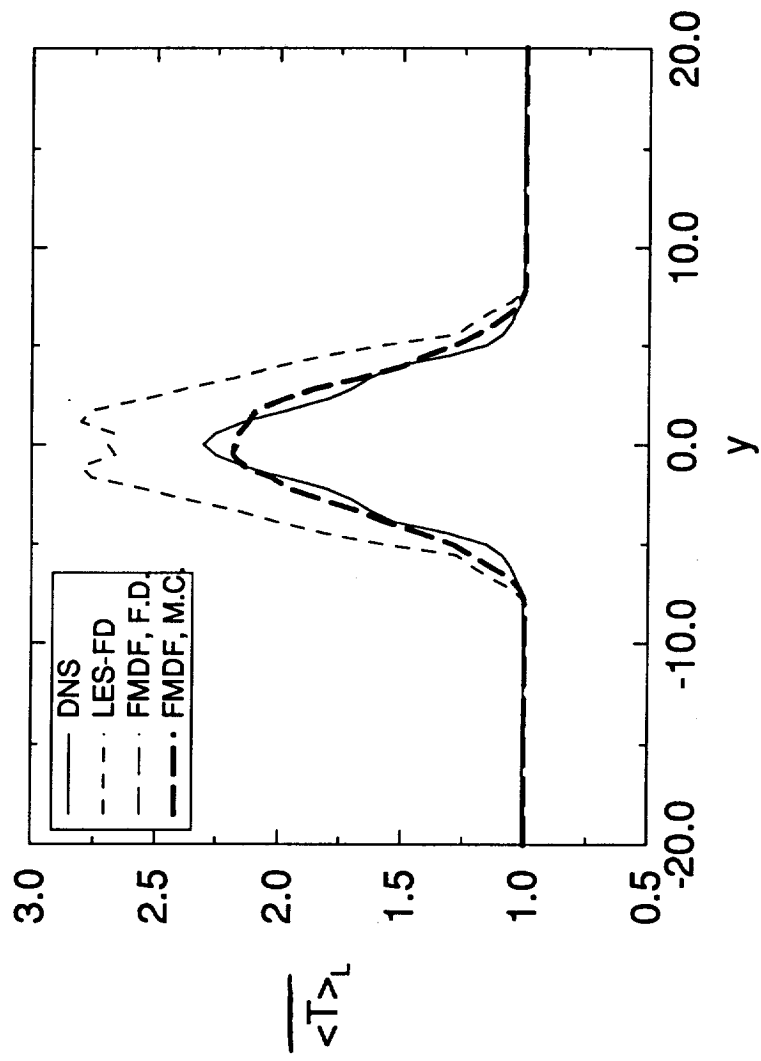


Figure 14

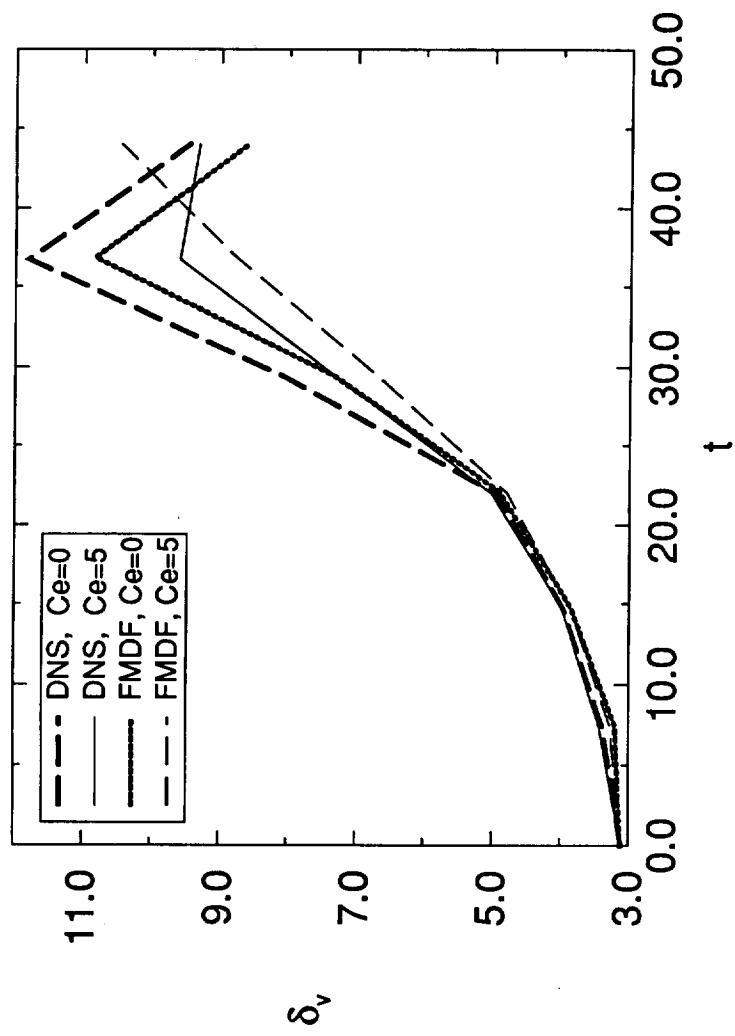


Figure 15

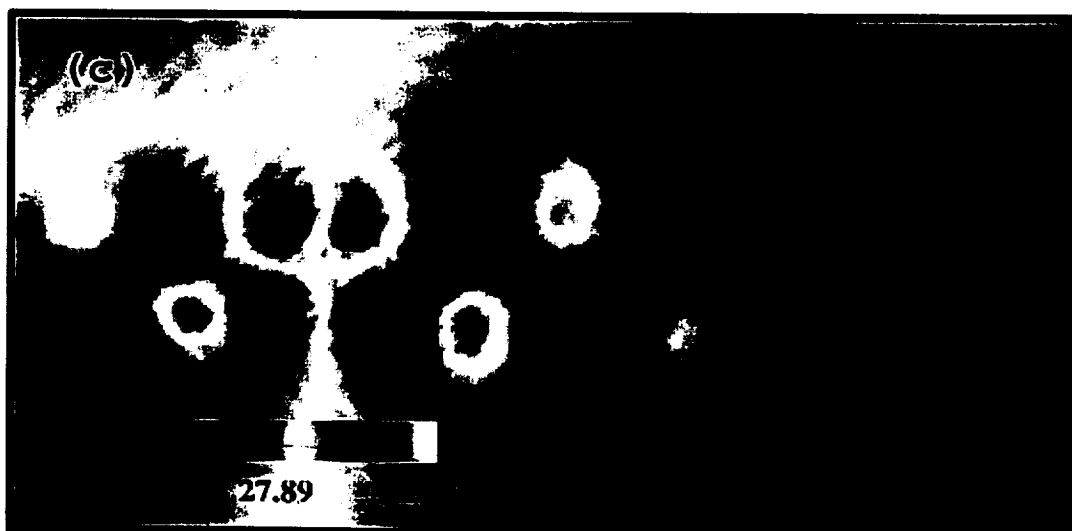
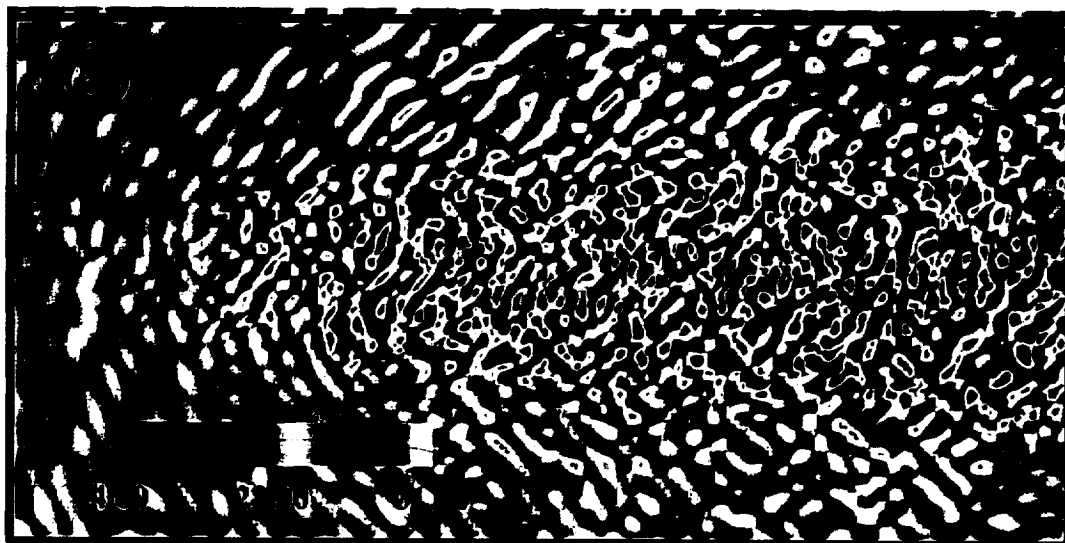


Figure 16

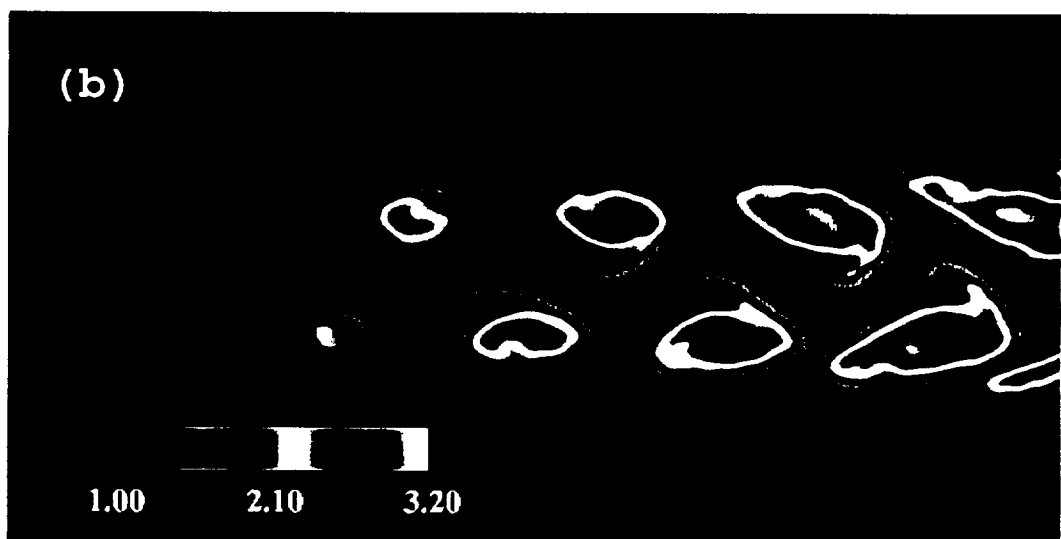
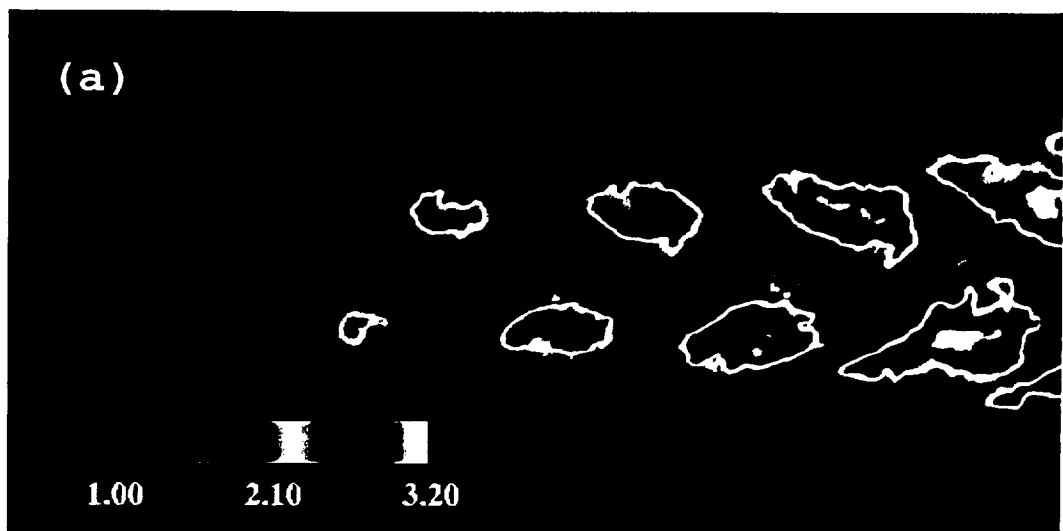


Figure 17

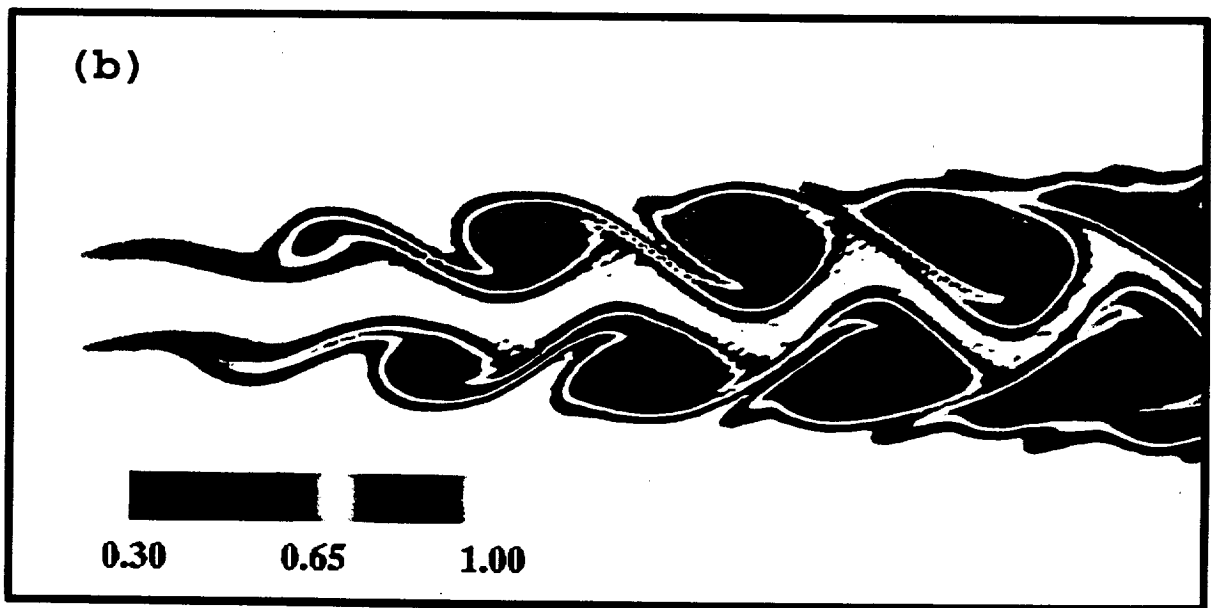
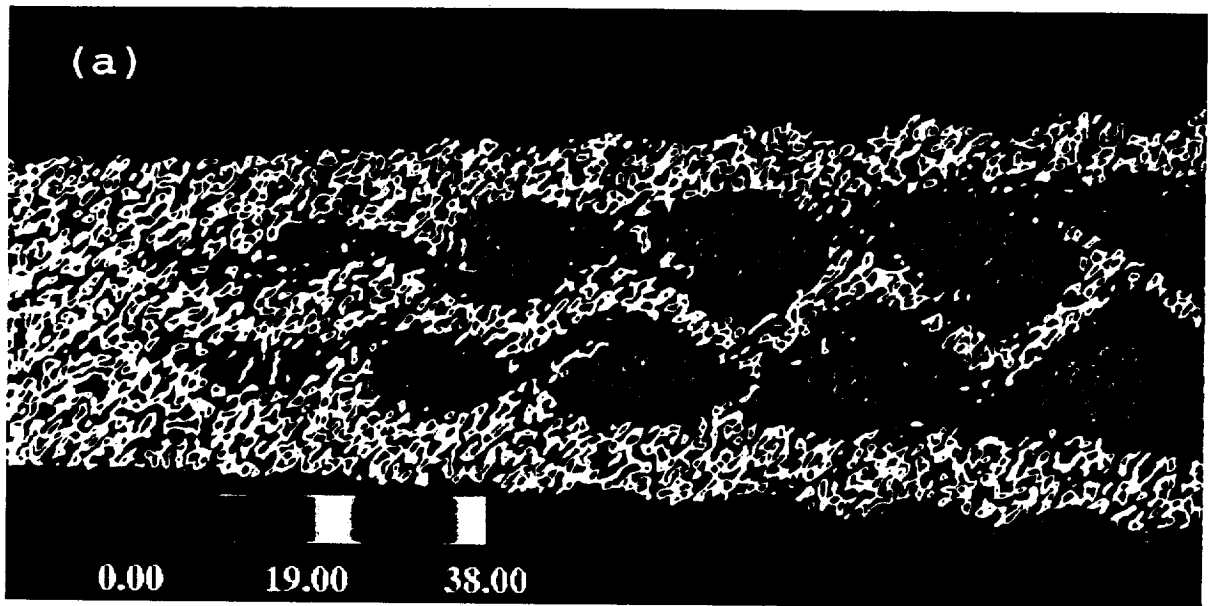


Figure 18

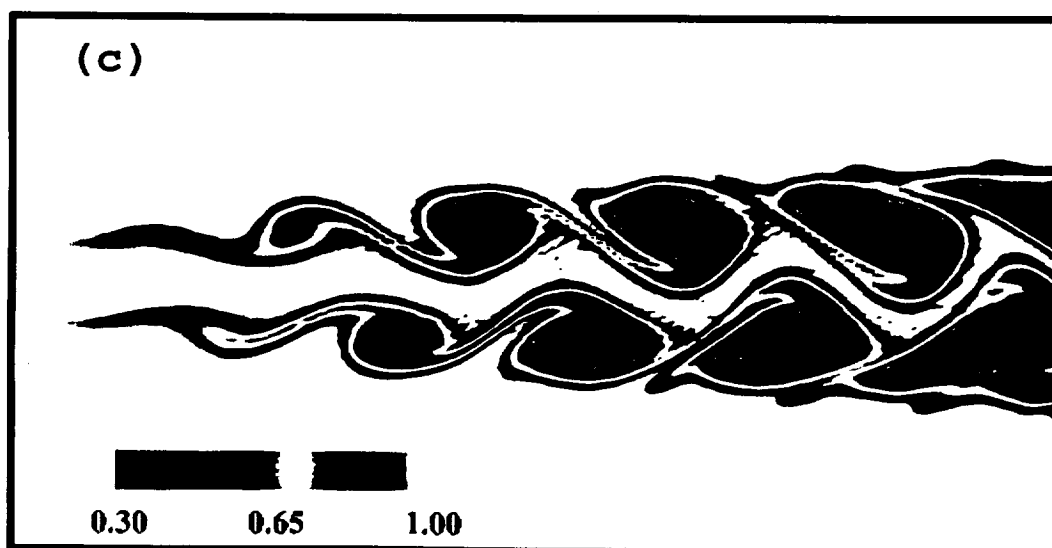
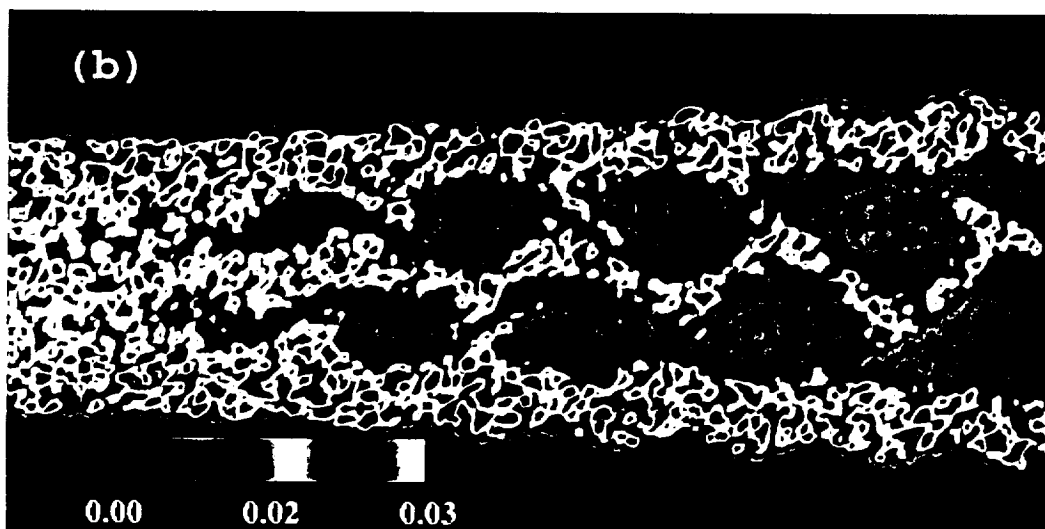
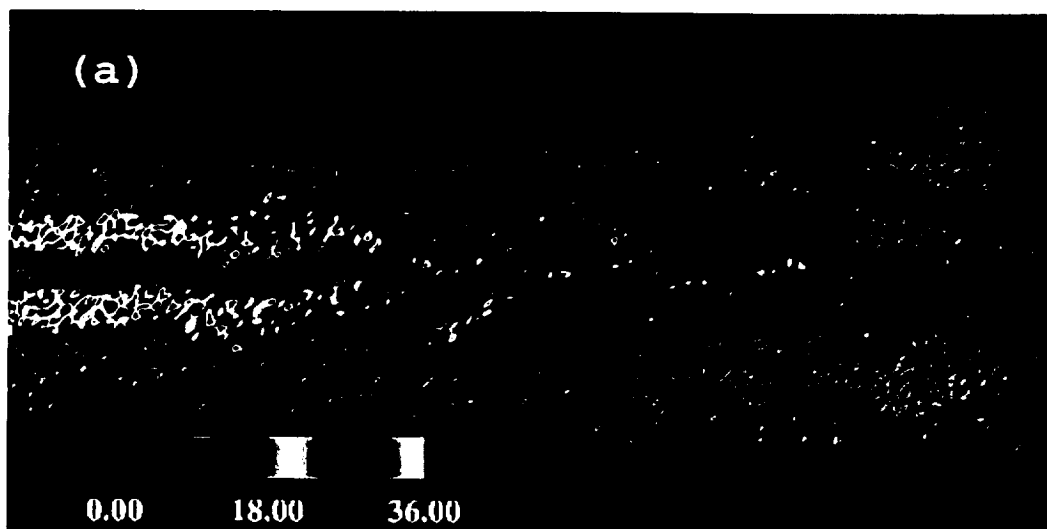


Figure 19

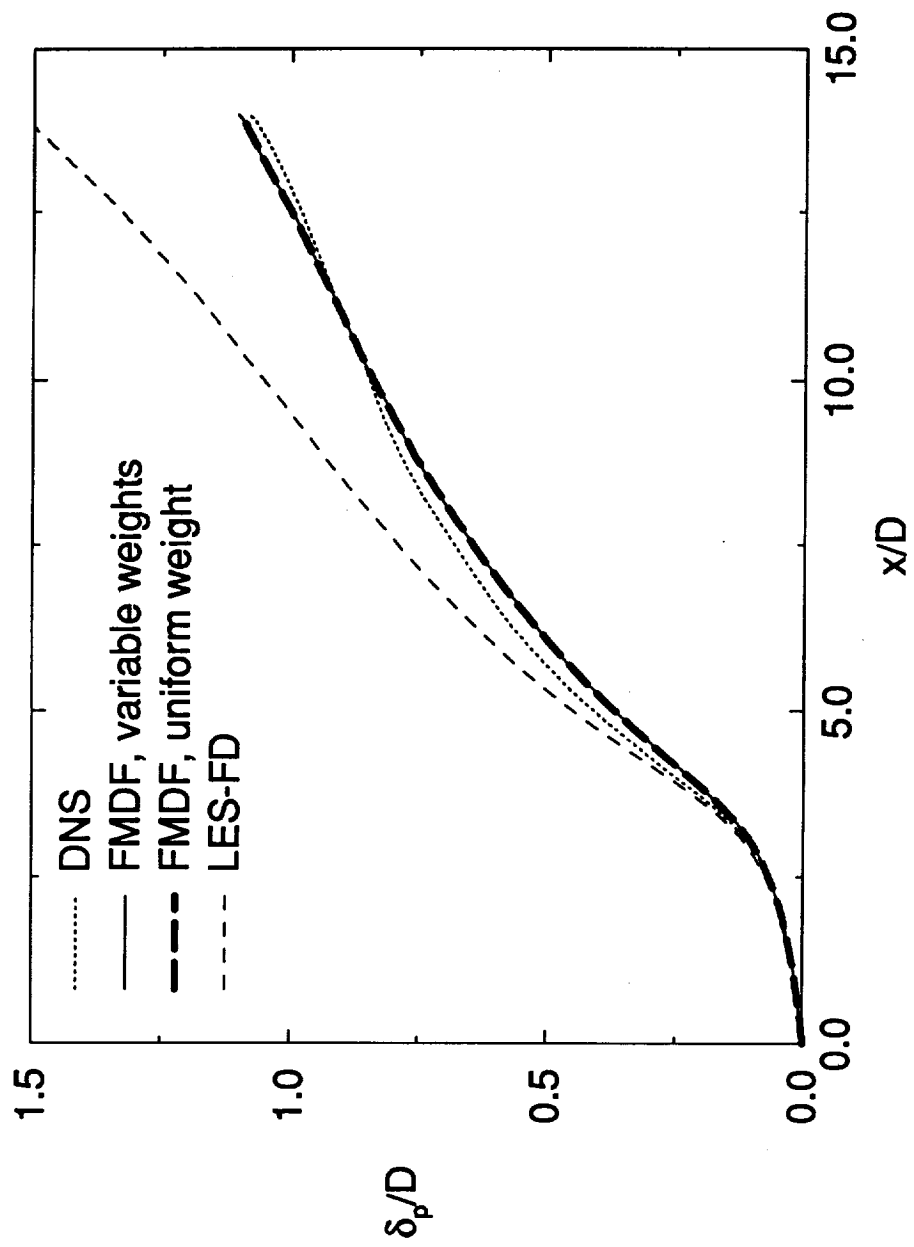


Figure 20(a)

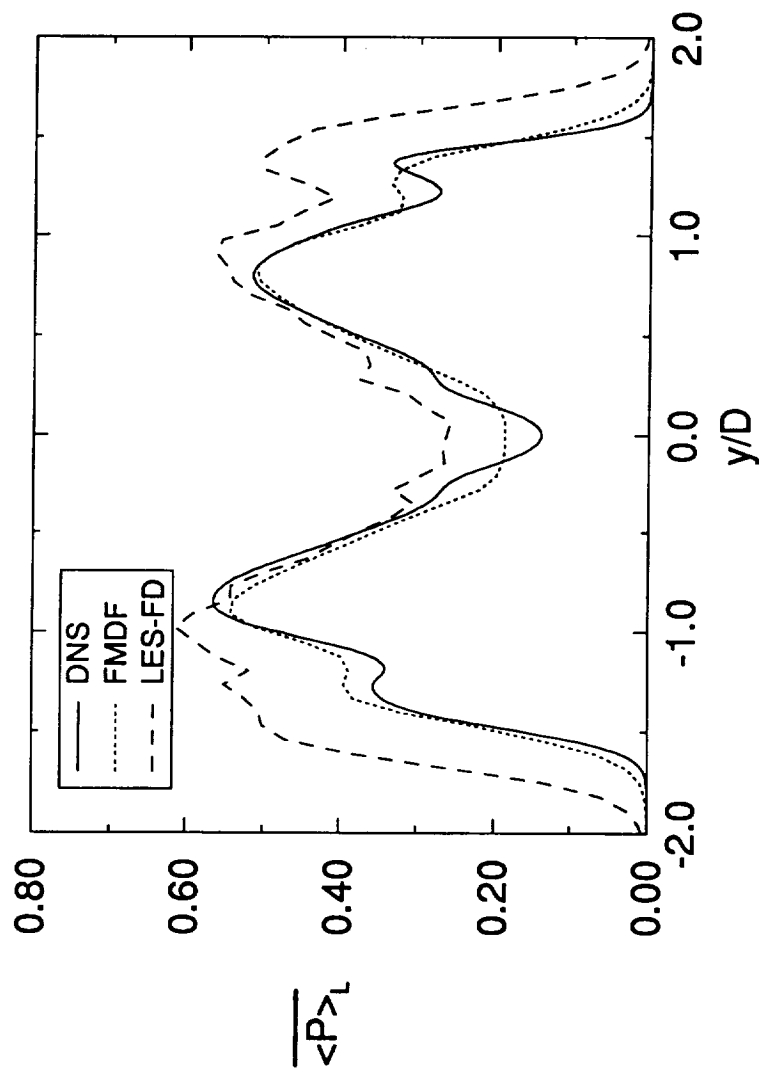


Figure 20(b)

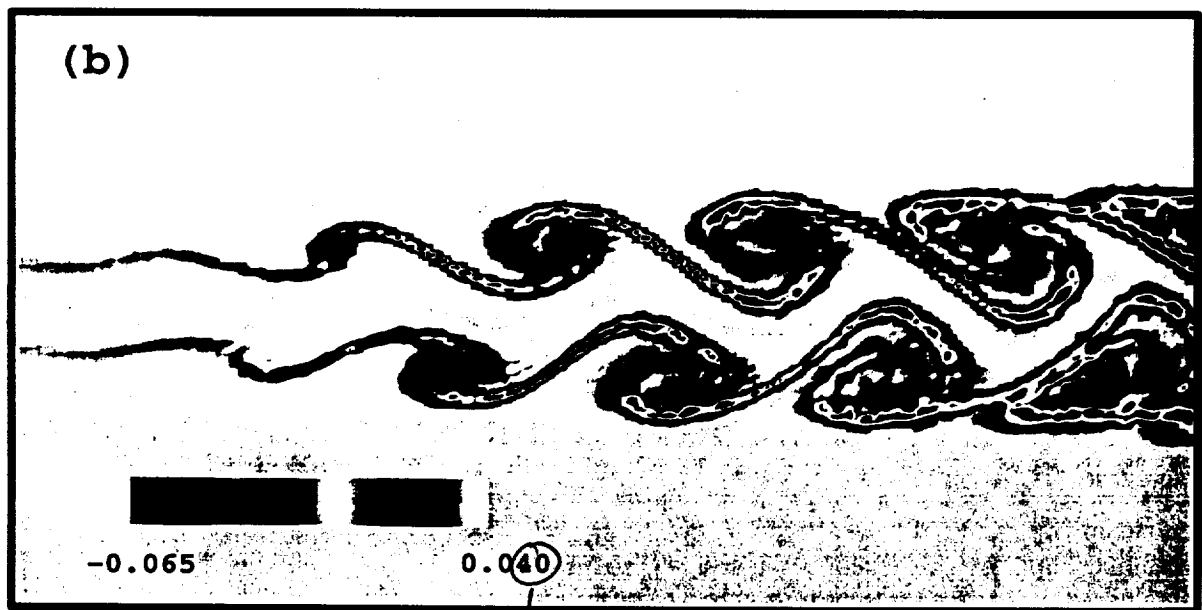


Figure 21

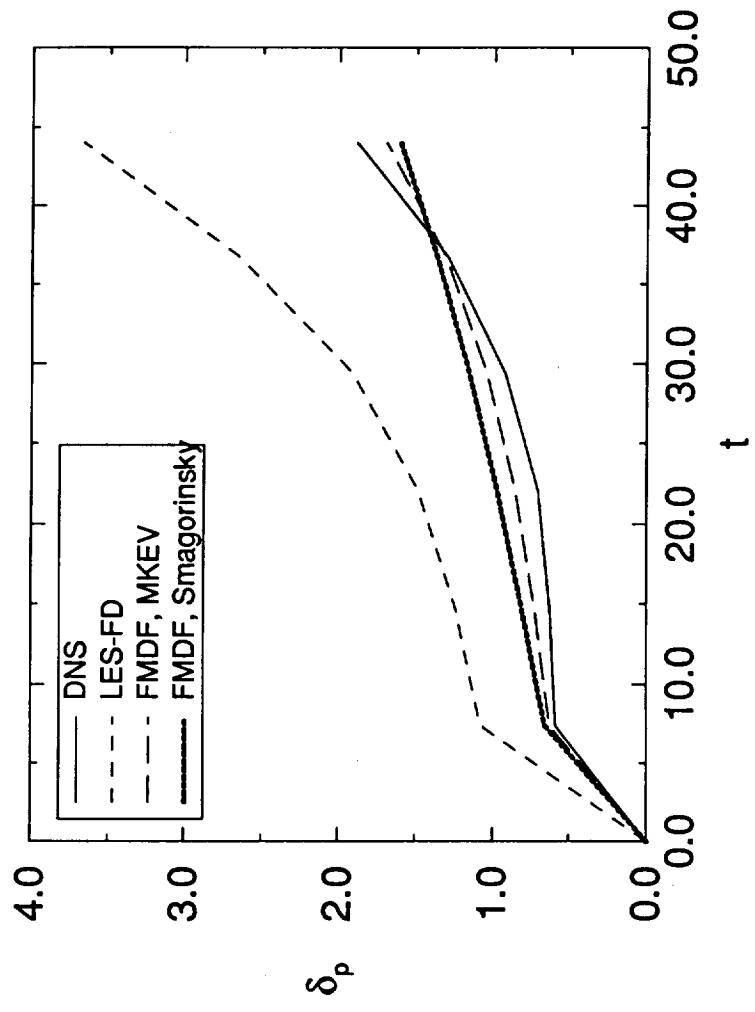


Figure 22(a)

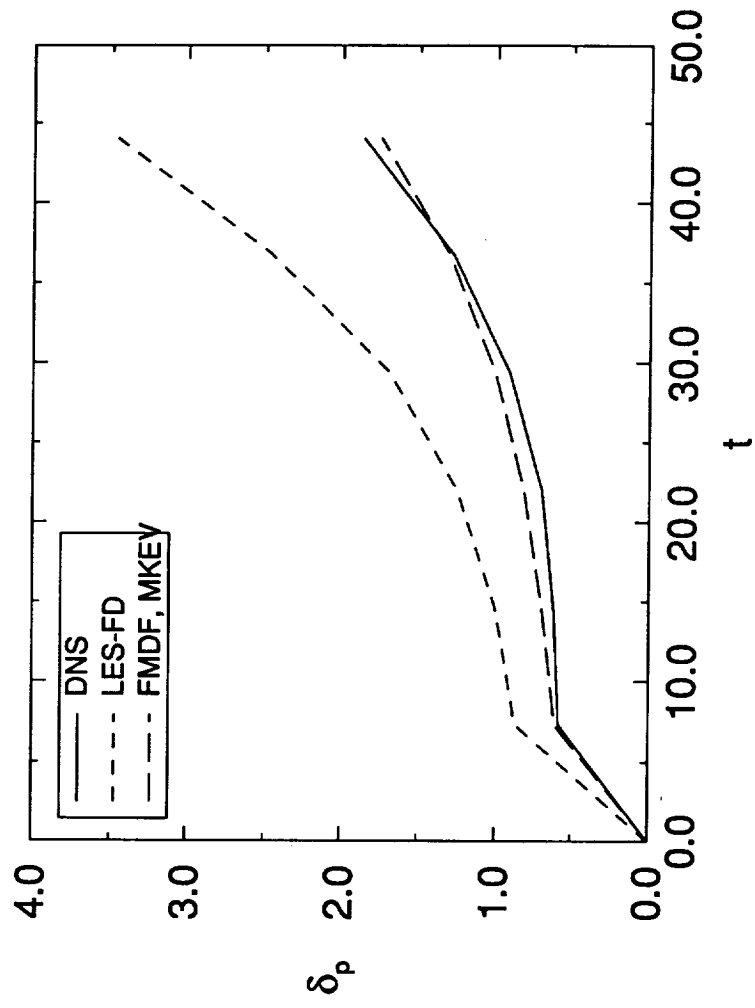


Figure 22(b)

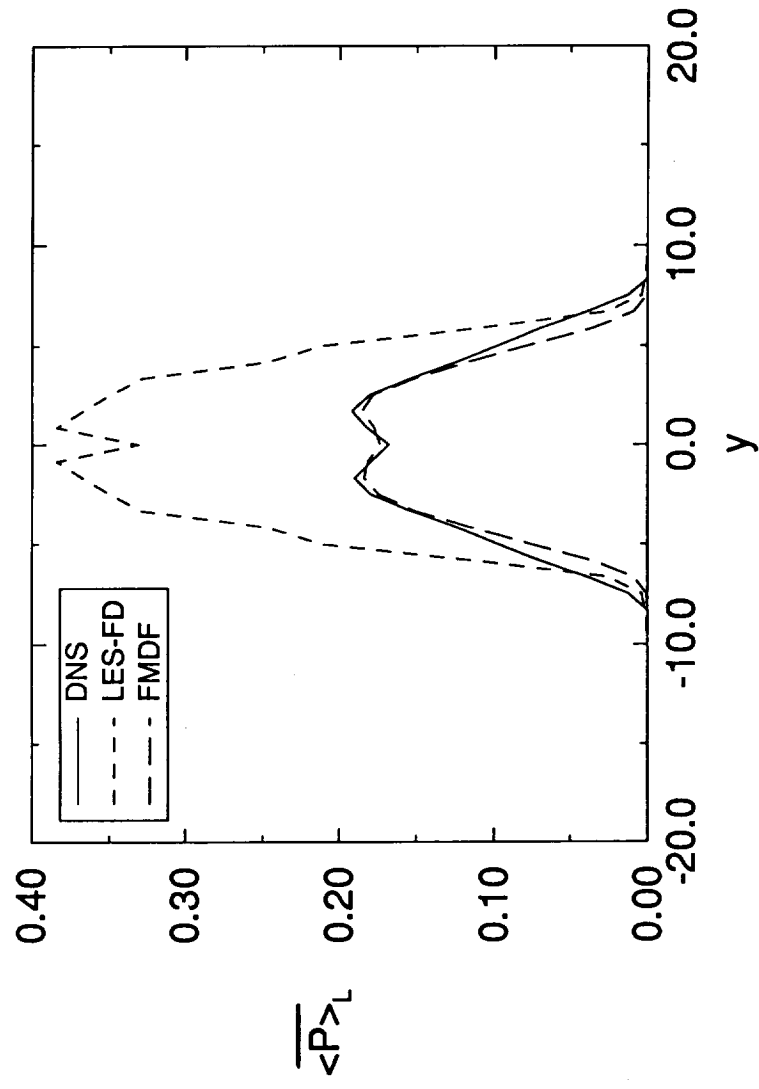


Figure 23(a)

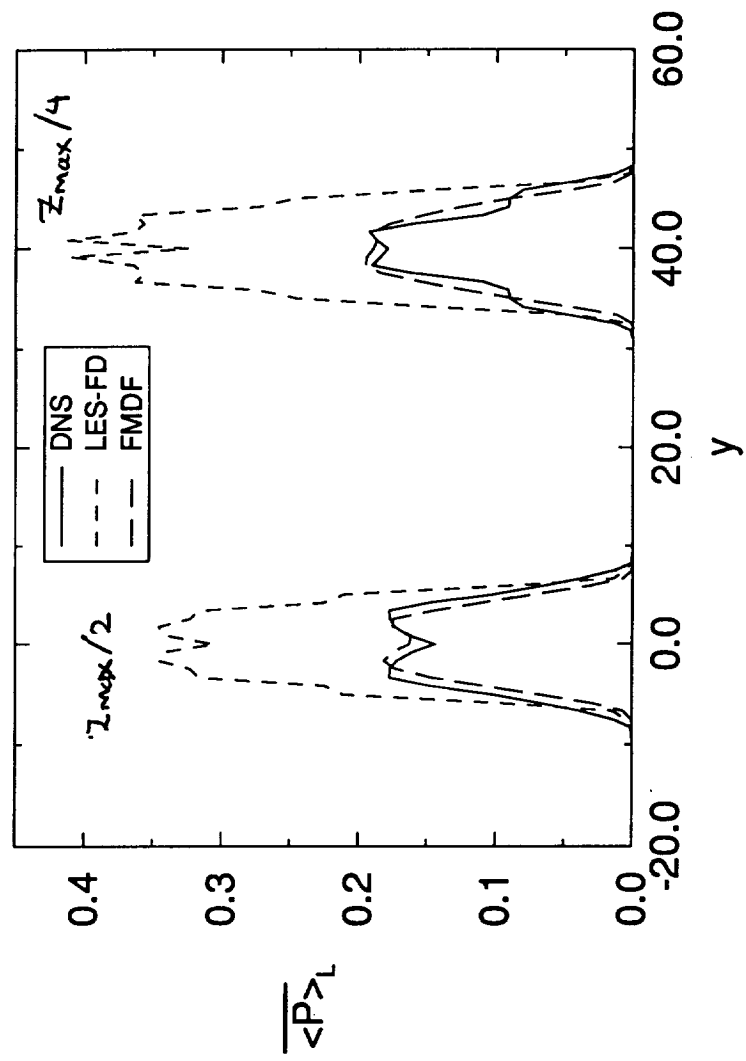


Figure 23(b)

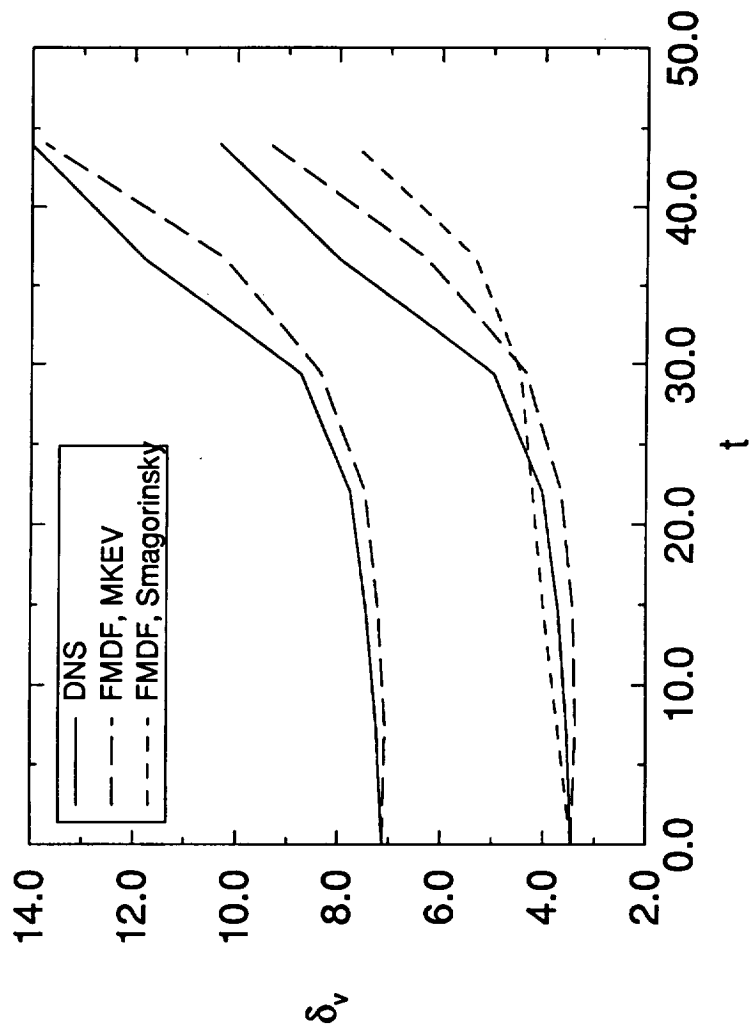


Figure 24

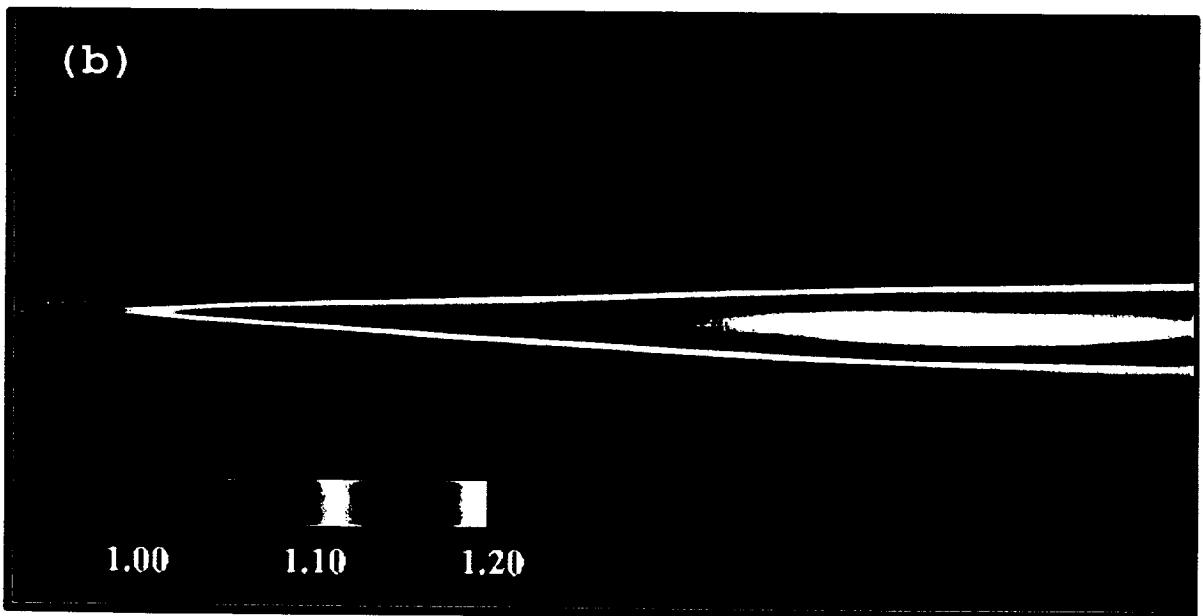
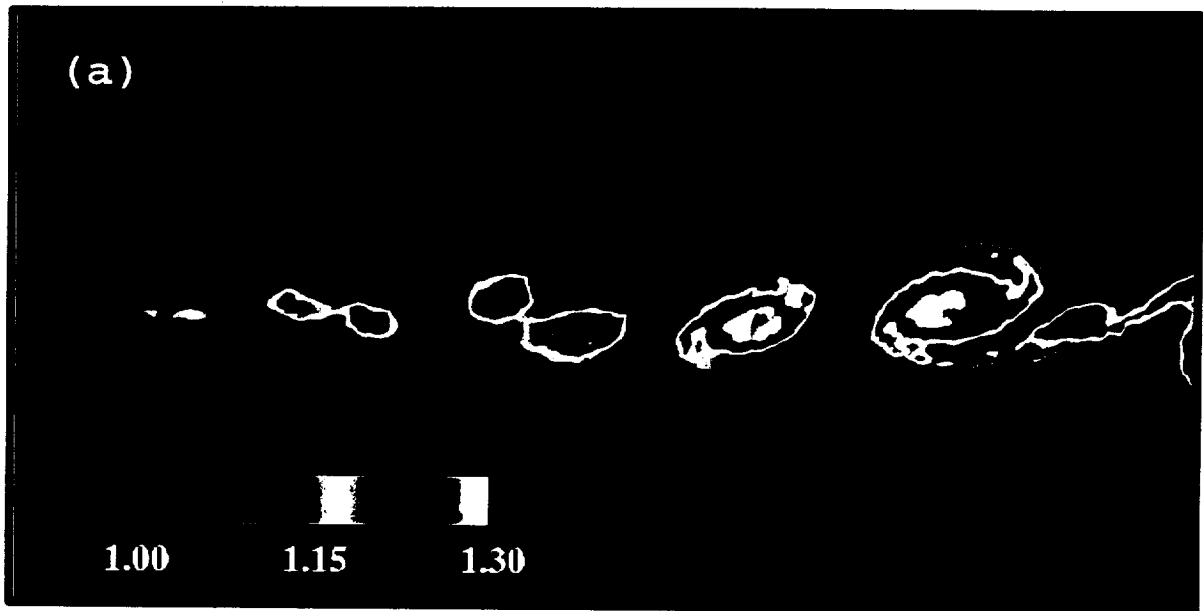


Figure 25

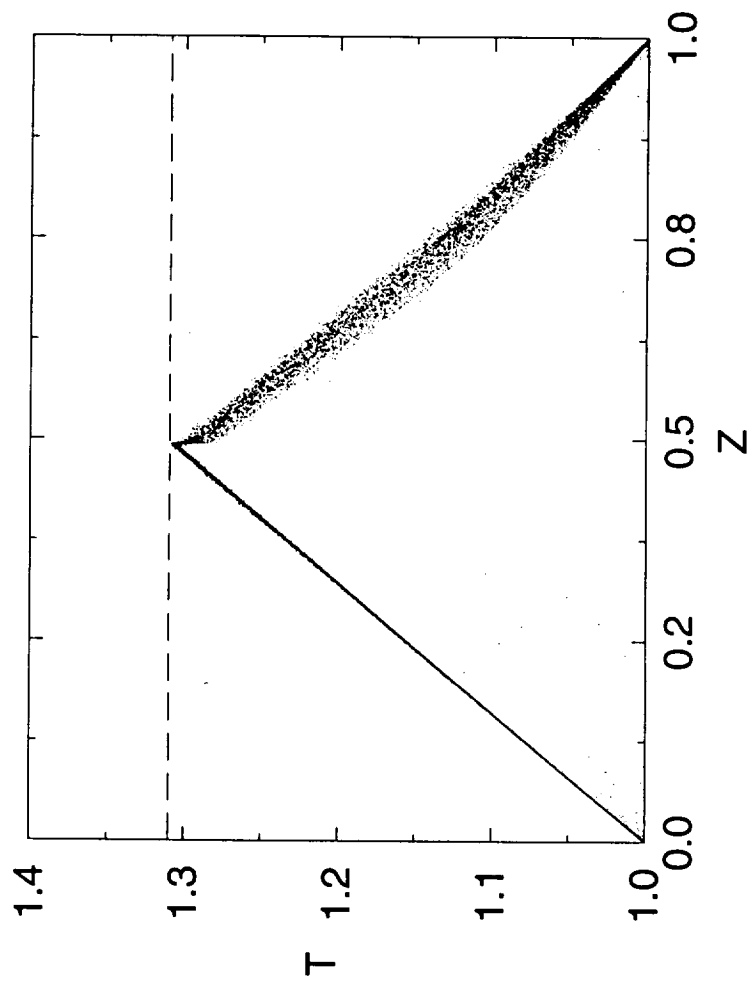


Figure 26

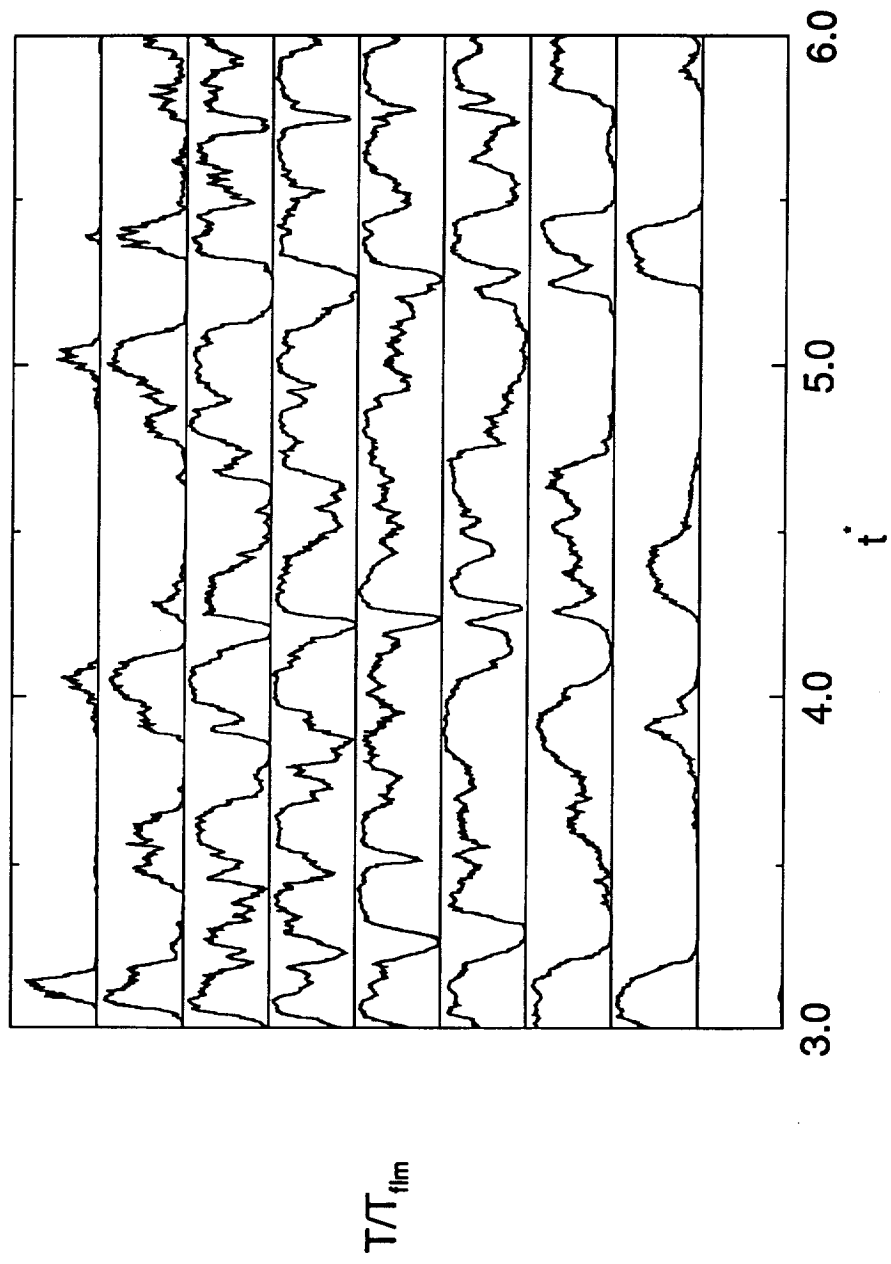


Figure 27

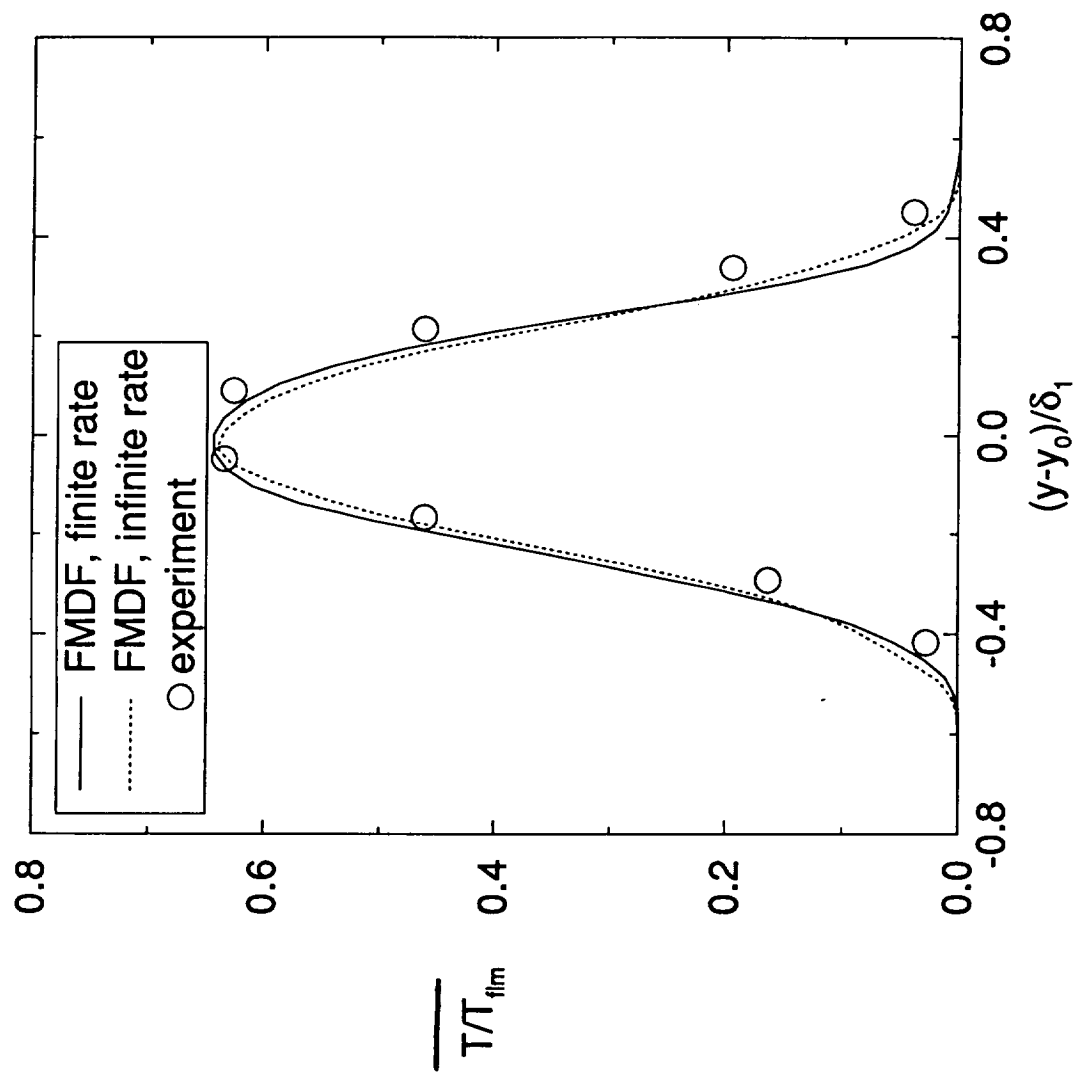


Figure 28

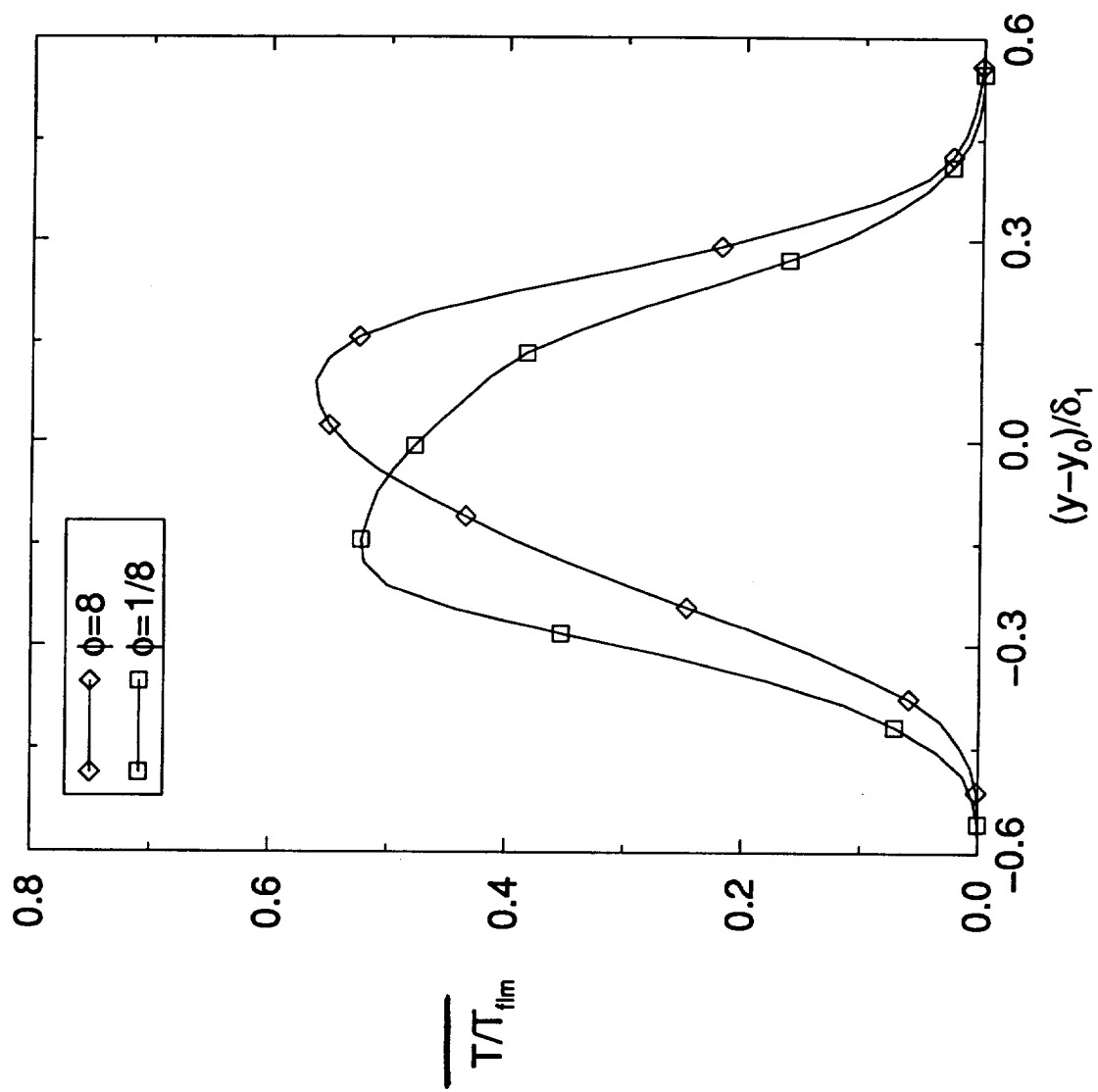


Figure 29

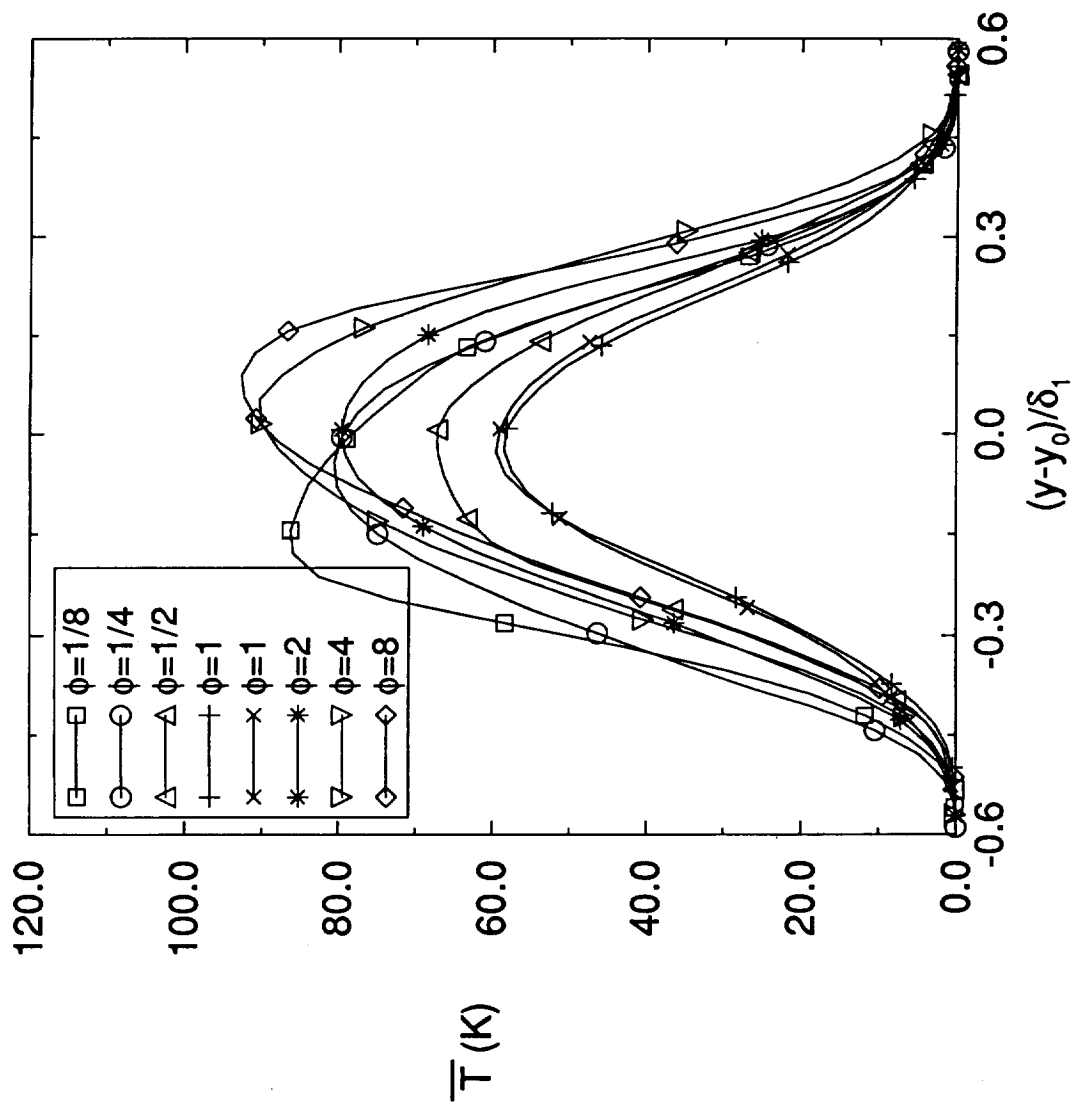


Figure 30(a)

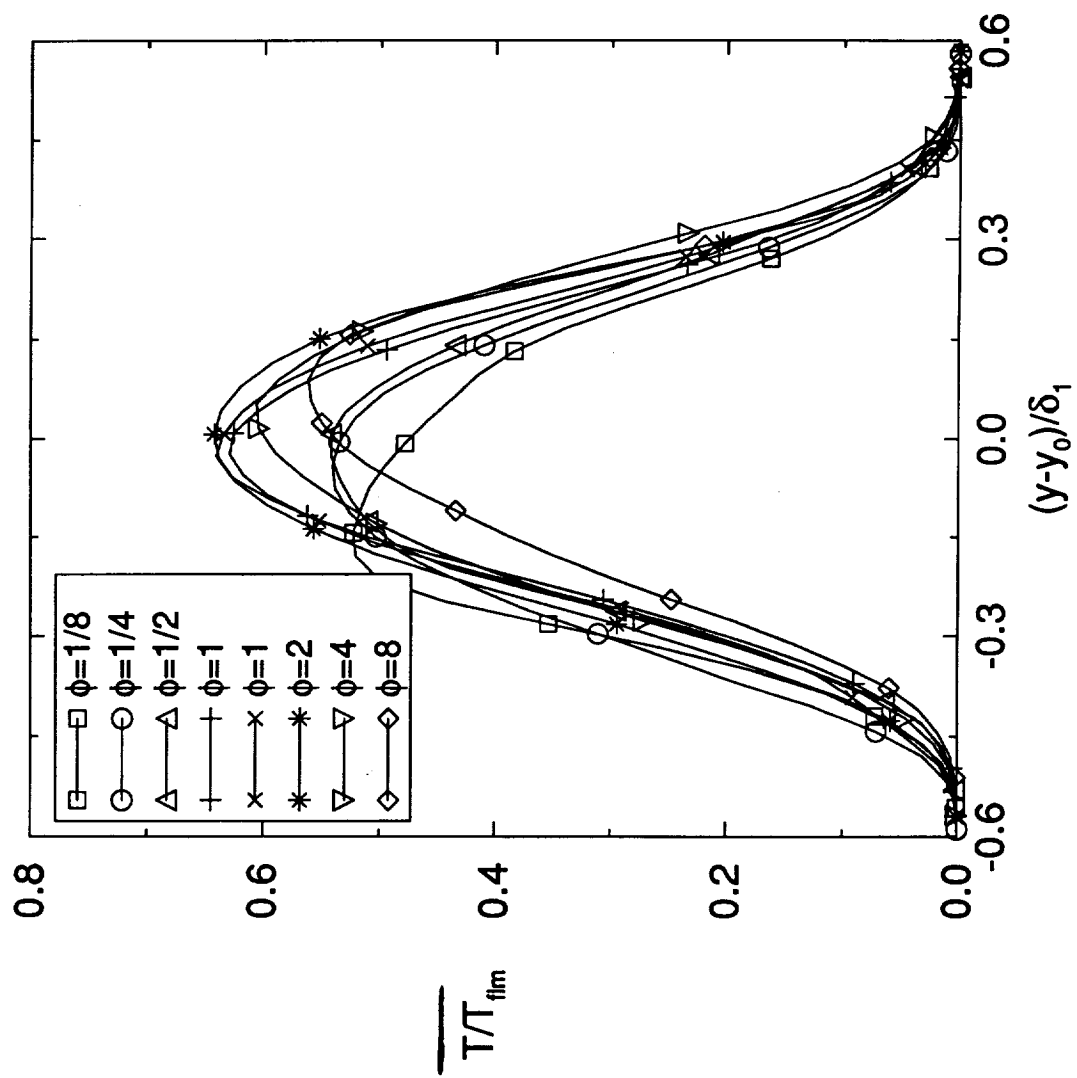


Figure 30(b)

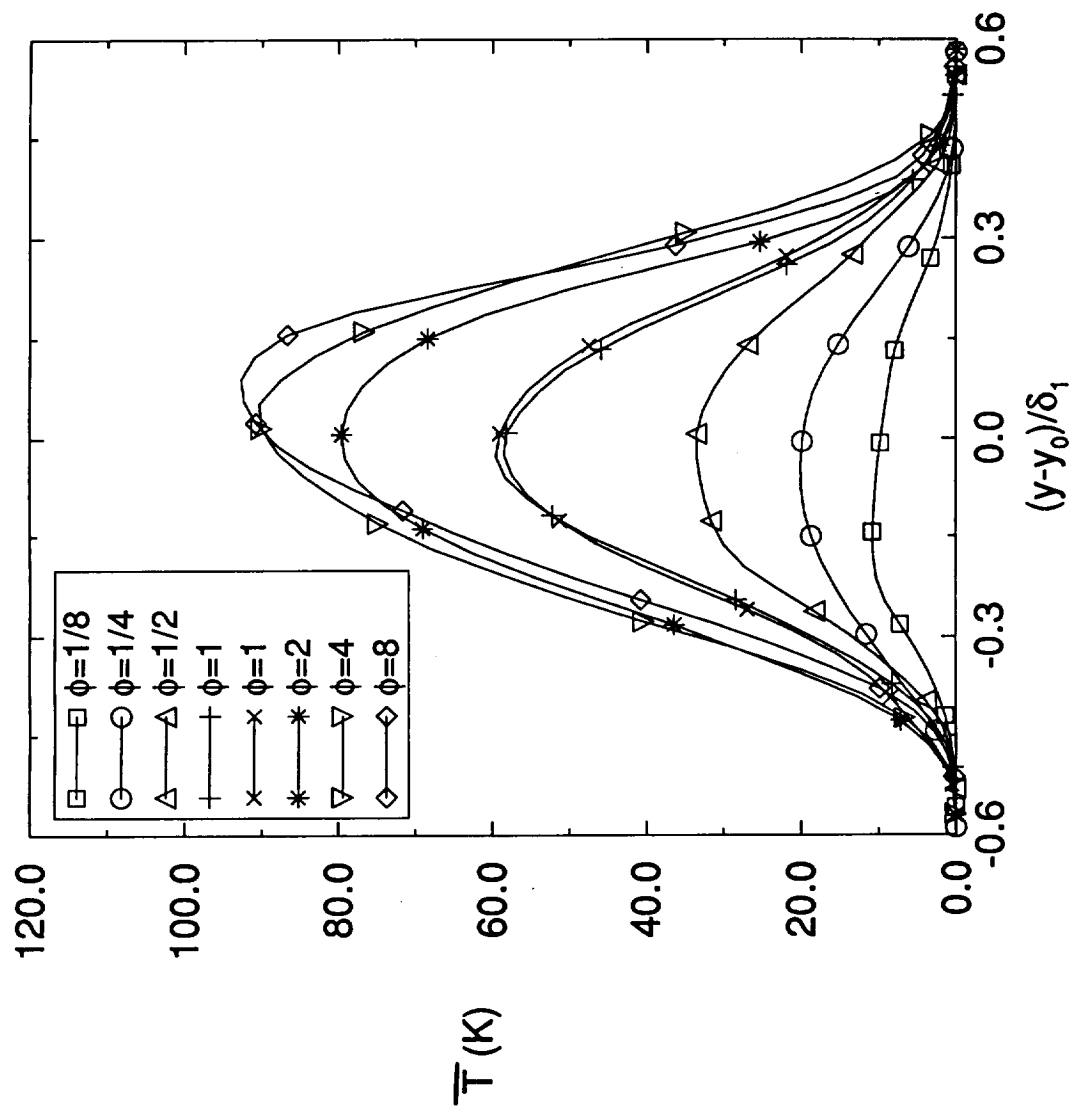


Figure 31(a)

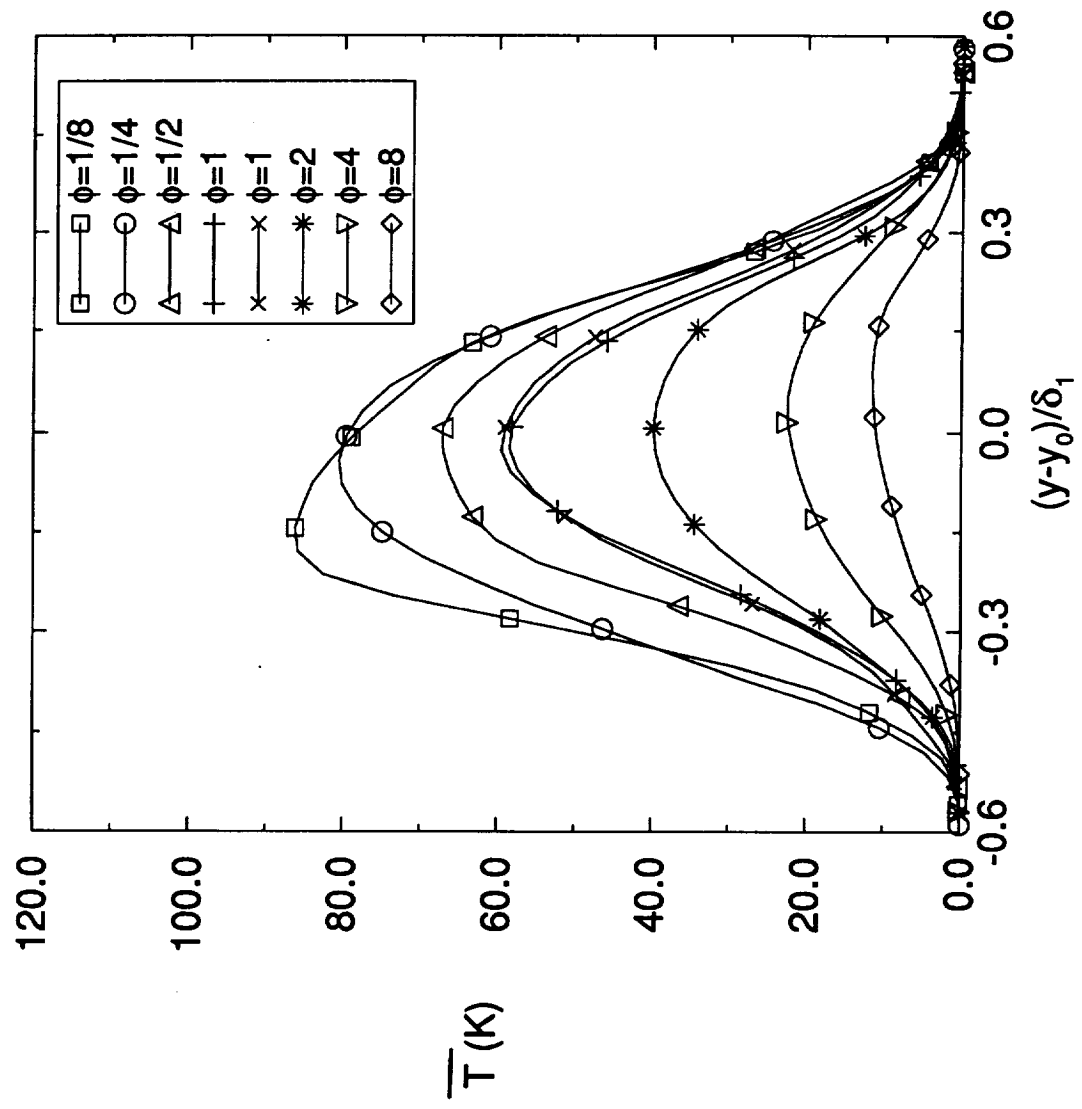


Figure 31(b)

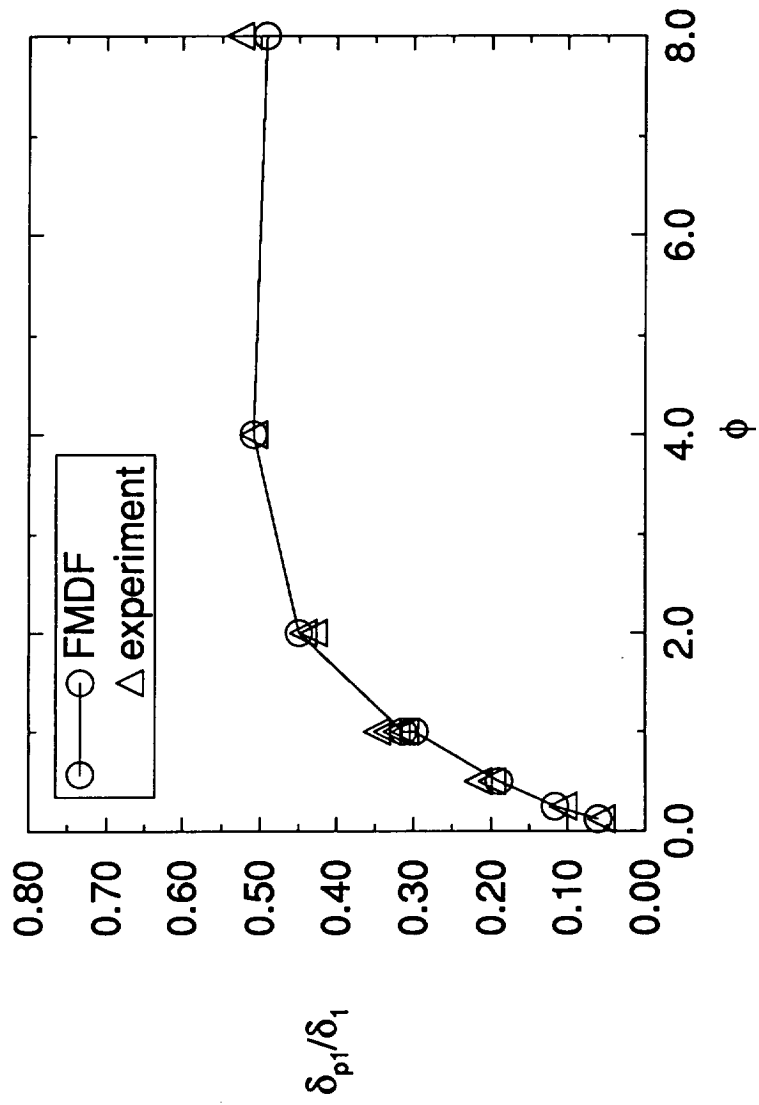


Figure 32(a)

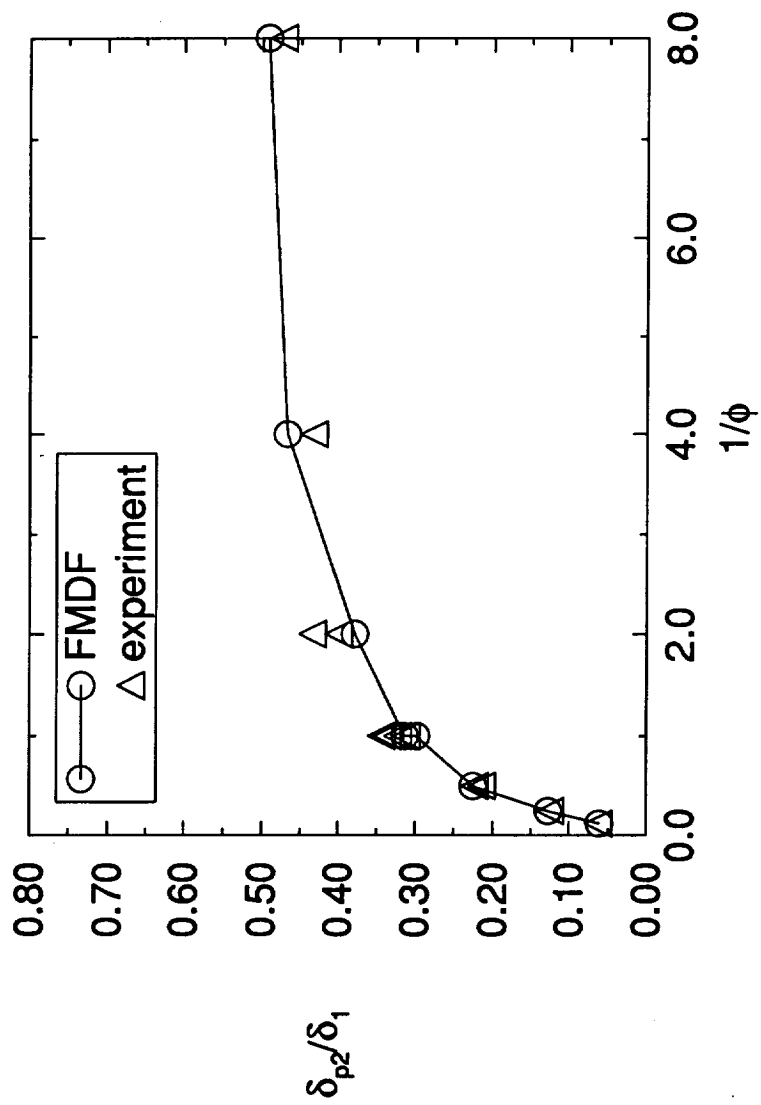


Figure 32(b)